UNIVERSITY OF CALIFORNIA, IRVINE

Materials design through phase and microstructure engineering: case studies in metal additive manufacturing and high entropy silicide thin films

DISSERTATION

submitted in partial satisfaction of the requirements
for the degree of

DOCTOR OF PHILOSOPHY

in Materials Science and Engineering

by

Aleksandra L. Vyatskikh

Dissertation Committee:
Professor Julie M. Schoenung, Chair
Distinguished Professor Diran Apelian
Professor Lorenzo Valdevit

2021

DEDICATION

This dissertation is dedicated to my grandmother

Irina Galperina

and my mother

Maria Studenikina Apparuti

who have always supported me unconditionally in any endeavor,
and to the memory of my grandfather,

Nikolay Studenikin,

who fostered and inspired my intellectual curiosity.

TABLE OF CONTENTS

LIST OF FIGURES

LIST OF TABLES

ACKNOWLEDGEMENTS

First and foremost, I would like to thank my Ph.D. advisor **Professor Julie M. Schoenung**. As professor and as chair of UCI's MSE department, Dr. Schoenung has created a unique environment that encourages inquiry and creativity and promotes teamwork and mentorship. She has been a truly amazing mentor throughout my time in the JMS group, and I have been incredibly lucky to have her as my Ph.D. advisor.

I would also like to express my sincere gratitude to the members of my thesis committee, **Professor Diran Apelian** and **Professor Lorenzo Valdevit**, as well as members of my qualifying exam committee, **Professor James Earthman** and **Professor Mohammad Javad Abdolhosseini Qomi**, for insightful suggestions and support.

Professor **Enrique J. Lavernia** has always been a true role model for me. I would like to thank him for challenging me intellectually and for many thoughtful scientific discussions that really helped me grow as a scientist and engineer.

I am sincerely grateful to **Professor Horst Hahn**, who has been an incredible mentor and collaborator. **Dr. Leonardo Velasco** has been an amazing colleague and mentor to me during my visit to Karlsruhe Institute of Technology; I am extremely thankful for a chance to work with such a talented and passionate scientist.

This work would not be possible without the help and support of the former and current members of the JMS group: **Dr. James Haley**, **Dr. Umberto Scipioni Bertoli**, **Dr. Benjamin MacDonald**, **Dr. Xin Wang**, **Dr. Baolong Zheng**, **Dr. Yizhang Zhou**, **Dr. Parnian Kiani**, **Thomas B. Slagle**, **Katherine Acord**, **Sen Jiang**, **Calvin Belcher**, **Salma Anter El-Azab**, **Arturo Meza**, and **Justin Cortez**. You are the best colleagues and friends one could ever wish for.

A lot of the experimental work that appears in this dissertation has been performed at the **Irvine Materials Research Institute (IMRI)**. IMRI staff members have been a tremendous help in designing and carrying out the experiments, and I would like to thank **Dr. Jian-Guo Zheng**, **Dr. Qiyin Lin**, **Dr. Mingjie Xu** and **Dr. Ich Tran** for their assistance and expertise. I am also incredibly thankful to **Darryl Mack**, **Amy Ricks** and **Desiree Rios**, whose unwavering support of MSE graduate students made my progress in the Ph.D. program possible.

I thank **Dr. Anastasia Goldt** and **Professor Albert Nasibulin** at Skolkovo Institute of Science and Technology for their help with thin film sheet resistance measurements.

Last but not least, I would like to acknowledge my family. My mother, **Maria**, and grandmother, **Irina**, always had my back throughout over two decades of school. My husband, **Andrey**, has encouraged and inspired me to pursue a Ph.D. and helped me stay motivated throughout this journey. Thank you all for being there for me.

The text of this dissertation is a partial reprint of the material as it appears in the following publications:

- A. L. Vyatskikh, T. Slagle, S. Jiang, S. A. El-Azab, U. Scipioni Bertoli, L. Valdevit, E. J. Lavernia, J. M. Schoenung, Thickness-dependent microstructure in additively manufactured stainless steel, Journal of Materials Engineering and Performance, 2021.
- A. L. Vyatskikh, B. E. MacDonald, A. D. Dupuy, E. J. Lavernia, J. M. Schoenung, H. Hahn, High entropy silicides: CALPHAD-based prediction and thin film fabrication, Scripta Materialia 201, 113914.
- D. Svetlizky, M. Das, B. Zheng, A. L. Vyatskikh, S. Bose, A. Bandyopadhyay, J. M. Schoenung, E. J. Lavernia, N. Eliaz, Direct metal deposition: technological aspects, material challenges and future prospects, Materials Today, 2021.

Permission to reprint copyrighted material has been granted by Springer Nature and Elsevier.

Part of this work was supported by the U.S. Army Research Office under Grant W911NF-18-1-0279. This research was also partially sponsored by the Jet Propulsion Laboratory, California Institute of Technology, under a contract with the National Aeronautics and Space Administration and carried out at UC Irvine under Contract Number 1558329. Partial financial support for the research described in this dissertation was provided by the German Academic Exchange Service (DAAD) under funding program 57507442.

In addition, I am sincerely grateful to the UC Irvine Graduate Division for the financial support provided by the Graduate Dean Recruitment Fellowship, Public Impact Fellowship and Chancellor's Club for Excellence Fellowship.

VITA

Aleksandra L. Vyatskikh

EDUCATION

University of California, Irvine — Irvine, CA
Ph.D. candidate, Materials Science and Engineering — 2017-2021
J. M. Schoenung Research Group

Skolkovo Institute of Science and Technology — Moscow, Russia
M. Sc., Materials Science — 2013-2015
Laboratory of Nanomaterials

Massachusetts Institute of Technology — Cambridge, MA
Master of Engineering in Manufacturing Program (Non-Degree) — 2013-2014
Department of Mechanical Engineering

Bauman Moscow State Technical University — Moscow, Russia
B. Eng., Manufacturing Processes and Systems — 2009-2013

PROFESSIONAL EXPERIENCE

Energoprom Group R&D Center — Moscow, Russia
Lead R&D specialist — June 2015 - May 2016
Employed Finite Element Analysis (FEA) to investigate failure modes of graphite anodes and cathodes under current-induced thermal stress.

TION Group — Novosibirsk, Russia
Intern at the R&D department — Summer 2014
Developed and scaled up a manufacturing process for fabrication of novel high-efficiency passive air filters consisting of nanometer-sized teflon fibers and micrometer-sized polypropylene fibers.

CONFERENCE PRESENTATIONS

3. **A. L. Vyatskikh,** B. Zheng, U. Scipioni Bertoli, L. Valdevit, E. J. Lavernia, J. M. Schoenung, Immiscible Alloys for Residual Stress Control in Metal Additive Manufacturing, TMS 2021 Annual Meeting and Exhibition (accepted talk, withdrawn due to the COVID-19 pandemic).
2. **A. L. Vyatskikh**, B. Zheng, U. Scipioni Bertoli, E. J. Lavernia, J. M. Schoenung. Residual Stress Mitigation in Metal Additive Manufacturing Using Compositional Engineering. Poster session presented at the TMS 2020 Annual Meeting & Exhibition, San Diego, CA, February 2020.
1. **A. L. Vyatskikh**, A. Tsapenko, E. Gilshteyn, T. Koltsova, T. Larionova, A. Talyzin, A. Anisimov, I. Anoshkin, E. I. Kauppinen, O. Tolochko, A.Nasibulin. Transparent and Conductive Hybrid Graphene/Carbon Nanotube Films. Poster session presented at the MRS Fall 2016 Meeting and Exhibit, Boston, MA, November 2016.

PUBLICATIONS AND PATENTS

10. **A. L. Vyatskikh**, X. Wang, E. J. Lavernia, J. M. Schoenung, Immiscible alloys for residual stress control in metal additive manufacturing (in preparation).
9. **A. L. Vyatskikh**, T. Slagle, S. Jiang, S. A. El-Azab, U. Scipioni Bertoli, L. Valdevit, E. J. Lavernia, J. M. Schoenung, Thickness-dependent microstructure in additively manufactured stainless steel, Journal of Materials Engineering and Performance, 2021.
8. J. M. Schoenung, **A. L. Vyatskikh**, A. D. Dupuy, B. E. MacDonald, E. J. Lavernia, H. Hahn, Single phase high entropy intermetallics and method for manufacturing, U.S. Provisional Patent No. 63/110,666.
7. **A. L. Vyatskikh**, B. E. MacDonald, A. D. Dupuy, E. J. Lavernia, J. M. Schoenung, H. Hahn, High entropy silicides: CALPHAD-based prediction and thin film fabrication, Scripta Materialia 201, 113914.
6. E. M. Leung, C. S. Moore, M. A. Badshah, M. Pinedo, G. T. Stiubianu, **A. L. Vyatskikh**, S. R. Jim, Z. Feng, A. A. Gorodetsky, Infrared and mechanical properties of squid-inspired thermoregulatory composite materials, Advanced Materials Technologies (invited, in review).
5. D. Svetlizky, M. Das, B. Zheng, **A. L. Vyatskikh**, S. Bose, A. Bandyopadhyay, J. M. Schoenung, E. J. Lavernia, N. Eliaz, Direct metal deposition: technological aspects, material challenges and future prospects, Materials Today, 2021.
4. E.M. Leung, M. Colorado Escobar, G.T. Stiubianu, S.R. Jim, **A.L. Vyatskikh**, Z. Feng, N. Garner, P. Patel, K.L. Naughton, M. Follador, E. Karshalev, M.D. Trexler, A.A. Gorodetsky, A dynamic thermoregulatory material inspired by squid skin, Nature Communications 10 (2019) 1947.
1) **A. L. Vyatskikh**, A. G. Nasibulin, "Single walled carbon nanotubes in photonics and optoelectronics" in *Photonics in Russia and the world: a public analytical report* (Bitubi, Moscow, Russia, 2016).
2. **A. L. Gorkina**, A. P. Tsapenko, E. P. Gilshteyn, T. S. Koltsova, T. V. Larionova, A. Talyzin, A. S. Anisimov, I. V. Anoshkin, E. I. Kauppinen, O. V. Tolochko, A. G. Nasibulin, Transparent and conductive hybrid graphene/carbon nanotube films, *Carbon*, 100, 501-507 (2016). (Featured in the "Carbons for wearable devices" special issue)
1. **A. L. Gorkina**, E. P. Gilshteyn, A. G. Nasibulin, A. P. Tsapenko, Y. G. Gladush, Infrared radiation detector based on single-walled carbon nanotubes and graphene, Russian Federation Patent No. 162 342 U1, 16.12.2015.

AWARDS AND HONORS

Public Impact Fellowship — November 2020
University of California, Irvine

Chancellor's Club for Excellence Fellowship — November 2020
University of California, Irvine

Short-Term Research Grant — September 2020
German Academic Exchange Service (DAAD)

The 21st National School on Neutron and X-Ray Scattering — June 2019
Argonne and Oak Ridge National Laboratories

Graduate Dean's Recruitment Fellowship — March 2017
University of California, Irvine

ABSTRACT OF THE DISSERTATION

Materials design through phase and microstructure engineering: case studies in metal additive manufacturing and high entropy silicide thin films

by

Aleksandra L. Vyatskikh

Doctor of Philosophy in Materials Science and Engineering

University of California, Irvine, 2021

Professor Julie M. Schoenung, Chair

The 21st century presents humanity with unique challenges, addressing which requires constant improvements in manufacturing technologies and engineering materials. In this dissertation, two areas of modern material research are explored: additive manufacturing and high entropy materials.

First, the problem of microstructural inhomogeneities within additively manufactured metal parts is addressed. Specifically, the effect of process parameters and feature thickness on the microstructures of 316L stainless steel components fabricated by laser powder bed fusion (LPBF) is examined. A standard benchmark geometry developed by the National Institute of Standards and Technology, which contained walls of 0.5, 2.5 and 5.0 mm in thickness, is used. Optical microscopy, finite element analysis, scanning electron microscopy and electron backscatter diffraction reveal dramatic microstructural differences in features of different thickness within the same component. The feature thickness influences the cooling rate, which in turn impacts the melt pool size, solidification microstructure, grain morphology and density of geometrically necessary dislocations. The relationship between feature size and grain morphology is dependent on the energy input used during LPBF. Such behavior suggested that local manipulation of LPBF process parameters can be

employed to achieve microstructural homogeneity within as-printed stainless steel components.

Second, a novel approach toward manipulation of residual stresses in additively manufactured parts is explored. Alloy design involving engineering of solid-state transformations is proposed as a way to change the residual stress state of the as-printed components. To this end, parts fabricated from two metals (pure Fe and Fe-50Cu) are evaluated. Residual stress measurements demonstrate that surface residual stresses can be successfully manipulated by adjusting the alloy composition. It is hypothesized that solid-state transformations experience by the Fe and Fe-rich phases are responsible for the observed differences in residual stresses. This study is the first to suggest using residual stress as a design criterion in alloy engineering for metal additive manufacturing.

Finally, a new high entropy silicide material for applications in electronics is proposed. The CALculation of PHAse Diagrams (CALPHAD) approach is used to identify two candidate single-phase high entropy silicides (HES): the ternary (CrMoTa)Si2 and the quinary (CrMoTaVNb)Si2. Both candidate compositions are experimentally synthesized via electron beam evaporation followed by heat treatment in vacuum, which facilitates the solid-state reaction. Both the ternary (CrMoTa)Si2 and the quinary (CrMoTaVNb)Si2 HES form a single phase with a C40 hexagonal crystal structure, validating our CALPHAD phase formation predictions. This work reports the first experimental realization of a thin film high entropy silicide material.

INTRODUCTION

The 21st century presents the humanity with extraordinary challenges. Raising global population, urbanization and global travel are causing the likelihoods of global pandemics, not unlike the coronavirus disease (COVID-19) pandemic we were battling at the time this dissertation was submitted, to rise [1,2]. At the same time, climate change makes catastrophic weather events, such as heat waves, storms, and flooding, more frequent and less predictable [3,4].

Scientists and engineers are striving to mitigate the risks of these unprecedented worldwide threats. Development of novel materials, in particular, provides critical and continuous improvements in all areas of human development. For example, the ever-increasing computing power demands are being met with the help of low-dimensional materials, such as carbon nanotubes [5] and graphene [6]. Innovative sustainable energy generation and storage solutions, such as low cost batteries [7,8], high efficiency solar cells [9] and hydrogen storage systems [10,11], are designed to meet the growing energy demands. The need for improved structural materials is satisfied by magnesium alloys [12], high specific strength architected materials [13,14] and high entropy alloys [15].

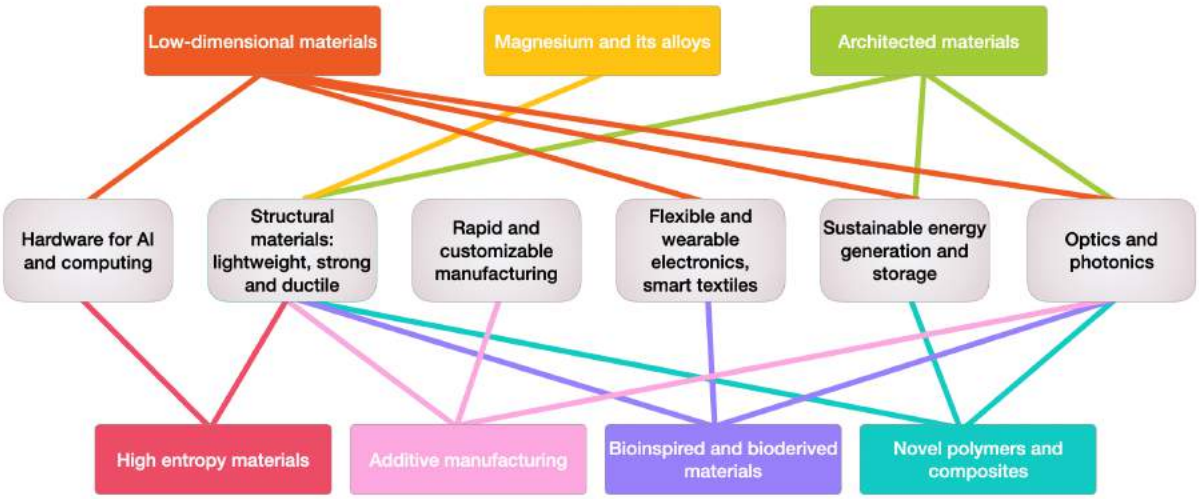

Some examples of current technological challenges (middle row) and materials-based solutions to them.

The research presented in this dissertation is aiming to address two of the important technological challenges. First, key issues in metal additive manufacturing, or 3D printing, are discussed. Metal AM is a crucial technology that allows to locate manufacturing close the points of consumption, reducing lead times and enabling rapid crisis response. Second, a new set of materials for applications in electronic devices is proposed. In this work, the high entropy materials design approach is extended to silicide materials. A novel single-phase high entropy silicide with good electrical conductivity is designed, fabricated using thin film processing, and characterized.

Chapter 1 discusses a study of microstructural variations within additively manufactured metal parts. The influence of local part geometry on the microstructure of 316L stainless steel parts fabricated via laser powder bed fusion is investigated. Features of 0.5, 2.5 and 5.0 mm in thickness were studied via electron backscattered diffraction (EBSD), which revealed grain size and aspect ratio distributions. Local plastic deformation was assessed by the density of geometrically necessary

dislocations (GNDs). Additionally, scanning electron microscopy (SEM), conductive atomic force microscopy (AFM) and X-ray diffraction (XRD) unveiled the influence of feature thickness on the amount of retained δ-ferrite. The results suggest that local microstructural differences in additively manufactured parts can be mitigated by adjusting process parameters.

Chapter 2 presents a novel approach to residual stress management in metal additive manufacturing (AM). In contrast to traditional residual stress mitigation approaches that involve manipulation of AM process parameters, this chapter discusses tailoring the alloy composition to adjust residual stresses. In particular, a mechanism for leveraging solid-state phase transformations to control residual stresses in metal AM is proposed. Directed energy deposition (DED) is employed to fabricate parts from pure Fe and Fe-50Cu (wt.%) binary alloy. It is demonstrated that at 50 wt.% Cu in a Fe-Cu binary alloy, the $\delta \rightarrow \gamma$ transformation in Fe is eliminated, which leads to formation of high compressive residual stresses in the Fe-50Cu parts. Through transmission electron microscopy (TEM) and EBSD we observed a large dislocation density within the Cu-rich phase, suggesting that residual stressed formed during processing are accommodated through plastic deformation of the Cu-rich phase. This work demonstrates that residual stress can be used as a design parameter in alloy engineering for additive manufacturing.

In chapter 3, a novel material for use in electronic devices is described. The composition of the high entropy silicide material was determined using the CALculation of PHAse Diagrams (CALPHAD) approach. The (CrMoTaVNb)Si_2 was then fabricated in thin film form using electron beam evaporation or magnetron sputtering, followed by heat treatment in vacuum. Grazing incidence XRD measurements confirmed the CALPHAD predictions that (CrMoTaVNb)Si_2 forms a

single phase with a C40 hexagonal crystal structure. Electrical characterization of the films revealed that their resistivity falls within the boundaries established by the constituent binary metal disilicides. The research presented in this chapter is the first report of a thin film high entropy silicide material.

CHAPTER 1 THICKNESS-DEPENDENT MICROSTRUCTURE IN ADDITIVELY MANUFACTURED STAINLESS STEEL

1.1 Introduction

Metal additive manufacturing (AM), also referred to as metal 3D printing, is poised to revolutionize the manufacturing industry by enabling shorter lead times, light-weighting through topology optimization, part count reduction, and rapid production of parts with complex geometries [16]. A remarkable recent example of successful AM implementation is the GE Aviation Catalyst turboprop engine **(Figure 1.1, a)**, where AM enabled consolidation of 800 components into just 12 printed parts, reducing the engine's weight by 5% and improving its specific fuel consumption by 1% [17]. Another notable example is NASA's 2020 Perseverance Mars rover, which features 11 3D printed parts [18]. Use of AM in Perseverance's planetary instrument for X-ray lithochemistry (PIXL) allowed for a three- to four-fold mass reduction in comparison with traditionally manufactured components **(Figure 1.1, b)**. SpaceX's SuperDraco rocket engine powering the Crew Dragon manned spacecraft employs an additively manufactured Inconel thrust chamber [19] **(Figure 1.1, c)**. According to the company, use of metal AM in place of conventional manufacturing resulted in an order of magnitude reduction in lead time, with the path from the initial concept to the first hotfire test taking just over three months [20].

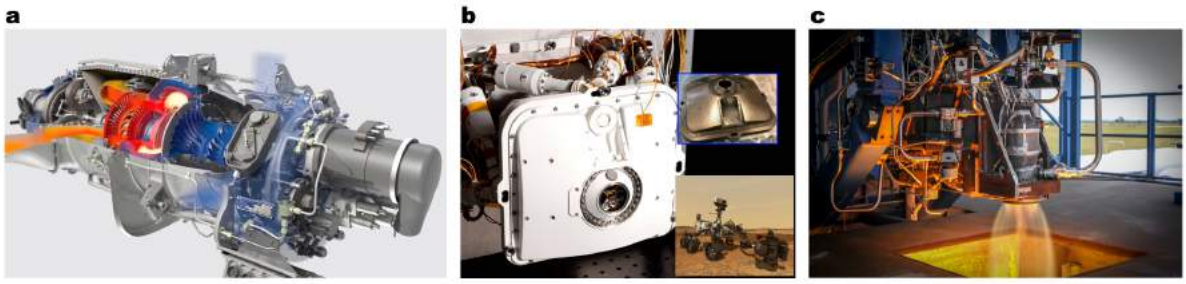

Figure 1.1. Examples of successful implementation of metal additive manufacturing. a) GE Aviation Catalyst Turboprop engine. b) Planetary instrument for X-ray lithochemistry (PIXL) installed on NASA Perseverance Mars rover. c) SpaceX SuperDraco engine.

These examples demonstrate that metal AM can be successfully implemented in critical aerospace components subjected to extreme environments. However, continued progress towards widespread industrial adoption of metal AM requires a comprehensive understanding of the local variations in phase composition, microstructure and mechanical properties caused by location-dependent thermal history of the parts. Such an understanding is especially important for geometrically complex components that contain features of different sizes, e.g. parts with integrated fluid/gas channels [21,22]. The relationship between feature size, microstructure and mechanical performance has been explored recently in 316L [23] and 304L [24] stainless steel parts fabricated by laser powder bed fusion (LPBF), Ti-6Al-4V parts produced by electron beam melting (EBM) [24–26], as well as LPBF-fabricated AlSi10Mg [27] and Inconel 625 [28]. Roach et al. investigated microstructure and mechanical properties of 316L stainless steel parts of varying cross-sectional areas fabricated via LBPF [23]. No clear relationship between the sample cross-sectional area and grain size, grain aspect ratio, sample crystallographic texture and microhardness was established. However, samples with larger cross-sectional areas tended to exhibit higher yield strength (YS), ultimate tensile strength (UTS) and elastic modulus, which was attributed to surface roughness effects. Brown et al. observed a

similar trend in LPBF-fabricated 316L stainless steel and EBM-fabricated Ti-6Al-4V, where an increase in sample thickness induced an increase in YS and UTS in both materials – an effect that was also attributed to surface roughness and defects [24]. However, a clear relationship between feature thickness, microstructure, phase composition and mechanical properties has not been established to date.

In this work, we made a step towards establishing a relationship between thickness and microstructural properties in stainless steel parts fabricated via laser powder bed fusion (LPBF). We used a standard, widely employed metal AM benchmark geometry developed the National Institute of Standards and Technology (NIST) [28–30]. We fabricated the benchmark components from 316L stainless steel, a very low-carbon austenitic stainless steel which is a popular metal AM material [31–34] due to its ductility, high corrosion resistance and low propensity for chromium-rich carbide formation [35–37]. Through a combination of 3D scanning, optical microscopy, finite element analysis (FEA), scanning electron microscopy and electron backscatter diffraction, we demonstrated dramatic microstructural variations within features of different thickness within the same component. Our findings suggest that microstructural homogeneity within the as-printed stainless steel components that possess features of varying thickness can be achieved through local manipulation of LPBF process parameters.

1.2 Materials and methods

1.2.1 Sample fabrication

For this study, we used the AMB2018-01 bridge structure geometry developed by NIST **(Figure 1.2, a)**. The benchmark part is 75 mm long, 12 mm tall and 5 mm wide, with 12 "legs" of three different thicknesses: four 5.0-mm legs, four 2.5-mm legs,

and four 0.5-mm legs. The samples were fabricated using a commercial SLM 125HL LPBF system (SLM Solutions, Lübeck, Germany). The chamber was kept in an inert nitrogen atmosphere, with oxygen level maintained at <100 ppm. Two samples were printed concurrently on the same annealed 316L stainless steel build plate. The build plate was preheated to and maintained at 200 °C. Gas atomized 316L stainless steel powder (SLM Solutions, Lübeck, Germany) with d_{10} = ~25 µm, d_{50} = ~40 µm and d_{90} = ~61 µm was used as feedstock powder. Manufacturer-specified chemical composition of the powder is provided in **Table 1.1**. Laser spot size was set to 80 µm. Samples were denoted as B120 and B200, with the number reflecting the approximate volumetric energy density (VED, J/mm^3) used during fabrication. VED, E_v, is defined as [38]:

$$E_v = \frac{P}{v \cdot t \cdot h}, \qquad (2.1)$$

where P is the laser power (W), v is the laser scan speed (mm/s), t is the layer thickness (mm) and h is the hatch spacing (mm). The LPBF process parameters shown in **Table 1.2** were selected on the basis of fabricating as-printed parts with >99% density.

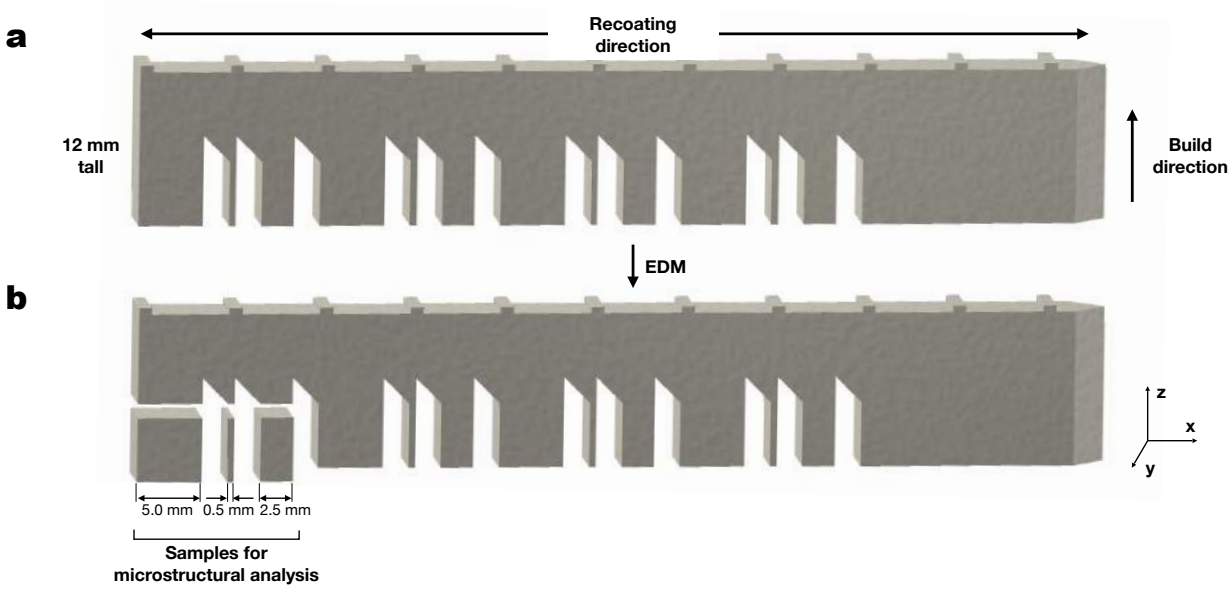

Figure 1.2. The AMB2018-01 sample geometry used in the study. a) 3D model of the AMB2018-01 bridge structure benchmark geometry. b) Three legs (lower left corner) were separated from the parts for microstructural analysis using wire electrical discharge machining.

Table 1.1. Chemical composition (mass fraction in %) of the feedstock powder, as provided by the manufacturer.

Fe	Cr	Ni	Mo	Nb+Ta	Mn
Balance	16.00-18.00	10.00-14.00	2.00-3.00	-	2.00

Si	P	S	C	N	O
1.00	0.045	0.030	0.030	0.10	-

Table 1.2. Laser powder bed fusion process parameters used for sample fabrication. The calculated value for volumetric energy density is also provided.

Sample ID	Laser power (W)	Scan speed (mm/s)	Hatch spacing (mm)	Layer thickness (mm)	Volumetric energy density (J/mm³)
B120	195	800	0.10	0.02	122
B200	370	2520	0.04	0.02	196

1.2.2 Characterization

The bridge structures were separated from the substrate using wire electrical discharge machining (wire-EDM). After separation from the substrate, the samples were imaged using an ATOS Core 200 3D scanner (GOM, Braunschweig, Germany). The 3D scans were processed with CloudCompare open source point cloud processing software, where the 3D scans were overlayed with the nominal CAD geometry, and cloud-to-mesh (C2M) distances were computed.

Legs of 0.5, 2.5 and 5.0 mm in thickness were then separated from the bridge structure using wire-EDM **(Figure 1.2, b)**. For examination under an optical microscope (OM) and scanning electron microscope (SEM), the legs were hot-mounted in Konductomet conductive filled phenolic mounting compound (Buehler, Lake Bluff, IL, USA) with the y-z surface exposed. Metallographic grinding was performed with 120-1200 grit silicon carbide papers using an AutoMet 250 grinder/polisher (Buehler, Lake Bluff, IL, USA). The samples were then polished with 3 μm and 1 μm DiaLube diamond suspensions on White Label woven silk polishing cloth (Allied High Tech Products, Inc., Rancho Dominguez, CA, USA). A final precision polish was obtained from vibratory polishing (GIGA-0900, PACE Technologies, Tucson, AZ, USA) for ~5 hours using a 0.05 μm alumina suspension (PACE Technologies, Tucson, AZ, USA) mixed with deionized water. To reveal the solidification microstructures, the samples were etched using a 3:1 volume mixture of HCl and HNO_3 for 30 seconds. Immediately following the immersion in the acid solution, the samples were placed in a cold water bath to prevent overetching. Melt pool boundaries were identified from optical micrographs of the etched cross-sections, and the melt pool widths and depths were measured using ImageJ software (NIH) [39].

Electron backscatter diffraction (EBSD) mapping and forescattered electron (FSE) imaging were performed using a GAIA3 SEM-FIB dualbeam microscope (Tescan, Brno, Czech Republic) equipped with a NordlysMax2 detector (Oxford Instruments, Abingdon, Oxfordshire, UK). The microscope was operated in field mode at an accelerating voltage of 20 kV, beam intensity of 20 and working distance of ~5 mm. Samples were mounted on a 70° pre-tilted specimen holder. Two scans with 4x4 CCD camera binning were performed for each sample: i) 1x1 mm map with a step size of 2 μm, and ii) 390x765 μm map with a step size of 1 μm. To avoid near-surface zones where grain refinement is possible, EBSD maps were collected from the middle regions of the specimen cross-sections.

EBSD maps were post-processed using the open source MTEX Matlab toolbox [40]. First, data points with mean angular deviation (MAD) of > 1° were removed. Then, grains were defined as areas of the map completely surrounded by boundaries with a misorientation > 5°, and grain reconstruction was performed. The orientation data were denoised and missing data were interpolated using the half-quadratic filter [41]. Grain aspect ratio was calculated as the ratio of the long axis length to the short axis length of the ellipses fitted to the grains. Kernel average misorientation (KAM) was computed using the first order neighbors. Density of geometrically necessary dislocations (GNDs) was calculated following the approach suggested by Pantleon [42] based on local orientation changes.

SEM imaging for primary dendrite arm spacing (DAS) measurements was performed using the Magellan 400 XHR microscope (FEI, Hillsboro, OR, USA). DAS was calculated based on a series of SEM micrographs using the modified Abrams three-circle procedure as described in ASTM E112 [43]. After the DAS values were obtained, the corresponding cooling rates were calculated as [44]:

$$d_p = 80(CR)^{-0.33}, \qquad (2.2)$$

where d_p is the DAS (μm) and *CR* is the corresponding cooling rate (°K/s).

Powder X-ray diffraction (XRD) patterns were collected with the Smartlab diffractometer equipped with a 2.2 kW Cu-Ka X-ray source (Rigaku, Tokyo, Japan) configured in Bragg-Brentano geometry. The patterns were collected in the 2θ range of 20-120° with 0.02° step and at a scan speed of 4 °/s.

Conductive atomic force microscopy (C-AFM) images were acquired with the Tosca microscope (Anton Paar, Graz, Austria) equipped with an ARROW-EFM tip (NanoWorld, Neuchâtel, Switzerland) with a platinum-iridium coating.

1.3 Results

First, the bulk geometry of the as-printed bridge samples was evaluated. The total length and width as measured from the 3D scans were 76.08 x 5.25 mm and 76.20 x 5.55 mm for samples B120 and B200, respectively. The C2M distances are plotted in **Figure 1.3, a-b**, and the corresponding C2M histograms are shown in **Figure 1.3, c**. The median C2M distance was ~53 μm for sample B120 and ~167 μm for sample B200. While both samples were found to be larger than the original CAD geometry (75 mm long and 5 mm wide), the deviation from the input file was greater for sample B200, which was fabricated with a higher energy input. A 61% increase in VED correlated with a ~215% increase in the median C2M distance. It is therefore evident that the dimensional accuracy of the as-printed parts was significantly affected by the process parameters used during LPBF processing. Deviation of part geometry from the input CAD file should be taken into consideration in further benchmark investigations.

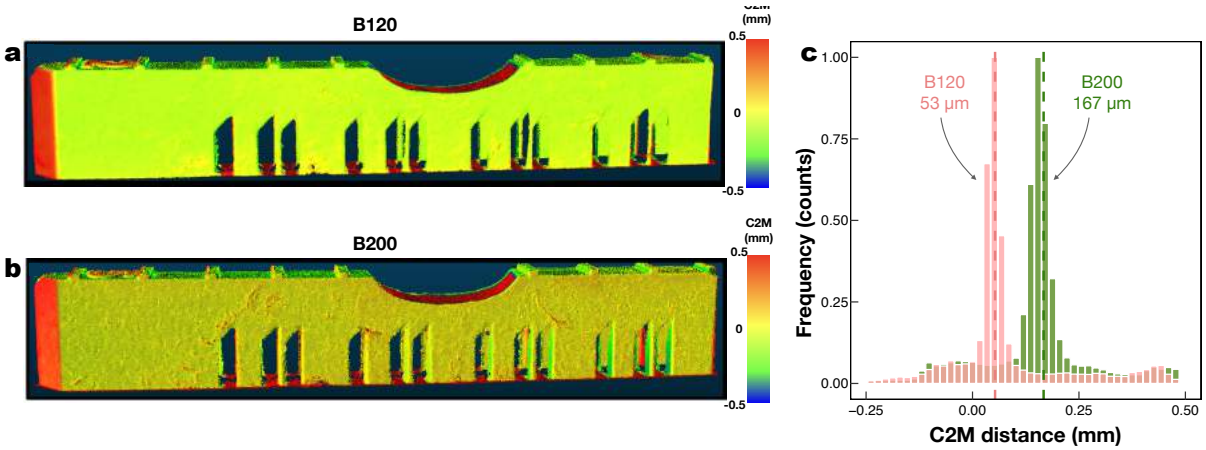

Figure 1.3. Dimensional accuracy of the as-printed AMB2018-01 bridge structures. Cloud-to-mesh (C2M) distances plotted over the 3D scans of the a) sample B120, and b) sample B200. c) Histogram plots of the C2M distances, with dashed vertical lines indicating median C2M distances.

Next, the melt pool geometries of the as-printed samples were analyzed. For sample B120, no clear trend could be identified in melt pool depth as a function of leg thickness, with measured mean pool depth of 29.2 ± 1.0, 27.9 ± 1.4 and 28.8 ± 1.14 µm for the 0.5, 2.5 and 5.0 mm thick legs, respectively **(Figure 1.4, a)**. For sample B200, however, the mean melt pool depth decreased with increasing leg thickness, from 22.8 ± 1.8 to 21.6 ± 1.7 and to 14.2 ± 1.2 µm for the 0.5, 2.5 and 5.0 mm thick legs, respectively. For both samples B120 and B200, the melt pool width decreased with increasing leg thickness **(Figure 1.4, b)**. For sample B120, the measured mean melt pool widths were 121.1 ± 3.4, 105.3 ± 3.4 and 105.6 ± 2.4 µm for the 0.5, 2.5 and 5.0 mm thick legs, respectively. For sample B200, the melt pool widths were 112.4 ± 7.8, 98.6 ± 7.4 and 94.1 ± 5.5 µm for the 0.5, 2.5 and 5.0 mm thick legs, respectively. Overall, melt pool was both shallower and narrower for sample B200. A representative optical micrograph demonstrating both melt pool fusion lines and grain boundaries is shown in **Figure 1.4, c**.

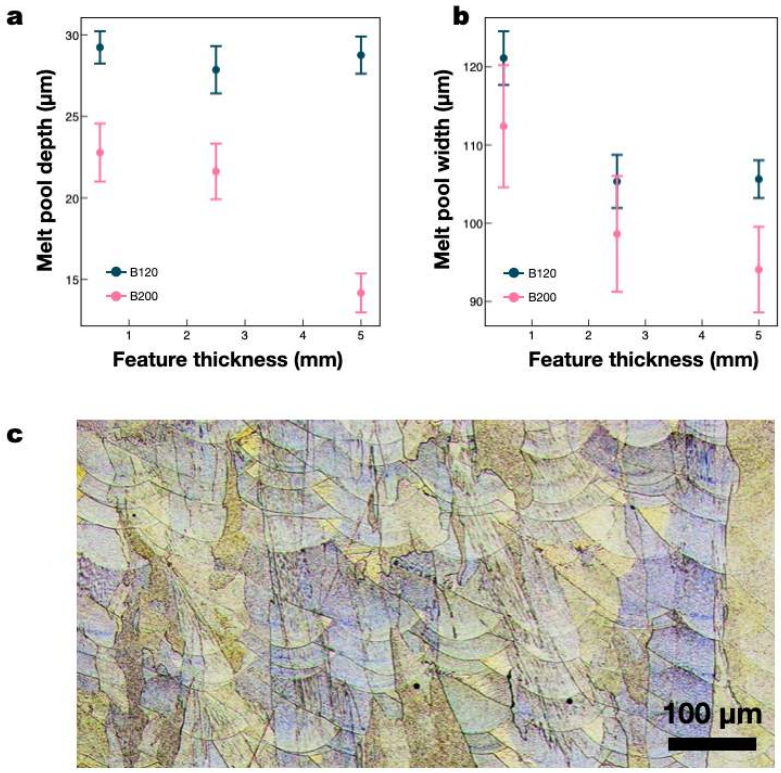

Figure 1.4. Melt pool geometry within the as-printed AMB2018-01 bridge structures. Melt pool a) depth, and b) width as a function of feature thickness. c) A representative optical micrograph of an etched B120 0.5 mm sample showing melt pool fusion lines and grain boundaries. Error bars represent 95% confidence intervals.

FEA modeling, as discussed in detail in [45], confirmed that melt pool dimensions should be smaller in sample B200 than in sample B120. Smaller depth and width of the melt pool in sample B200 can be attributed to a more elongated, teardrop-like shape of the melt pool along the scanning direction, as confirmed by the temperature profiles extracted from the FEA model [45].

Further microstructural characterization was performed via a quantitative analysis of the grain structure of the samples. For sample B120, inverse pole figure (IPF) maps overlayed over FSE images are shown in **Figure 1.5, a**. Within the 0.5 mm thick leg, the grains had irregular, faceted morphologies. For the 2.5-mm thick leg, grains formed long columns of ~62 µm in width, with smaller grains located between the adjacent large columnar grains. A similar grain structure was observed for the 5.0

mm leg, where the width of the columnar grains was ~80 μm. Mean grain areas for sample B120 were 718 ± 102, 764 ± 188 and 912 ± 208 μm² for the 0.5, 2.5 and 5.0 mm thick legs, respectively. For sample B200, IPF maps overlayed over FSE micrographs are shown in **Figure 1.5, b**. Within the 0.5 mm thick leg, the grains were highly elongated and aligned along a direction rotated ~30° with respect to the build direction. In the 2.5 and 5.0 mm thick legs, grains had irregular, faceted shapes, and were aligned along the build direction. Mean grain areas for sample B200 were 1936 ± 483, 922 ± 181 and 546 ± 65 μm² for the 0.5, 2.5 and 5.0 mm thick legs, respectively.

Opposite trends in grain area as a function of feature thickness were identified in samples B120 and B200 **(Figure 1.5, c)**: in B120, grain area increased with feature thickness (a ~27% increase in grain area in the 5.0 mm thick leg as compared to that in the 0.5 mm leg), while in B200, grain area decreased with feature thickness (a ~72% decrease in grain area in the 5.0 mm thick leg as compared to that in the 0.5 mm thick leg). Similar trends were observed in grain aspect ratios (ARs) as a function of feature thickness **(Figure 1.5, d)**: in sample B120, grains tended to be more elongated as feature thickness increased (with ARs of 3.3 and 4.9 for the 0.5 and 5.0 mm thick legs, respectively), while in B200, grains tended to be more equiaxed in thicker features (AR of 4.9 and 3.4 for the 0.5 and 5.0 mm thick legs, respectively).

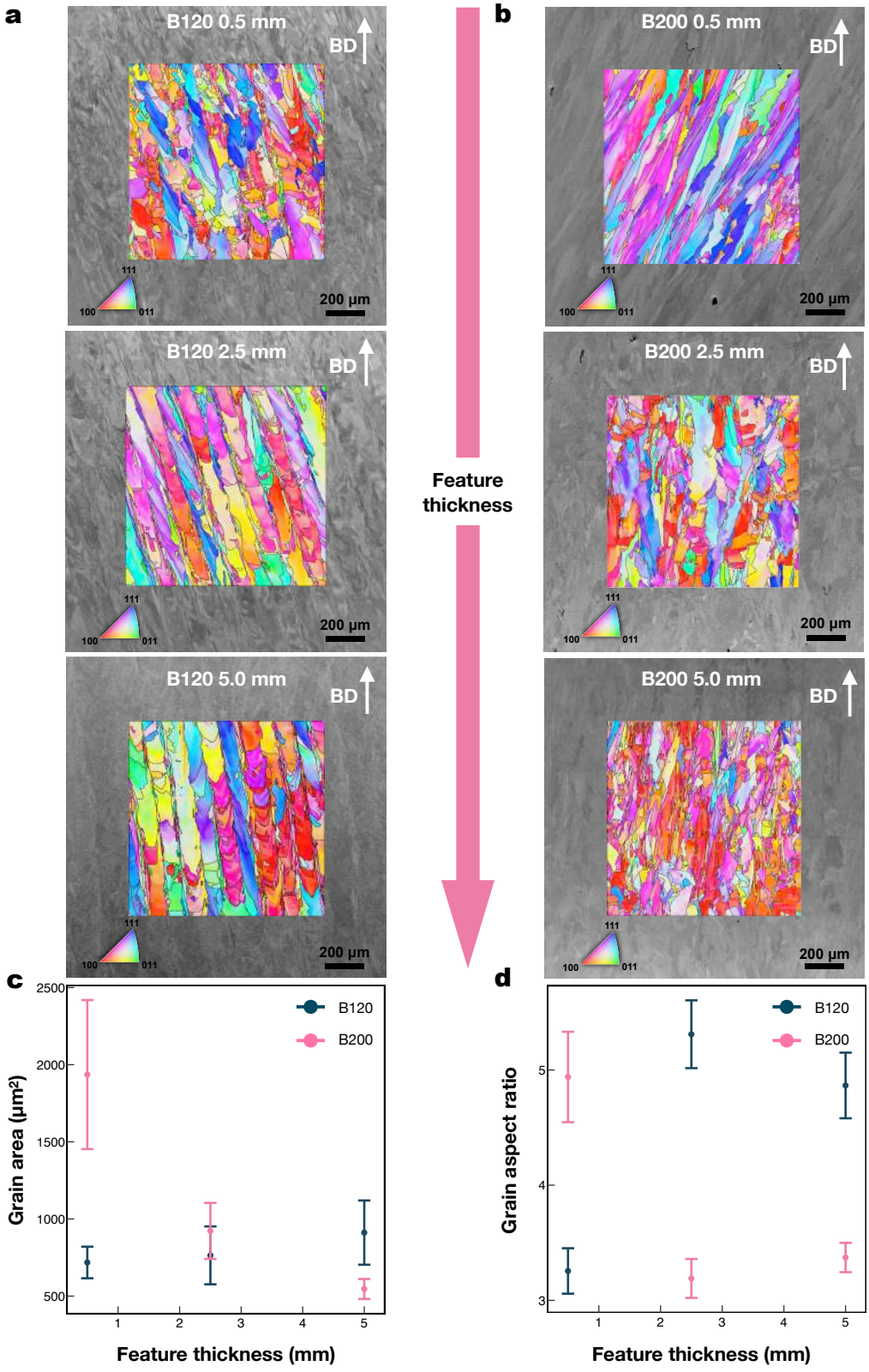

Figure 1.5. Analysis of the grain structure. Inverse pole figure maps overlayed over forescattered electron images for a) sample B120 and b) sample B200; c) grain area as a function of feature thickness; d) grain aspect ratio as a function of feature thickness; d) grain aspect ratio as a function of feature thickness. Error bars represent 95% confidence intervals.

To understand the factors that influence microstructure evolution, the solidification microstructures and the corresponding cooling rates were assessed. A representative secondary electron (SE) micrograph of the solidification microstructure is shown in **Figure 1.6, a**. Cooling rates calculated based on DAS are plotted as a function of feature thickness in **Figure 1.6, b**. No clear trend was identified in cooling rate as a function of feature thickness in sample B120, where cooling rates were calculated to be 11 x 10^5, 17 x 10^5 and 11 x 10^5 °K/s within the 0.5, 2.5 and 5.0 mm thick legs, respectively. For sample B200, the cooling rates were found to be 3 x 10^5, 6 x 10^5 and 6 x 10^5 °K/s within the 0.5, 2.5 and 5.0 mm thick legs, respectively, indicating a slight increase in cooling rate with increasing feature thickness. Overall, cooling rates were lower in sample B200 in comparison with sample B120, which is in agreement with previous experimental results [33] and numerical simulations [33,34] of LPBF of 316L stainless steel.

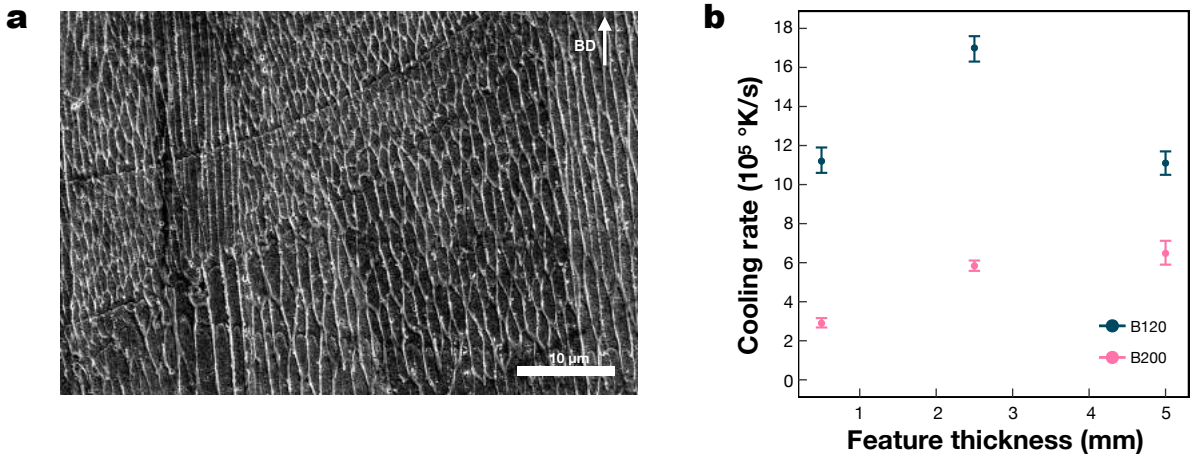

Figure 1.6. Solidification microstructure and cooling rates in SS316L builds. a) A representative scanning electron microscopy micrograph of the solidification microstructure. b) Cooling rates calculated based on primary dendrite arm spacing. Error bars represent 95% confidence intervals.

The analysis was further extended with an investigation of the effect of feature thickness on the phase composition and microsegregation within the as-printed samples. XRD analysis of samples B120 **(Figure 1.7, a)** and B200 **(Figure 1.7, b)**

revealed that the face-centered γ-austenite was the main phase present in the samples. Additionally, a diffraction peak indexed to the (110) set of lattice planes of the body-centered cubic δ-ferrite phase was observed at ~43.5° for all three leg thicknesses of sample B120, and this peak was most prominent for the 0.5 mm thick leg. Oval-shaped δ-ferrite particles were observed in the SE micrographs of the 0.5 mm thick leg of sample B120 **(Figure 1.7, c)** at the austenite cell boundaries. In sample B200, no clear peaks corresponding to the δ-ferrite phase were identified in the XRD patterns **(Figure 1.7, b)**, and no δ-ferrite particles were observed in the SE micrographs **(Figure 1.7, d)**.

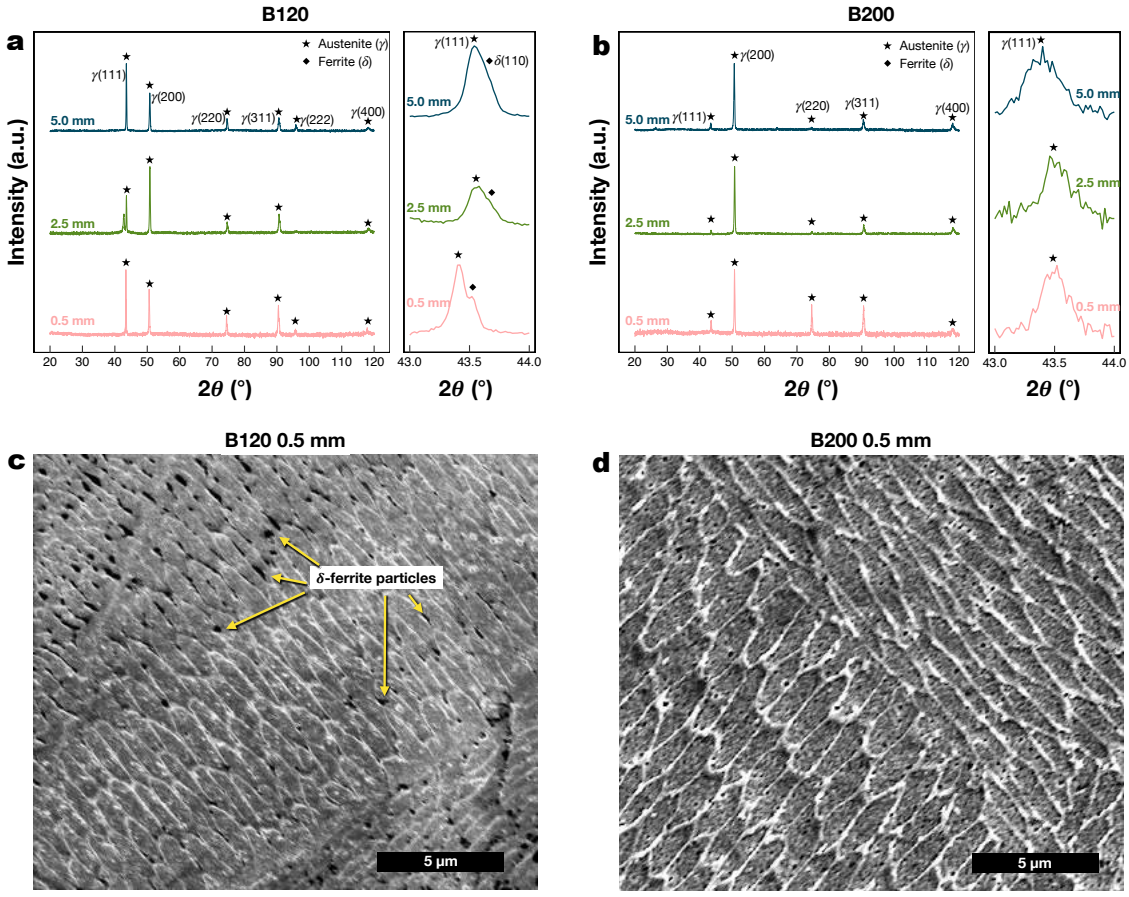

Figure 1.7. Phase composition of the as-printed SS316L samples: a) X-ray diffraction (XRD) patterns for sample B120, b) XRD patterns for sample B200, c) scanning electron microscopy (SEM) micrograph of the microstructure for the 0.5 mm thick leg of sample B120, d) SEM micrograph of the microstructure for the 0.5 mm thick leg of sample B200.

Presence of secondary phase particles at the cell boundaries was confirmed with conductive AFM (**Figure 1.8**). In C-AFM scans, secondary phase particles appeared as exhibiting higher current that were located between individual cells.

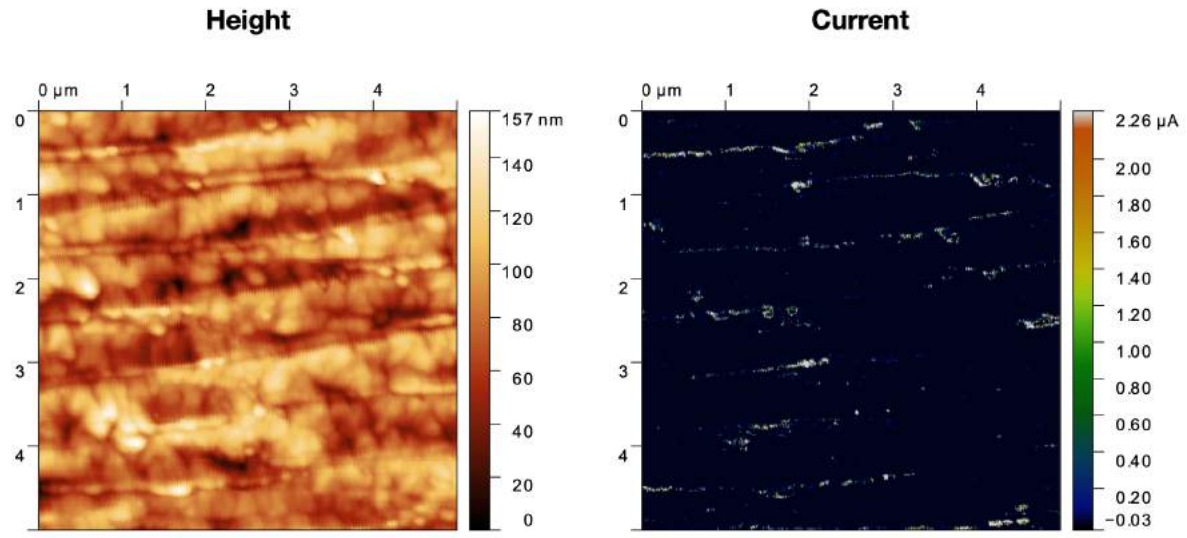

Figure 1.8. Conductive atomic force microscopy imaging of sample B120 2.5 mm. Bright spots in the current map indicate presence of ferrite particles at the cell boundaries.

Minor secondary phase precipitates were also observed in the as-printed samples (**Figure 1.9**). Irregularly-shaped, faceted secondary phase particles few hundred nanometers in size were located at the grain boundaries. The particles are likely to have $M_{23}C_6$ chromium-rich composition, as this carbide is known to nucleate and grow readily in austenitic stainless steels [46] , especially at the high-angle grain boundaries [47].

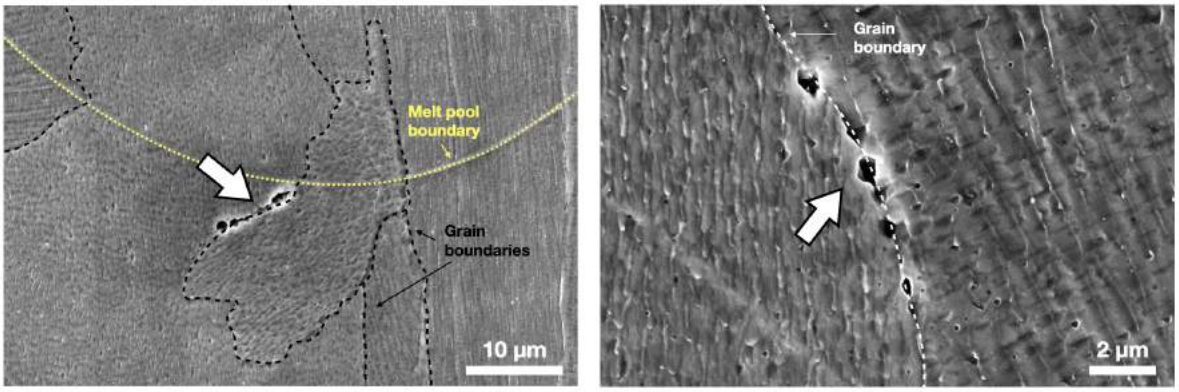

Figure 1.9. Scanning electron microscopy micrographs showing minor secondary phase precipitates (potentially $M_{23}C_6$ carbide) located at the grain boundaries of sample B120 (white arrows).

Finally, the influence of LPBF process parameters and local part geometry on local plastic deformation within the as-printed parts was investigated. IPF EBSD maps and the corresponding KAM maps for sample B120 are shown in **Figure 1.7, a**. The mean KAM values were 0.30 °, 0.26 ° and 0.28 ° for the 0.5, 2.5 and 5.0 mm thick legs, respectively, indicating no trend in KAM as a function of leg thickness in sample B120. IPF maps and the corresponding KAM maps for sample B200 are shown in **Figure 1.7, b**. The mean KAM values were 0.24 °, 0.25 ° and 0.33 ° for the 0.5, 2.5 and 5.0 mm thick legs, respectively. In contrast to sample B120, a correlation between feature thickness and KAM was observed in sample B200, with thicker feature exhibiting higher KAM values.

Plots of the GND density distributions for sample B120 are shown in **Figure 1.10, c**. Median GND density values were calculated to be 3.38 x 10^{13}, 2.93 x 10^{13} and 3.02 x 10^{13} m^{-2} for the 0.5, 2.5 and 5.0 mm thick legs, respectively. For sample B200, the GND density distributions are shown in **Figure 1.10, d**, and median GND density values were calculated to be 2.29 x 10^{13}, 2.63 x 10^{13} and 3.33 x 10^{13} m^{-2} for the 0.5, 2.5 and 5.0 mm thick legs, respectively. Overall, the largest GND density of 3.33 x 10^{13} m^{-2} was observed in the 5.0 mm thick leg of sample B200.

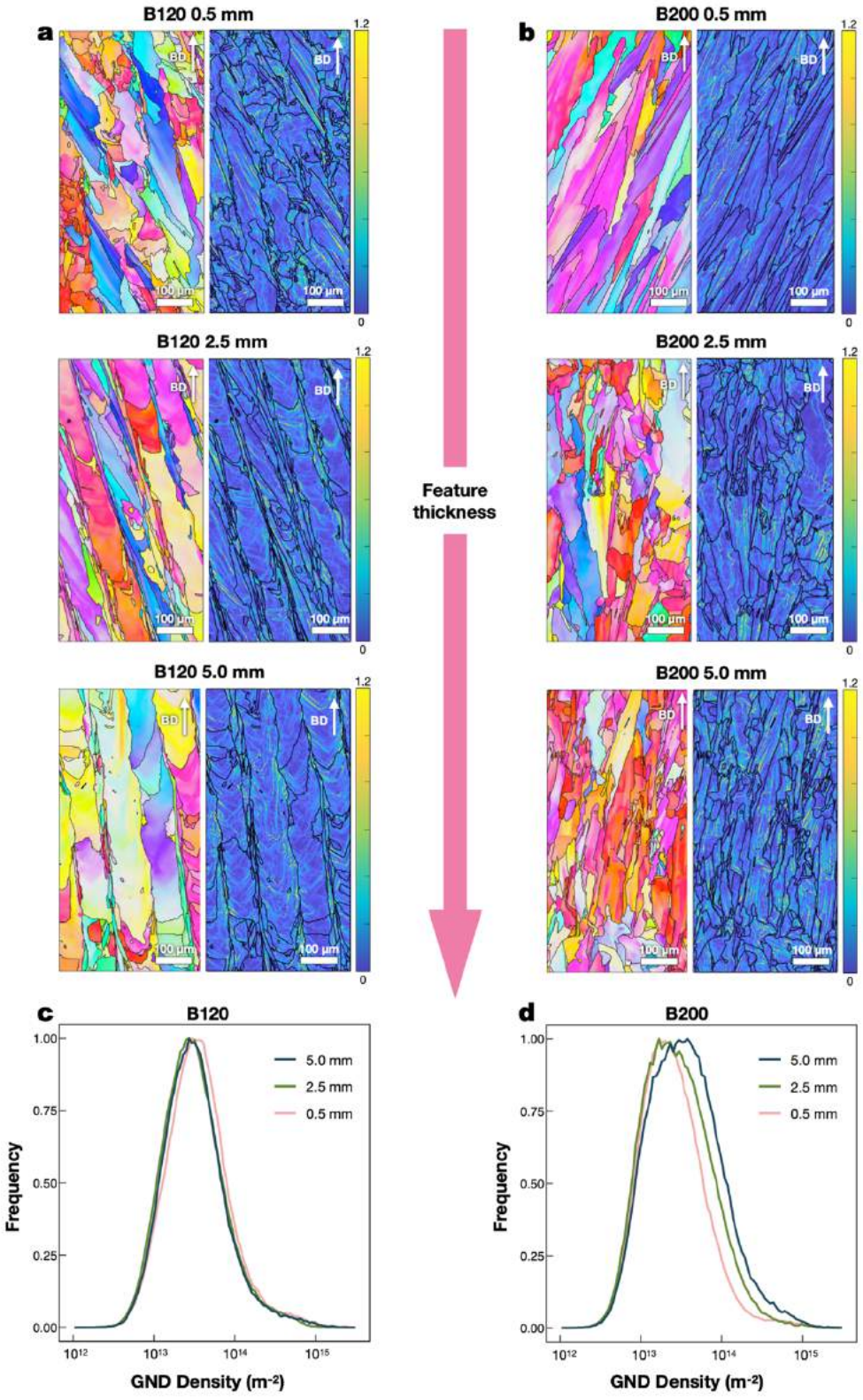

Figure 1.10. Local plastic deformation within the as-printed samples. Inverse pole figure maps and the corresponding kernel average misorientation maps for a) sample B120, and b) sample B200. Frequency polygons showing distributions in the density of geometrically necessary dislocations for c) sample B120, and d) sample B200.

1.4 Discussion

All key microstructural characteristics of the samples obtained from the SEM and EBSD analyses are summarized in **Table 1.3**. Both LPBF-printed benchmark parts investigated in this work exhibited cellular microstructures typical for additively manufactured 316L stainless steel **(Figure 1.7, c-d)** [48], with cell boundaries formed via microsegregation of Mo and Cr [49–51]. For sample B120, the solidification mode was primary austenite with second-phase intercellular dendrite [52,53], with oval-shaped ferrite particles observed at the cell walls and triple points **(Figure 1.7, c)**. Presence of δ-ferrite in sample B120 was additionally confirmed with XRD analysis **(Figure 1.7, a)**, where the (110) peak of δ-ferrite was observed, and AFM scanning (**Figure 1.8**). In contrast to sample B120, retained δ-ferrite was not detected in sample B200 **(Figure 1.7, b and Figure 1.7, d)**. Absence of XRD peaks attributed to δ-ferrite indicates that either there is no retained δ-ferrite present in sample B200, or it is present in amounts below the ~3 vol.% detection limit of the laboratory XRD [54]. Overall, the two-phase austenite-ferrite microstructure observed in sample B120 is not surprising. Based on the chemical composition of the feedstock powder (**Table 1.1**) and Schaeffler equivalency relationships [55], a nickel equivalent Ni_{eq} of 11.9-15.9 and a chromium equivalent Cr_{eq} of 19.5-22.5 can be expected for 316L stainless steel used in this work. Based on the Schaeffler diagram [55] and the values of Ni_{eq} and Cr_{eq}, the material is predicted to contain both austenite and ferrite, with the amount of δ-ferrite dependent on the alloy composition. A rough estimation of the amount of δ-ferrite can be obtained from Seferian's relationship [56,57], which yields ~3.0-5.2 vol.% of δ-ferrite. Preferential formation of intercellular dendrite in sample B120 as compared to sample B200 can be attributed to the higher cooling rates observed in sample B120 (**Figure 1.6, b**), which potentially suppressed the ferrite to austenite

transformation [58]. Thus, our analysis of phase composition suggests that phase formation control via manipulation of LPBF process parameters is possible in 316L stainless steel and other materials that exhibit multiple phases.

Table 1.3. Summary of the key microstructural parameters depending on the feature size. Cooling rates, grain areas and grain aspect ratios are reported as mean values ± 95% confidence intervals.

Sample ID	Feature thickness (mm)	Cooling rate (10^5 °K/s)	Grain area (μm²)	Grain aspect ratio	Mean KAM (°)	Median GND density (10^{13} m^{-2})
B120	0.5	11.20 ± 0.70	718 ± 102	3.26 ± 0.20	0.30	3.38
	2.5	17.00 ± 0.60	764 ± 188	5.31 ± 0.29	0.26	2.93
	5.0	11.10 ± 0.60	912 ± 208	4.87 ± 0.28	0.28	3.02
B200	0.5	2.90 ± 0.26	1936 ± 483	4.94 ± 0.39	0.24	2.29
	2.5	5.84 ± 0.27	922 ± 181	3.19 ± 0.17	0.25	2.63
	5.0	6.48 ± 0.64	546 ± 65	3.37 ± 0.13	0.33	3.33

*KAM – kernel average misorientation; GND – geometrically necessary dislocations.

Grain area and morphology were found to be a function of feature thickness for both samples. For sample B120, grain area increased from ~992 μm² for the 0.5 mm leg to ~1576 μm² for the 5.0 mm leg **(Figure 1.10, a)**, which constituted a ~59% increase in grain area. An opposite trend was observed in sample B200, where grain area decreased ~2741 μm² in the 0.5 mm leg to 811 μm² in the 5.0 mm leg **(Figure 1.10, b)**, or a ~70% decrease. The trend observed in sample B200 is in agreement with the calculated cooling rates **(Figure 1.5, b)**, where an increase in cooling rate with increasing feature thickness was observed. However, cooling rates alone cannot explain the grain structure evolution observed in sample B120, suggesting that other factors (e.g., solidification rate [48] or temperature gradient [59]) have a dominant influence on grain growth in this sample.

Based on the Hall-Petch relationship [60,61] and the observed grain sizes (**Figure 1.5, c**), a strong dependence of the mechanical properties on the feature size

can be expected in sample B200. We can speculate that in sample B200, strength should be proportional to the feature size, as larger features tended to exhibit smaller grain sizes. Similarly, some variation in strength can be expected in features of different thickness within sample B120, with thicker features exhibiting a slightly decreased strength.

Large, columnar grains spanning tens of layers were observed in the 2.5 and 5.0 mm thick legs of sample B120 **(Figure 1.5, a)** and in the 0.5 mm thick leg of sample B200 **(Figure 1.5, b)**. Similar grain structures were previously reported for Inconel 625 parts fabricated for the AM Bench challenge [28], as well as LPBF-printed SS 316L [62,63] and CrMnFeCoNi high entropy alloy [62] samples. Highly anisotropic grain structures observed in these samples can potentially cause significant anisotropy in mechanical properties [64], fatigue performance [65,66] and corrosion resistance [67], and therefore should be avoided.

Grain growth direction was also influenced by the feature thickness. In sample B200, inclined grain orientations were observed in the 0.5 mm thick leg, while the 2.5 and 5.0 mm thick legs exhibited largely vertical grain orientations **(Figure 1.5, b).** The observed differences in grain growth directions in sample B200 can be attributed to differences in melt pool depth **(Figure 1.4, a)** [38]. A deeper melt pool (~23 μm deep) observed in the 0.5 mm thick leg produced highly inclined grains, and a shallower melt pool (~14 μm deep) observed in the 5.0 mm thick leg generated grains oriented along the build direction.

Dislocation substructures and GND densities were found to depend on LPBF process parameters and feature thickness. In both samples, high-KAM regions were observed within the grains, indicating agglomeration of dislocations and formation of low angle grain boundaries [68] **(Figure 1.10, a-b)**. For sample B120, high-KAM lines were observed to form V-shaped channels **(Figure 1.10, a, middle and right)**,

while this behavior was not detected in sample B200 **(Figure 1.10, b)**. GND densities were lognormally distributed within both samples **(Figure 1.10, c and d)** in agreement with previously published work [69]. In sample B120, no clear relationship between feature thickness and GND density was identified **(Figure 1.10, c)**, suggesting similar plastic deformation in features of all three thicknesses at the resolution afforded by EBSD mapping employed in this work. In contrast, in sample B200, GND density increased with feature thickness **(Figure 1.10, d)**, indicating accommodation of higher thermal stresses through plastic deformation in features of larger thickness. To elaborate the evolution of strain and GND density in LPBF-printed parts, further investigation via high-resolution EBSD [68] or precession electron diffraction (PED) is needed.

1.5 Conclusions

The influence of the local part geometry and LPBF process parameters on the microstructure of additively manufactured 316L stainless steel was explored. An extensive microstructural characterization of two LPBF-printed AMB2018-01 benchmark parts (sample B120, printed at a volumetric energy density (VED) of ~120 J/mm^3, and sample B200, printed at a VED of ~200 J/mm^3) was performed. The benchmark parts contained features of three thicknesses: 0.5 mm, 2.5 mm and 5.0 mm. Specific finding are as follows:

1. Dimensional accuracy of LPBF-printed benchmark parts depended on the process parameters, with larger VED used during printing causing larger deviations from the input CAD geometry.
2. Evaluation of the melt pool geometry via optical microscopy showed that melt pool size varied with feature thickness. In sample B200, melt pool depth was inversely proportional to the feature thickness, while in

sample B120 no direct relationship between feature thickness and melt pool depth was established. For both samples, melt pool width decreased with increasing feature thickness.

3. Melt pool depth, in turn, influenced grain growth direction within sample B200, where a shallower melt pool produced grains oriented along the build direction, and a deeper melt pool generated grains inclined with respect to the build direction.
4. No influence of feature thickness on phase composition was established. However, LPBF process parameters influenced the amount of retained δ-ferrite present within the samples: lower energy input used in sample B120 caused higher cooling rates and promoted suppression of the ferrite-austenite transformation; no δ-ferrite was observed in sample B200.
5. The relationship between grain morphology and feature thickness was highly dependent on the LPBF process parameters. In sample B120, an increase in feature thickness caused an increase in grain size, while an opposite trend was observed in sample B200.
6. Finally, density of geometrically necessary dislocations (GND)s was dependent on feature thickness in sample B200, where thicker features exhibited higher values of GND density, suggesting larger plastic deformation.

Overall, the present findings demonstrate that local part geometry has a significant influence on the solidification and grain microstructure of LPBF-printed parts. Microstructure within features of different thickness was found to be dependent on the LPBF process parameters (e.g., VED). Therefore, in complex parts where both thick and thin features are present, microstructural homogeneity can be achieved by

locally tailoring the LPBF process parameters, potentially eliminating the need for post-print heat treatment.

CHAPTER 2 IMMISCIBLE ALLOYS FOR RESIDUAL STRESS MITIGATION IN DIRECTED ENERGY DEPOSTION

2.1 Introduction

Metal additive manufacturing (AM), often referred to as metal 3D printing, is a family of disruptive manufacturing technologies that allow for rapid, on-demand fabrication of high-quality near-net-shape metal components. Metal AM has been successfully adopted by the medical [70,71] and aerospace [72,73] industries, where custom, geometrically complex metal parts are required. Over the last 15 years, there has been a rapid increase in the intensity of research and development activities related to metal AM, both in academia and industry, as evidenced by the remarkable growth of annual number of patents and scientific publications **(Figure 2.1)**. Such a keen interest of the metallurgy and manufacturing communities can be attributed to metal AM's capability to significantly reduce lead times, enabling efficient and rapid iterations in design and testing [74]. Additionally, metal AM allows for considerable part count reductions in assemblies [75–77], as well as light-weighting through part geometry optimization [16].

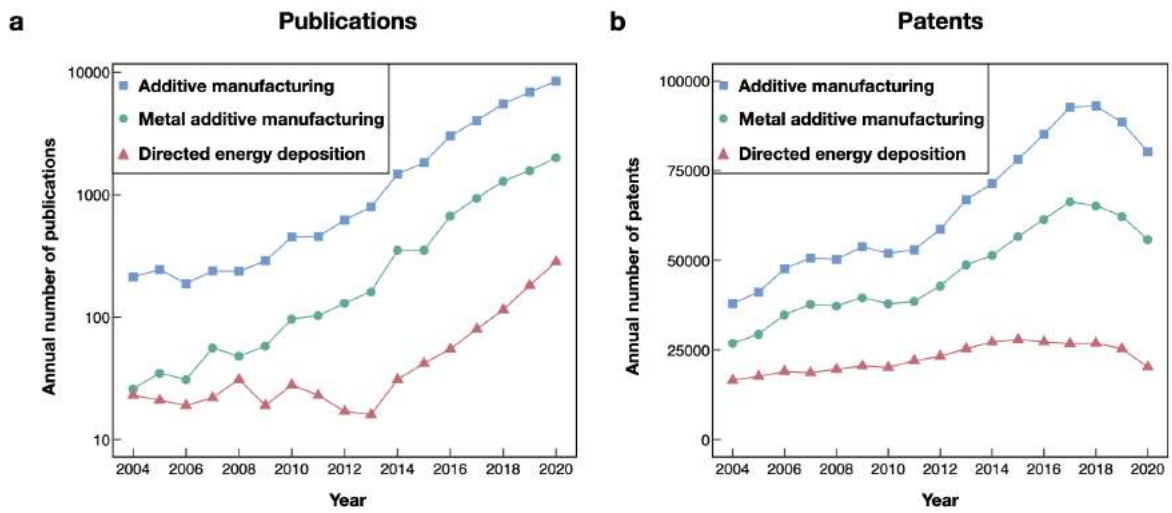

Figure 2.1. Trends in metal additive manufacturing research and intellectual property. a) Annual number of publications (note the logarithmic scale on the y axis). b) Annual number of published patents. Data collected from Scopus for scientific publications and from Espacenet for worldwide patents.

In contrast to conventional manufacturing processes, in metal AM a part is built up from the feedstock material (e.g., powder or wire) layer-by-layer based on a computer aided design (CAD) model [38]. The most frequently used metal AM techniques are powder bed fusion (PBF) and directed energy deposition (DED). In a typical PBF process, a thin layer of feedstock powder is spread uniformly across the build platform by a roller or a recoater, and a focused energy source is scanned along the CAD-defined path, melting the powder particles **(Figure 2.2, a)**. The build platform is then lowered, and the process is repeated for the next layer. In DED, the feedstock material is delivered directly to the melt pool formed by a focused energy source (laser/electron beam or arc plasma) as shown in **Figure 2.2, b**. While PBF commonly has higher dimensional accuracy and yields parts with smaller surface roughness [38], DED has multiple unique advantages over PBF **(Figure 2.2, c-f)**: 1) DED enables higher deposition rates (up to 2.5 kg/h for DED versus 0.25 kg/h for PBF [78]), 2) DED has an inherent capability for multi-material deposition (e.g., *in situ* alloying [79]) and fabrication of functionally graded structures [80,81], 3) DED

systems can be adapted to fabrication of coatings [82,83] and repair of damaged parts [84,85], and 4) DED enables processing of large (>1000 mm^3) part volumes [86].

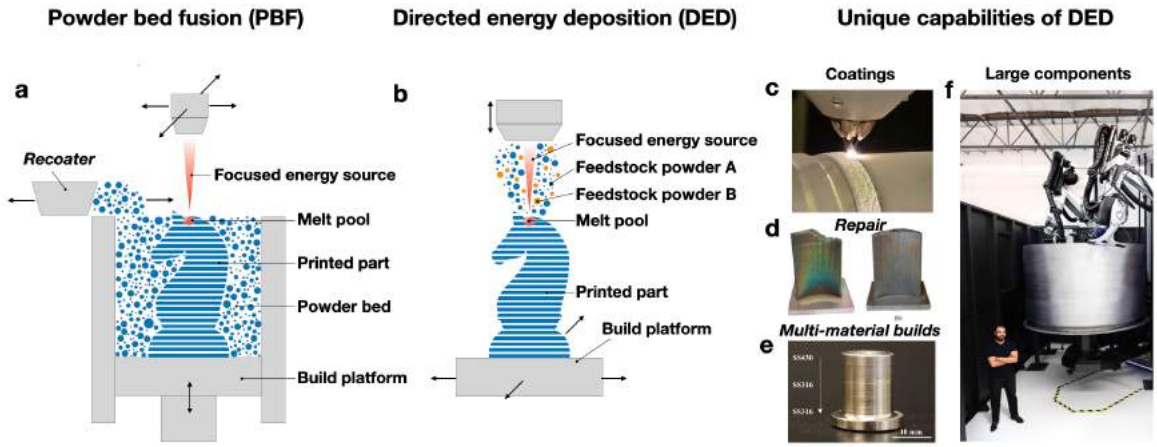

Figure 2.2. Metal additive manufacturing technologies. a) A schematic of the powder bed fusion process. b) A schematic of the directed energy deposition (DED) process. c) Application of DED in coatings (image courtesy Optomec). d) Repair of a DED-fabricated 316L stainless steel turbine blade [84]. *e) A functionally graded magnetic-nonmagnetic bimetallic structure fabricated via DED* [80]. *f) A large aerospace component fabricated by a custom DED-based process (image courtesy Relativity Space).*

While DED in its core principles is similar to welding, it presents a variety of unique technical and scientific challenges. Microstructures of DED-deposited alloys usually exhibit highly elongated grains and preferred crystallographic orientations [87], leading to significant non-uniformities in mechanical properties [88]. Moreover, high cooling rates of up to 10^5 K/s [89] combined with the layer-by-layer nature of DED processing that subjects the material to repeated thermal cycles can cause complex phase transformations [90] and formation of detrimental residual stresses [91]. This chapter discusses an investigation of the effect of alloy composition on the residual stresses introduced during DED.

2.1.1 Residual stress in directed energy deposition

Thermal and thermomechanical processing of metals brings about complex interactions between thermal gradients, elastic or inelastic strains/stresses, and microstructure **(Figure 2.3)**, inevitably resulting in the introduction of residual stresses [92,93]. For example, in martensitic stainless steel weldments, the residual stress state (i.e. compressive/tensile character and magnitude) depends on the expansion introduced by the austenite-to-martensite transformation, as well as on the thermal shrinkage during cooling [94]. However, the martensite start temperature is, in turn, influenced by the principal residual stresses.

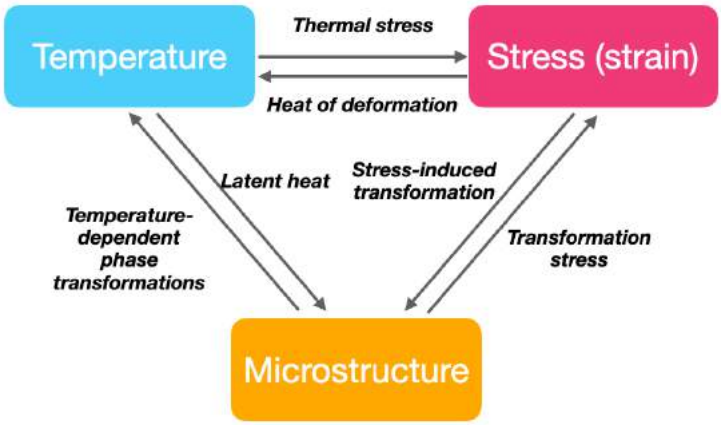

Figure 2.3. A schematic diagram showing the coupling phenomena between temperature, stress/strain fields and microstructure in metallic components. Adapted from [93].

DED is a non-equilibrium processing technique with fast cooling rates of 10^2-10^4 K/s [95–99] and thermal gradients on the order of 10^4-10^5 K/m [100,101] **(Figure 2.4, c)**. Due to the layer-by-layer nature of the process, the part goes through a highly complex thermal history, which includes melting, remelting and reheating of the material [96,98,100,102–105] **(Figure 2.4, b)**. This can lead to complicated phase transformations and microstructural changes [96,97]. As a consequence, the residual

stresses that are introduced by DED can be highly nonuniform and often have high gradients up to ~10^2 MPa/mm [106,107]. Residual stresses in DED-fabricated parts, which often have tensile character, can cause a multitude of issues, including: distortion [102], cracking [108,109], delamination of parts from the substrate [108], early crack propagation under cyclic loading [110,111], and, as a result, premature failure of structural components. Understanding, predicting and mitigating residual stresses in DED parts is, therefore, of great importance.

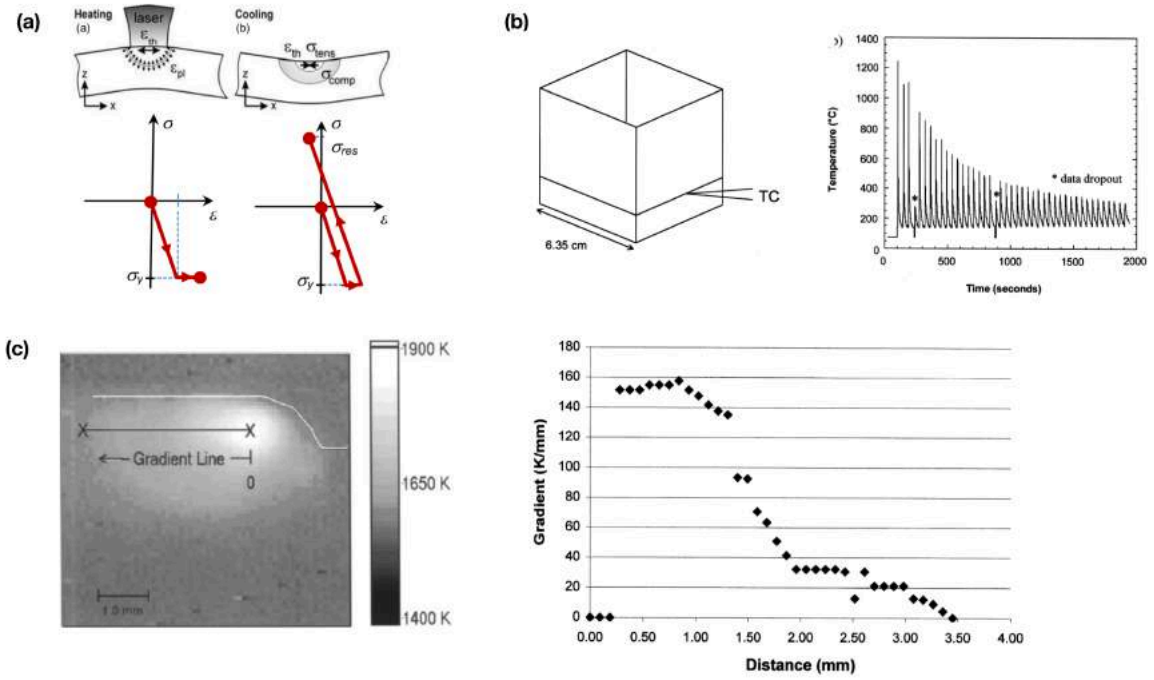

Figure 2.4. Origin of residual stress in directed energy deposition (DED). (a) Thermal residual stress formation model: heating phase (left) and cooling phase (right) [112]. *(b) Thermocouple placement (left) and thermocouple response (right) during DED fabrication demonstrating complex thermal history of the printed part* [100]. *(c) Digital image of the molten pool during laser DED of stainless steel 316 (left) and temperature gradient along the gradient line (right) demonstrating large temperature gradients during DED* [100].

2.1.2 Measurement of residual stress

Residual stress measurement is a non-trivial task, as no methods for direct stress measurements currently exist. Calculation of residual stresses requires acquisition of some other measurable quantities, e.g. displacement/distortion, lattice

spacing, or speed of sound. Residual stress measurement techniques are typically classified into destructive and non-destructive. Destructive techniques are based on mechanical stress relaxation and include hole drilling, serial sectioning, and ring-core drilling. Non-destructive techniques are based on measuring lattice spacing (diffraction techniques), speed of sound, or Barkhausen noise (sound emitted by a ferromagnetic material under external magnetizing field). When choosing a technique for residual stress measurement, there is a tradeoff between cost, speed, and resolution **(Table 2.1)**. Moreover, most approaches are based on a series of assumptions, and care needs to be taken to make sure these assumptions are valid for the investigated component. A detailed review of residual stress measurement techniques can be found in [113–117].

Table 2.1. Comparison of the main residual stress measurement techniques.

Method	Penetration depth	Spatial resolution	Advantages	Limitations	References
Hole drilling	~1-2 x hole diameter	~1.8 mm (typical hole diameter)	Inexpensive; portable equipment; fast; easy to perform the measurement	Semi-destructive; inapplicable in areas with high stress gradients; erroneous results possible in areas with $\sigma_{res} \geq 1/3\ \sigma_y$; flat surface required for strain gauge; strain hardening in the vicinity of the hole may happen during material removal, causing errors up to 70 MPa; phase-specific stresses cannot be inferred from the measurements; limited resolution	[113,114,116,117]
Laboratory X-Ray diffraction	~4-75 μm	~0.1-10 mm	Readily available; non-destructive; can infer phase-specific stresses	Surface sensitive technique; affected by surface roughness and flatness; affected by texture and grain size; need to know stress-free lattice spacing d_o; need to know X-ray elastic constants; use of Cu Kα radiation in alloys containing Fe, Cr or Ti can result in fluorescent background	[114,115,118]
Synchrotron X-ray diffraction	~0.1-40 mm	~ 5-10 μm	High spatial resolution; nondestructive; can infer phase-specific stresses; does not activate the material after the experiment; fast	Need to know stress-free lattice spacing d_o; need to know X-ray elastic constants; only available at national user facilities; low penetration depth as compared to neutrons	[114,118]
Neutron diffraction	~1-10 cm	~1 mm (down to ~250 μm in pinhole neutron diffraction)	High penetration depth; nondestructive; can infer phase-specific stresses	Few diffraction peaks acquired per scan; only available at national user facilities; low data acquisition rate; special handling requirements for activated samples; need to know stress-free lattice spacing d_o; need to know elastic constants; low spatial resolution as compared to hard X-rays	[114,118–120]
Ultrasonic	> 10 cm	~ 5 mm	Inexpensive; portable equipment; non-destructive; fast	Microstructure sensitive; limited resolution; bulk measurement over large volume	[113,114]
Barkhausen noise	~ 0.2 mm	~ 5-10 mm	Fast; portable; non-destructive; high penetration depth	Ferromagnetic materials only; requires calibration; microstructure sensitive	[113,121]

2.1.3 Mitigation of residual stress in additive manufacturing

One of the most popular approaches for residual stress reduction is heating of the substrate, build chamber, and the printed part during deposition. This allows for a reduction of thermal gradients in the part during printing, minimizing the accumulated residual stresses. Corbin et al. [122] demonstrated that preheating of the substrate to ~400 °C can reduce the substrate distortion accumulated during printing of the first layer by 27.4%. Lu et al. [102] developed a 3D thermo-mechanical finite element (FE) model to study distortions and residual stresses induced by DED. Their findings indicate that when substrate preheating is combined with build chamber heating, both the residual stresses and distortions can be reduced by up to 80.2 and 90.1%, respectively **(Figure 2.5, a)**. Vasinonta et al. [123] also formulated a thermo-mechanical model to study the effect of temperature gradients, as well as part and baseplate preheating on the residual stress of stainless steel parts fabricated by laser engineered net shaping (LENS®). Their results suggest that uniform part and baseplate preheating considerably reduces the residual stress. The maximum reduction of residual stress of ~40% was achieved by preheating the part and the baseplate to 400°C **(Figure 2.5, b)**. These studies show that pre-heating of the substrate, build chamber and the printed parts is an effective approach for residual stress mitigation; however, pre-heating does not lead to complete elimination of the residual stresses or to conversion of tensile residual stresses into compressive, and further post-processing might be required to achieve these goals.

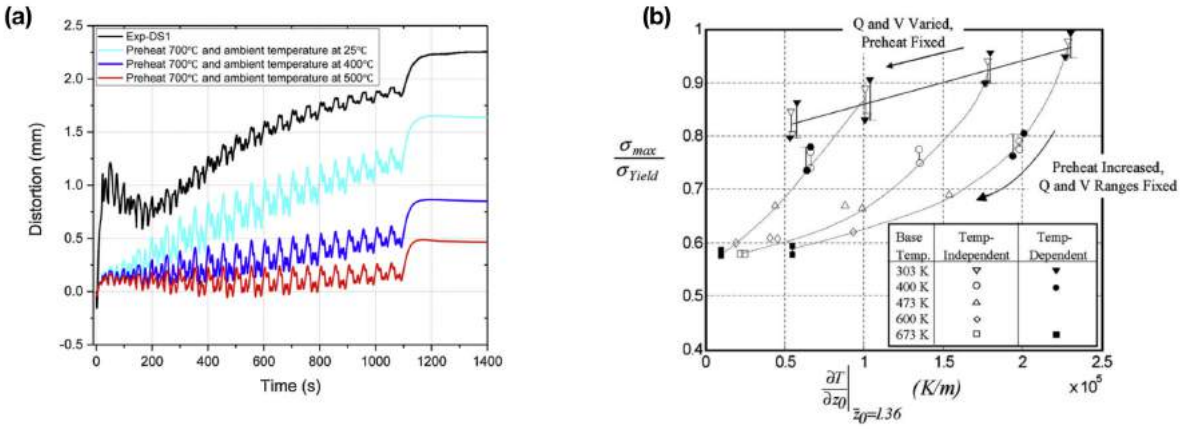

Figure 2.5. Influence of the preheating on the distortion and residual stress during DED. (a) Calculated distortion generated during laser directed energy deposition printing of Ti-6Al-4V. Preheating of the build chamber reduced the accumulated distortion [102]. *(b) Influence of the part and baseplate preheating and resulting thermal gradients on the residual stress. Higher preheating temperatures lead to lower thermal gradients and, consequently, lower residual stresses* [123].

Another approach for residual stress mitigation during printing is optimization of the scan strategy. Denlinger et al. [124] employed a series of *in situ* and post-process distortion measurements on Ti-6Al-4V and Inconel 625 L-DED parts to study the effect of interlayer dwell time on part distortion. They demonstrated that increasing the interlayer dwell time from 0 to 40 s allows for additional cooling during deposition and results in reduction of residual stress from ~710 MPa to ~566 MPa in Inconel 625. On the other hand, increasing dwell time from 0 to 40 s during printing of Ti-6Al-4V resulted in an increase of residual stress from ~98 MPa to ~218 MPa **(Figure 2.6, a)**. These findings demonstrate that development and evolution of residual stress is highly material-dependent due to the complex interplay between residual stress and microstructure (**Figure 2.3**). Specifically, differences in behavior of Inconel 625 and Ti-6Al-4V may be attributed to differences in phase transformations during printing. Woo et al. [125] investigated the influence of scan strategy on the residual stress in functionally-graded materials (FGM) prepared by L-DED. Results of the study show

that the range of stress $\Delta\sigma$ can be reduced from ~950 MPa for 0° hatch rotation, to ~680 MPa for 90° hatch rotation, and then further reduced to ~430 MPa for island or "checkerboard" strategy. Yu et al. [126] employed a fractal scanning strategy, where the layers were scanned following a Hilbert curve. They demonstrated that the parts printed with this strategy exhibited lower substrate deformations as compared to conventional scan strategies due to the quasi-symmetric temperature distribution at the end of deposition process and lower temperature gradients introduced by the fractal scanning strategy **(Figure 2.6, b)**. Ma and Bin [127] confirmed that fractal scan strategy leads to distortions ~55.7% lower than those produced by serpentine scan strategy in selective laser sintering. Interestingly, Strantza et al. [128] found that employing a widely popular "island" or "checkerboard" scan strategy in LPBF of Ti-6Al-4V in place of continuous scanning throughout the part can increase residual stresses, especially in surface areas of the printed component. They also observed higher cut-off deflections in the part printed using the "island" scan strategy. Overall, these studies demonstrate that scan strategy can have a large influence on the residual stresses and distortions in DED.

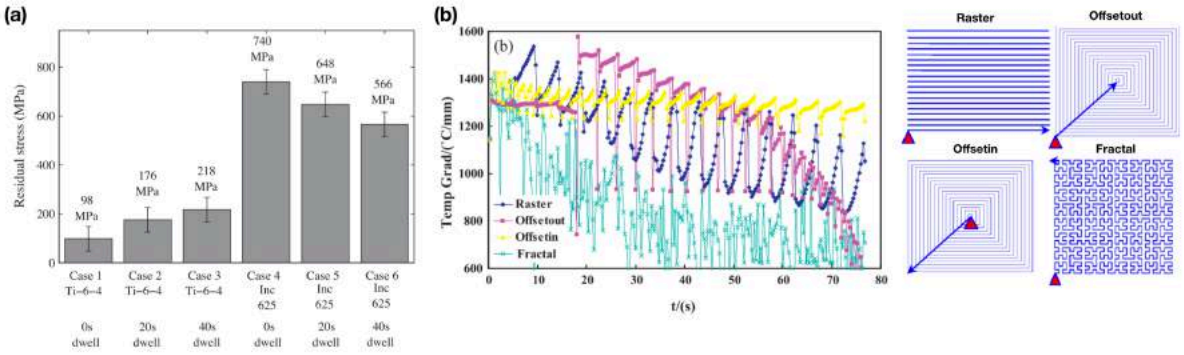

Figure 2.6. Residual stress mitigation by scan strategy optimization. (a) Influence of the interlayer dwell time on the residual stress in Inconel 625 and Ti-6Al-4V [124]. *Increased dwell time leads to lower residual stresses in Inconel 625, but higher residual stresses in Ti-6Al-4V. (b) Finite element analysis modeling results showing the influence of scan strategy on the temperature gradients during laser directed energy deposition* [126]. *Lowest gradients are obtained with a fractal scan strategy following a Hilbert curve.*

Residual stresses can be further decreased by post-print heat treatments. Stress relaxation induced by heat treatment of Inconel 625 parts was studied by compression tests with *in situ* neutron diffraction by Wang et al. [129]. In this work, stress relaxation in both additively manufactured and conventionally processed parts was quantified, and analysis of both macroscopic stress and stress in grains with different orientations was performed. The results indicate that at the same temperature and applied strain, additively manufactured Inconel 625 had a higher stress relaxation rate and lower peak and plateau stresses than conventionally processed Inconel 625, due to different texture and grain sizes in these two materials. Wang et al. [91] employed neutron diffraction and demonstrated that residual stress in laser-based DED-printed Inconel 625 parts can be relieved by heat treatment at 870 °C in Ar for 1 h. However, heat treatment also leads to precipitation of carbides, which in turn reduces the reference strain-free lattice spacing, leading to potential errors in computation of residual stresses. Zhang et al. [130] further analyzed the phase composition and precipitation kinetics of Inconel 625 at temperatures relevant to stress-relief heat treatments. Their findings indicate that elemental segregation caused by AM processing is the root cause for unusual precipitation behavior in heat-treated IN 625. These studies indicate that post-print heat treatment is an effective approach for residual stress relief, but alloy-specific strategies must be developed to avoid formation of undesirable phases.

Post-print surface treatments have been successfully employed to adjust the stress state of additively manufactured parts. Yamaguchi et al. [131] demonstrated that magnetic field assisted finishing (MAF) can reduce residual stresses on the surface of AM parts from ~200 MPa to ~-70 MPa, converting the tensile stress on the part surface into compressive. Guo et al. [132] used laser shock peening (LSP) as a post-print treatment to modify the surface stress in L-DED Ti-6Al-4V parts. This approach

allowed for modification of surface residual stresses from ~100 MPa to ~-200 MPa, as well as an increase of microhardness from ~361 HV to ~420 HV. Sun el al. [133] applied LSP to wire-arc additively manufactured (WAAM) 2319 aluminum alloy, demonstrating that compressive stresses of up to -100 MPa were introduced by LSP. LSP also dramatically increased the surface microhardness of the WAAM parts from ~75 HV to ~110 HV. These studies show that post-print surface modification can introduce surface compressive stresses, potentially improving the fatigue life of DED-printed parts.

2.1.4 Alloy engineering for residual stress mitigation in welding

As discussed above, most popular stress mitigation techniques in metal AM are based on adjusting process parameters, such as substrate/chamber temperature, scan strategy, or interlayer dwell time. These approaches are not capable of completely eliminating residual stresses or of converting detrimental tensile stresses into beneficial compressive stresses. An alternative approach to residual stress manipulation has been explored in welding of high strength steels. Instead of adjusting welding parameters, the composition of the well filler itself is changed to leverage the transformation strains associated with the austenite-to-martensite transformation.

Ohta et al. [134] investigated using a low transformation temperature (LTT) wire in welding of JIS SPV490 structural steel. They showed that adjusting the composition of welding wire allowed to reduce the martensite start temperature to from ~500 °C to ~180 °C. Lower martensite start temperature enabled expansion of the weld metal in the final stage of solidification, inducing compressive residual stress within the weld (**Figure 2.7, a**). In contrast, in a conventional welding wire, tensile residual stresses were observed within the weldment. Such a change in the residual stress character had a profound effect in fatigue performance of the welded material,

decreasing fatigue crack propagation rate throughout the investigated range of stress intensity factor (**Figure 2.7, b**).

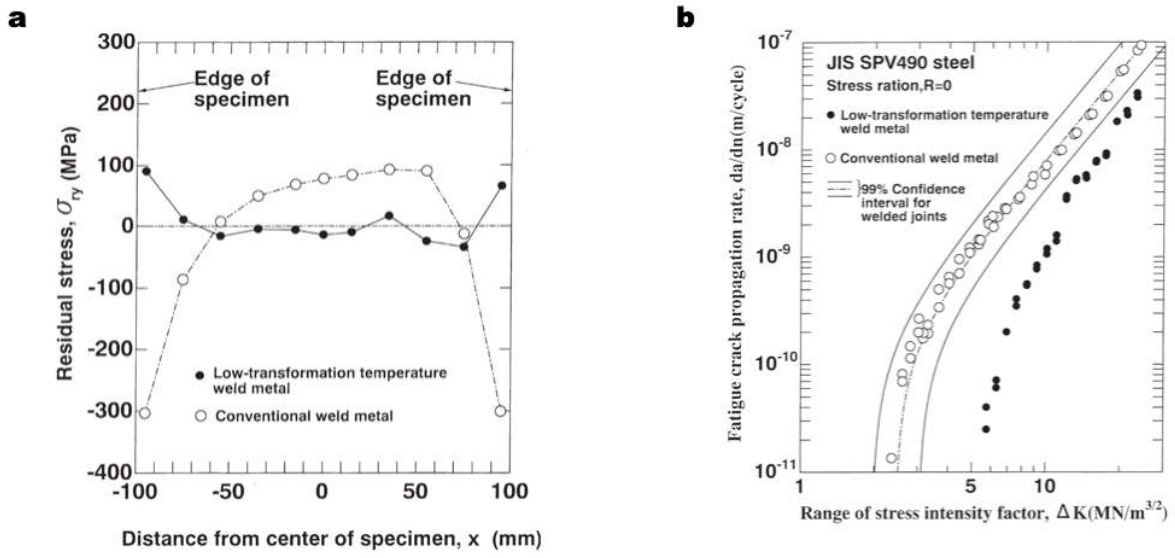

Figure 2.7. Effect of using a low transformation temperature (LTT) welding wire on residual stress [134]. *a) Comparison of residual stress distributions in weldments fabricated with LTT and conventional welding consumables. b) Using LTT weld metal significantly improved fatigue properties of the weld.*

A similar study was performed by Ramjaun and colleagues [135], who demonstrated that using a weld filler alloy that exhibits a low martensite start temperature of ~164 °C can influence residual stresses in weldments. They employed neutron diffraction residual stress measurements and showed that LTT welding alloy was capable of inducing compressive residual stress in both single- and multi-pass welds (**Figure 2.8**). However, steep stress gradients were still present within the welds

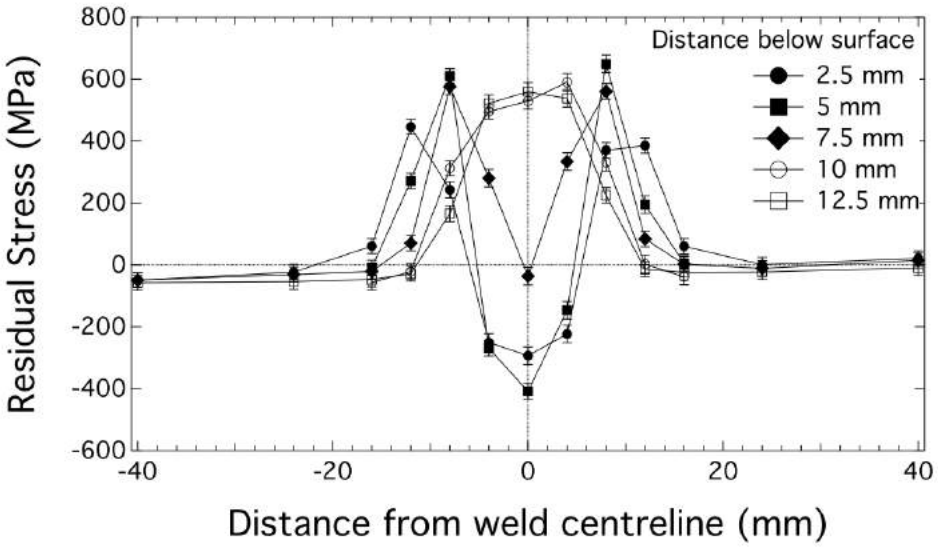

Figure 2.8. Distribution of residual stresses within a three-pass weld fabricated using a low transformation temperature wire [135].

An *in situ* synchrotron diffraction study of multi-pass LTT welds was performed recently by Dixneit et al. using time and spatially resolved angle dispersive XRD in transmission geometry [136]. They investigated LTT CrNi and LTT CrMn fillers, as well as the conventional filler for high strength steels, Mn_4Ni_2CrMo (**Figure 2.9, a**). The *in situ* setup has enabled investigation of lattice strains both at the root and at the final weld pass. In addition, use of diffraction for residual stress measurements enabled investigation of phase-specific strains within the γ, α_b and α' phases (**Figure 2.9, b**). Use of LTT fillers enabled reduction of the martensite start temperature from ~420 °C in conventional filler to ~ 240 °C in LTT CrNi and ~180 °C in LTT CrMn. In a conventional filler, high tensile lattice strains were observed within the austenite phase, and nearly-zero lattice strains were observed at room temperature within the martensite phase. In contrast, in both LTT CrNi and LTT CrMn, compressive lattice strains were observed upon cooling of both austenite and martensite. The authors speculate that, in LTT welds, the volume expansion caused by the austenite-to-

martensite transformation counteracted the strains formed due to restrained cooling of the material.

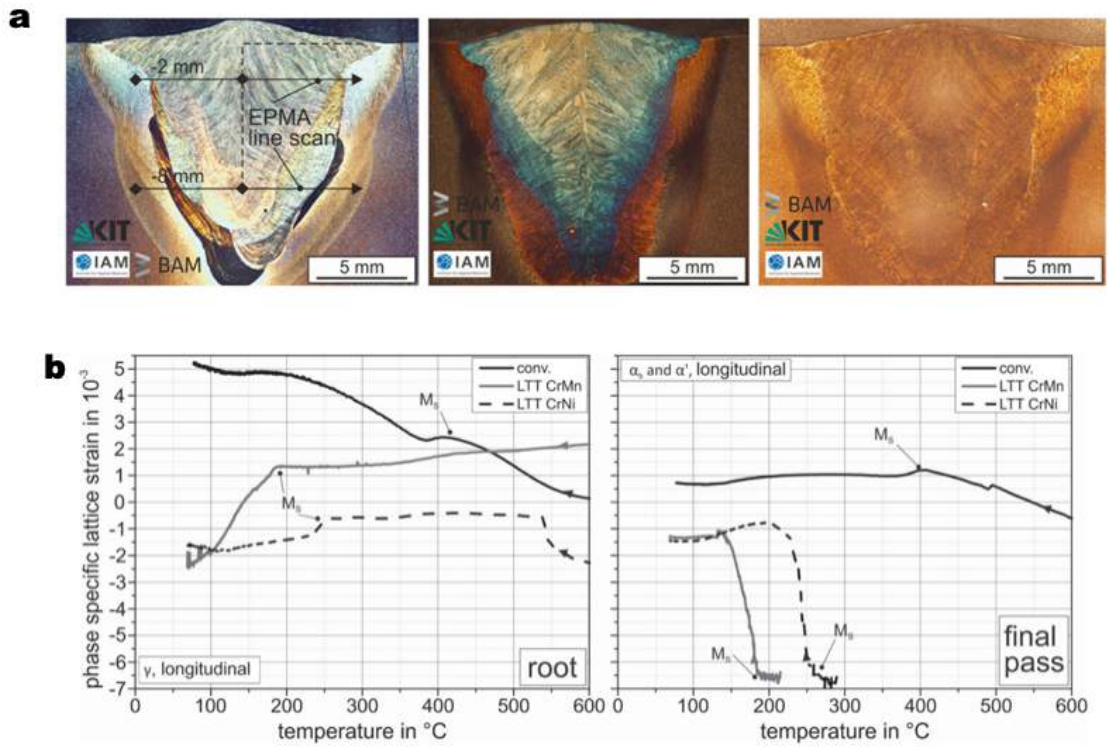

Figure 2.9. In situ synchrotron diffraction study of welding using transformation temperature (LTT) fillers [136]. *a) Optical micrographs of weld cross-sections of LTT CrMn (left), LTT CrNi (middle) and conventional (right) fillers. b) Phase-specific lattice strain within the LTT CrMn, LTT CrNi and conventional welds in longitudinal direction.*

To date, use of LTT alloys in AM has not been investigated. However, Chen et al. demonstrated Ar arc cladding of LTT powder [137]. They found high compressive residual stresses ranging from -229 MPa to -361 MPa within the clad coatings. In addition, LTT coating enhanced the hardness and wear resistance of the material.

2.2 Motivation and aims

In this work, we drew inspiration from the use of LTT materials in welding to demonstrate that solid-state phase transformations have crucial consequences for residual stress in metal AM parts. To investigate the effect of solid-state phase transformations, we compared two metals fabricated using DED: 1) pure Fe, and 2) Fe-50Cu (wt.%) binary alloy. The choice of these two materials was based on several considerations, discussed in detail below.

First and foremost, Fe and Fe-50Cu undergo different phase transformations upon cooling from the melt. As shown in the Fe-Cu binary phase diagram in **Figure 2.10, a** and Fe cooling diagram in **Figure 2.10, b**, pure Fe solidifies first as body-centered cubic (BCC) δ-Fe. It is then transformed into the face-centered cubic (FCC) austenite γ-Fe. Further cooling leads to a transition to BCC ferrite α-Fe. These BCC to FCC transitions are accompanied by a change in density and volume: density of δ-Fe at 1660 °C is 7.50 g/cm^3, density of γ-Fe at 912 °C is 7.70 g/cm^3, and density of α-Fe at 900 °C is 7.62 g/cm^3 [138,139]. Consequently, the $\delta \rightarrow \gamma$ transformation causes an ~3% decrease in volume, while the $\gamma \rightarrow \alpha$ transformation causes a ~1% increase in volume.

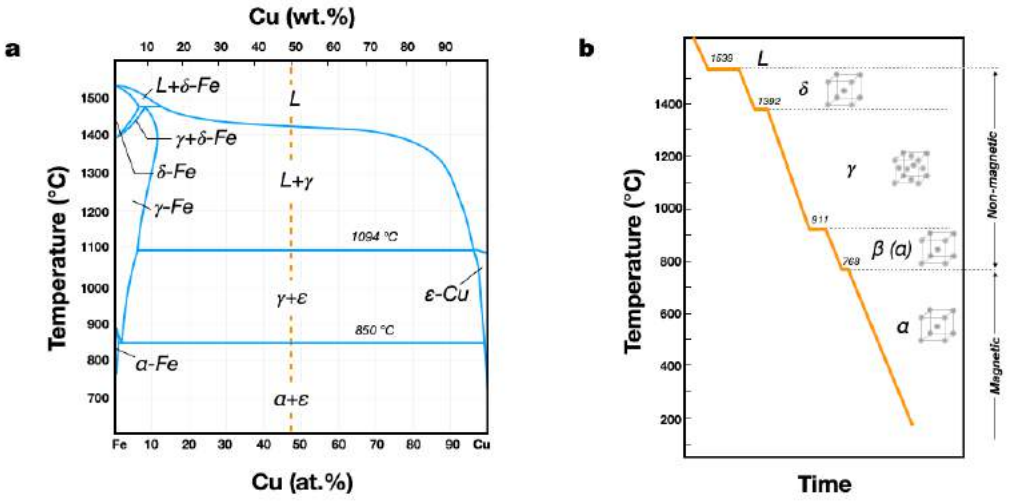

Figure 2.10. a) Binary Fe-Cu phase diagram, with dashed line indicating the Fe-50Cu (wt.%) composition. Adapted from [140]. *b) Cooling diagram of pure Fe.*

The phase transformation sequence of Fe-50Cu does not include δ-Fe: γ-Fe particles solidify directly within the liquid Cu-rich phase, and, upon cooling, the Fe-rich phase undergoes the $\gamma \rightarrow \alpha$ transformation. This means that the phase transformation accompanied by the decrease in volume is eliminated in Fe-50Cu, while the phase transformation accompanied by an increase in volume is preserved. We can therefore hypothesize that this last $\gamma \rightarrow \alpha$ transformation in Fe-50Cu will lead to formation of compressive residual stresses, similarly to the LTT welding wires discussed above, while parts fabricated from pure Fe will feature lower compressive or tensile stresses.

Second, Fe-Cu alloys possess a unique combination of high electrical and thermal conductivity with high strength and good plasticity [141–143]. However, a metastable miscibility gap that exists in the Fe-Cu system makes conventional processing (e.g., casting) of Fe-Cu alloys challenging. If the melt is undercooled into the metastable miscibility gap, it will decompose into two liquids, leading to formation of large spherical droplets of the minority phase within the majority phase (**Figure 2.11, b**). At low cooling rates, the minority phase droplets can aggregate, causing melt separation in Fe-Cu (**Figure 2.11, a**). As cooling rate increases, solidification structures become more refined, as demonstrated in **Figure 2.11, c** where electron beam melting with a cooling rate up to 10^5 °K/s was employed. In general, rapid solidification processes, such as gas atomization [144,145] and splat quenching [146], have been used to produce finely dispersed microstructures in Fe-Cu alloys. These processes, while successful at facilitating formation of fine solidification structures in Fe-Cu alloys, are expensive and not readily scalable.

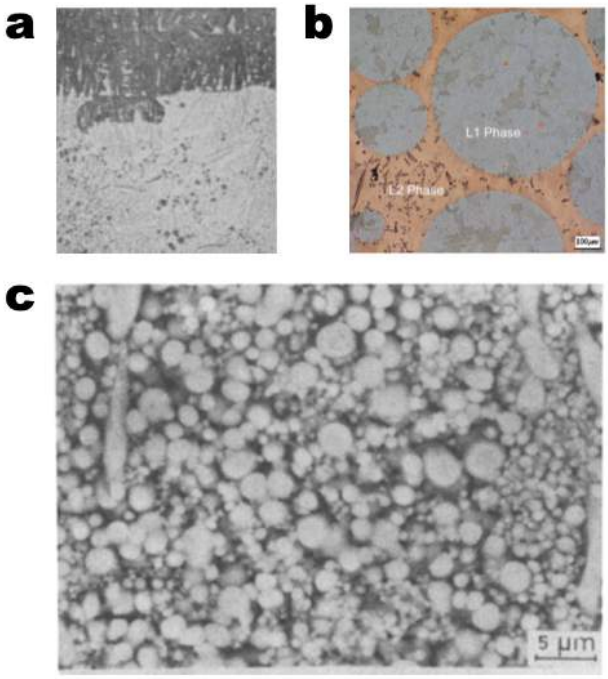

Figure 2.11. Solidification structures of Fe-Cu alloys. a) Scanning electron microscopy (SEM) image of a cast Fe-50Cu alloy exhibiting a clear junction between two phase-separated liquids [143]. *b) Optical micrograph showing spherical particles formed by liquid phase separation in Fe-Cu alloy* [147]. *c) A SEM micrograph of Fe-50Cu alloy fabricated via electron beam melting, showing fine distribution of the two phases* [148].

AM processing of Fe-Cu alloys can enable finely dispersed microstructures due to the large cooling rates inherent to metal AM. However, to date, few studies report AM of Fe-Cu alloys. Makarenko and Shishkovsky [149] demonstrated DED of multilayer functionally graded material (FGM) specimens fabricated from 316L stainless steel and aluminum bronze (10% Al). The SEM micrographs showed some evidence of liquid-phase separation with spherical Fe-rich particles of ~7 µm in diameter, as well as formation of Fe-rich dendrites and particles within the Cu-rich matrix. Additionally, round nanoscale porosity was observed within the samples. Osipovich et al. fabricated FGM structures based on 304 stainless steel and C11000 Cu alloy (99.9 wt% Cu) using the wire-fed electron beam technique. They also observed some liquid phase separation within the gradient/transition zone, with Fe-rich

particles within the Cu-rich matrix [150]. Interestingly, Vickers microhardness within the gradient zone was not significantly lower than microhardness of the pure steel zone. Recently, Zafari and Xia [142] demonstrated SLM of the Fe-20Cu (vol.%) alloy. They used mixed Fe and Cu powders as the feedstock material. The major finding of this study is that in SLM-printed Fe-Cu, formation of large columnar grains typical for AM was suppressed, and small nearly-equiaxed grains with a median grain size of 138 nm were observed (**Figure 2.12, c**). SLM-fabricated Fe-20Cu exhibited a compressive yield strength of ~900 MPa, while SLM-fabricated Fe demonstrated a compressive yield strength of ~400 MPa. This strengthening by a factor of 2.25 was attributed to the presence of nano-sized (~5 nm) Cu particles that provided dispersion strengthening.

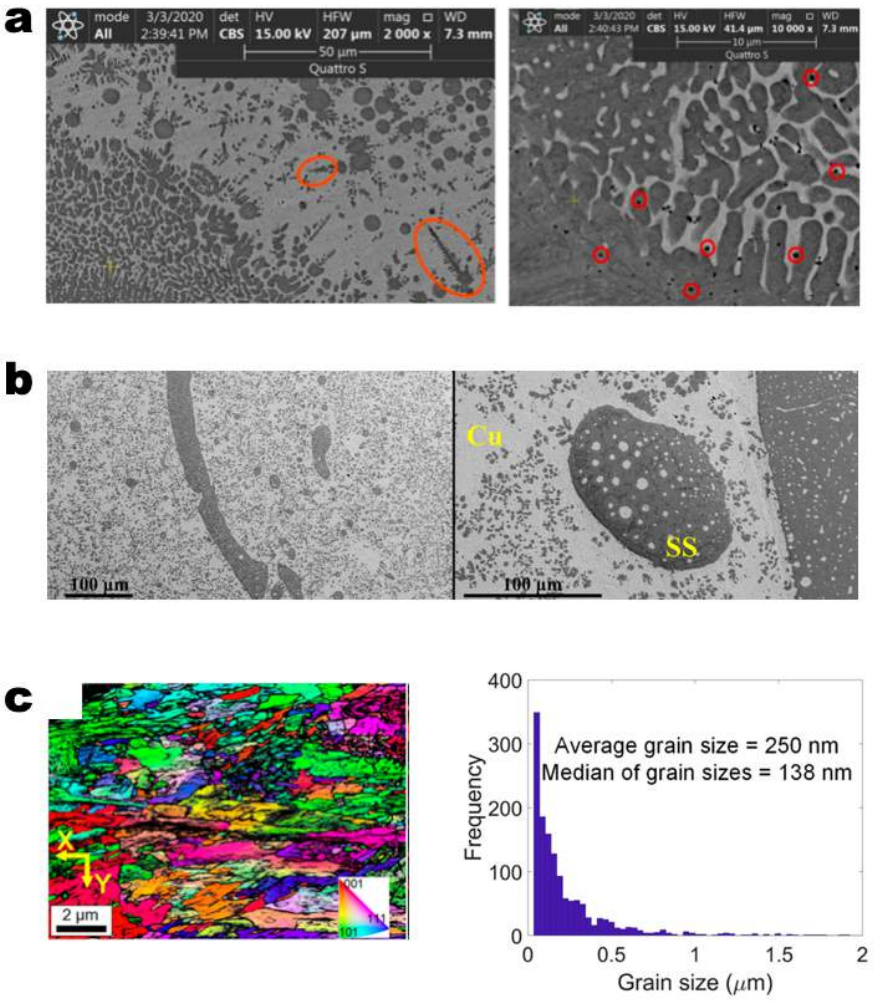

Figure 2.12. Additive manufacturing of Fe-Cu alloys. a) Scanning electron microscopy micrographs of a stainless steel 316L – aluminum bronze functionally graded material (FGM) [149]. *b) 304 stainless steel and C11000 Cu FGM fabricated via electron beam melting* [150]. *c) Selective laser melting of Fe-20Cu produced parts with highly refined grains* [142].

In this work, we use DED to fabricate samples from pure Fe and Fe-50Cu (wt.%) binary alloy. By comparing residual stresses formed within the two alloys, we demonstrate that the solid-state transformation play an important role in formation of residual stresses in AM-fabricated parts. Moreover, we show that DED is a feasible technique for fabrication of highly dense Fe-Cu parts with finely dispersed microstructures unattainable by conventional materials processing approaches.

2.3 Materials and methods

Test samples (10 x 10 x 10 mm cubes) were fabricated using an Optomec 750 laser engineered net shaping (LENS®) (Optomec, Albuquerque, NM, USA) system equipped with a 1kW 1064 nm YLR continuous wave laser (IPG Photonics, Oxford, MA, USA). The deposition chamber was kept in an inert Ar atmosphere, with oxygen level continuously monitored an maintained at <20 ppm. Samples were deposited onto a ASTM A36 low-carbon steel substrate plate of 6.35 mm in thickness. Spherical gas-atomized powders of Fe and Fe-50Cu (wt.%) powders with nominal particle diameters of 38-150 μm were used as a feedstock material (TLS Technik GmbH & Co. Spezialpulver KG, Bitterfeld-Wolfen, Germany). A total of 18 samples (9 samples for Fe and 9 samples for Fe-50Cu) were fabricated to separate the effect of alloy composition and process parameters on the residual stresses. The process parameter sets producing nearly fully-dense samples were determined through a series of preliminary experiments as detailed below. For all samples, the layer thickness was set to 0.254 mm, hatch spacing was set to 0.4064 mm and working distance was set to ~13.7 mm to produce a laser spot 0.7 mm in diameter.

The porosity of printed samples was measured using optical microscopy (OM) with the BX53M microscope (Olympus, Shinjuku, Tokyo, Japan). The images were then processed using ImageJ software (NIH), and the total porosity was determined as fraction of the porosity area to the total cross-sectional area. To color the ferrite grains, samples were color etched using Klemm's I etch (1 g $K_2S_2O_5$ dissolved in 50 ml of stock solution of $Na_2S_2O_3$).

Residual stress measurements were performed by the hole drilling method according to the ASTM E837-13a standard by Hill Engineering (Rancho Cordova, CA, USA). A EA-06-031RE-120 type A strain gauge rosette (Vishay, Malvern, PA, USA)

with three radial gauge elements (**Figure 2.13**) was positioned on the top surface of the samples, and a total of 20 measurements were taken for depth profiling of residual stresses. Maximum and minimum principal residual stresses σ_{max} and σ_{min} were then calculated as:

$$\sigma_{max}, \sigma_{min} = \frac{\sigma_x + \sigma_y}{2} \pm \sqrt{(\frac{\sigma_y - \sigma_x}{2})^2 + \tau_{xy}^2},$$

where σ_x, σ_y – normal residual stresses (MPa), and τ_{xy} – shear residual stress (MPa).

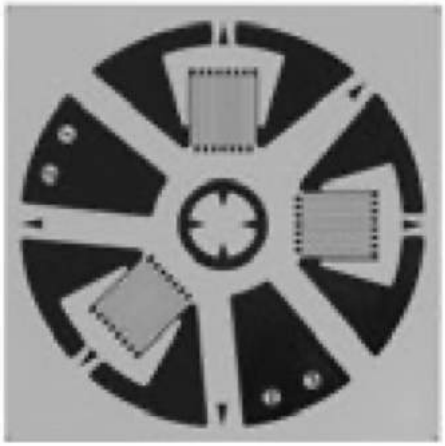

Figure 2.13. A Vishay ES-06-031RE-120 strain gauge for residual stress measurements.

To distinguish the surface and bulk residual stresses, the top 0.5 mm of the samples through which the residual stress measurements were performed were divided into two zones: "surface" (< 90 μm from the top surface) and "bulk" (≥ 90 μm mm from the top surface). The residual stresses within the surface and bulk zones were then averaged, reducing the 20 measurements to 2 data points per sample. Analyses of variance (ANOVA) were then performed on the bulk and surface datasets to determine the of the volumetric energy density (VED, J/mm^3) and alloy composition on the total variation in residual stresses.

The elastic properties (i.e., Poisson's ratio and Young's modulus) were measured through the ultrasound velocity technique with a 38DLP ultrasonic

thickness gauge (Olympus, Shinjuku, Tokyo, Japan) equipped with a 5MHz 0.25 in. diameter longitudinal wave contact transducer and a 5MHz 0.25 in. diameter normal incidence shear wave contact transducer. Sample densities were measured using the Archimedes's principle. Poisson's ratio ν and Young's modulus E were calculated as:

$$\nu = \frac{1 - 2(\frac{V_T}{V_L})^2}{2 - 2(\frac{V_T}{V_L})^2}$$

$$E = \frac{V_L^2 \rho(1+\nu)(1-2\nu)}{1-\nu}$$

where V_T – shear (transverse) velocity (mm/μs), V_L – longitudinal velocity (mm/μs), ρ – sample density (g/cm^3).

Samples for microstructure examination were prepared by following the standard metallographic procedures. First, the samples were embedded in KoductoMet conductive phenolic mounting compound (Buehler, Lake Bluff, IL, USA). Then, the samples were polished with SiC papers (320-1200 grit) using an AutoMet automatic polisher (Buehler, Lake Bluff, IL, USA), followed by polishing with 3 and 1 μm diamond paste with extender on a canvas polishing surface. Finally, the samples were polished using aqueous alumina slurry on a microcloth pad in a GIGA-0900 vibratory polisher (PACE Technologies, Tucson, AZ, USA) for ~6 hours.

Scanning electron microscopy (SEM) and energy-dispersive spectroscopy (EDS) were performed with a Magellan 400 XHR microscope (FEI, Hillsboro, OR, USA). Electron backscatter diffraction (EBSD) and focused ion beam (FIB) TEM sample preparation were performed using a GAIA3 SEM-FIB dualbeam microscope (Tescan, Brno, Czech Republic) equipped with a NordlysMax2 EBSD detector (Oxford Instruments, Abingdon, Oxfordshire, UK) and a Ga ion source.

EBSD maps were post-processed using the open source MTEX Matlab toolbox [40]. Data points with mean angular deviation (MAD) of > 1° were removed, and grain

reconstruction was performed by defining grains as areas of the map completely surrounded by boundaries with a misorientation > 5. The orientation data were denoised and missing data were interpolated using the half-quadratic filter [41]. An approach based on local orientation changes was employed to calculate the density of geometrically necessary dislocations (GNDs) [42].

Scanning transmission electron microscopy (STEM) was performed with a JEM-2800 S/TEM microscope outfitted with dual 100 mm^2 silicon drift detectors (SDD) for EDS.

2.4 Results

2.4.1 Powder characterization

First, we investigated the morphology and composition of the gas atomized Fe and Fe-50Cu powders (**Figure 2.14**). The Fe powder particles were found to exhibit spherical shape (**Figure 2.14, a**), while the Fe-50Cu powder featured more irregularly shaped particles (**Figure 2.14, b**). Powder diffraction patterns collected from the Fe and Fe-50Cu samples confirmed that no extraneous phases were present in the feedstock powders (**Figure 2.14, c**).

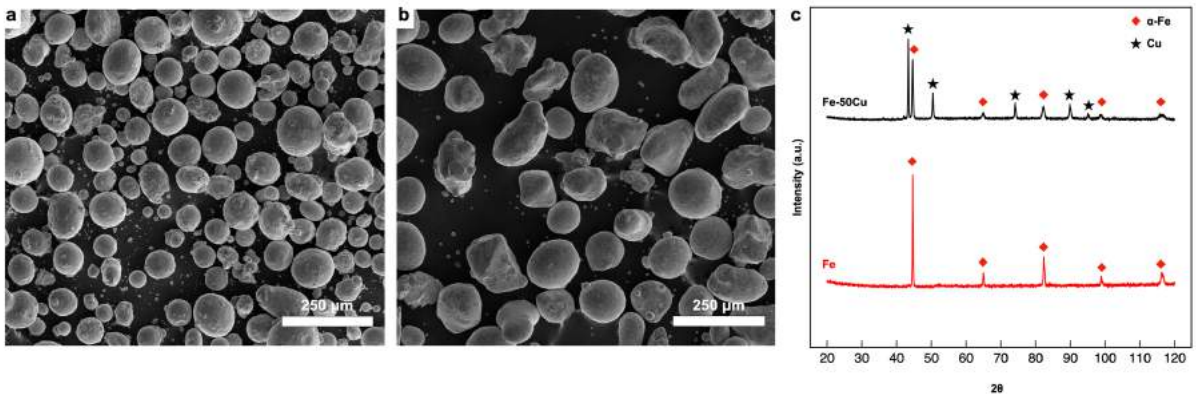

Figure 2.14. Characterization of feedstock powders. a) A scanning electron microscopy (SEM) micrograph of Fe powder particles. b) A SEM micrograph of Fe-50Cu (wt.%) powder particles. c) Powder X-ray diffraction patterns obtained from Fe (red trace) and Fe-50Cu (black trace) powders.

2.4.2 DED process parameters optimization

To determine the optimal processing parameters for LENS® of pure Fe parts, we deposited multiple 10 x 10 x 10 mm cuboid test samples. We used specific energy E (J/mm²) and powder mass density G (g/mm²) as combined parameters guiding the optimization:

$$E = \frac{P}{2vr_l}$$

$$G = \frac{\dot{m}}{2vr_l}$$

where P is the laser power (W), v is the scan speed (mm/s), r_l is the radius of the laser spot and $\dot{m}$ is the feed rate of the powder (g/min).

Figure 2.15 shows that at high E/G ratios, the dilution problem is present, i.e. not enough powder is supplied to successfully build the parts. If the E/G ratio is low, the porosity problem is evident, i.e. the laser power is not high enough to melt all the particles, leading to formation of lack-of-fusion porosity. The feasible processing window is indicated in **Figure 2.15** with a green oval.

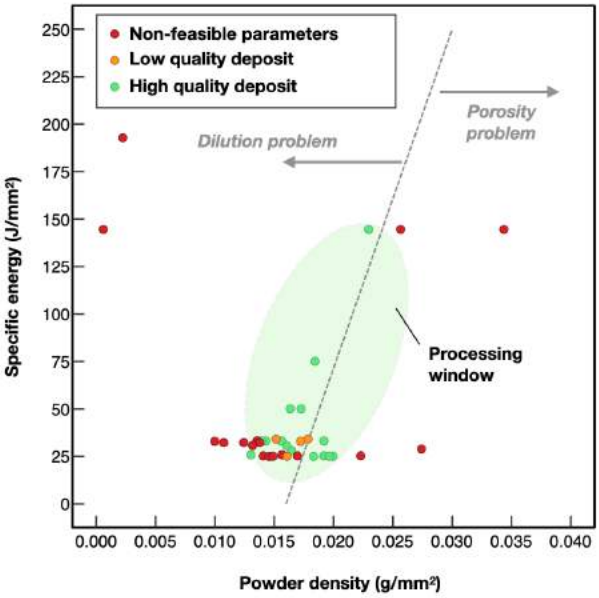

Figure 2.15. Directed energy deposition processing window for pure Fe.

Additionally, the effect of specific energy on the porosity of the parts is illustrated in **Figure 2.16**. Lower specific energy yielded highly-porous samples with both lack-of-fusion and gas porosity present. Higher specific energy produced parts with a decreased amount of lack-of-fusion and gas porosity.

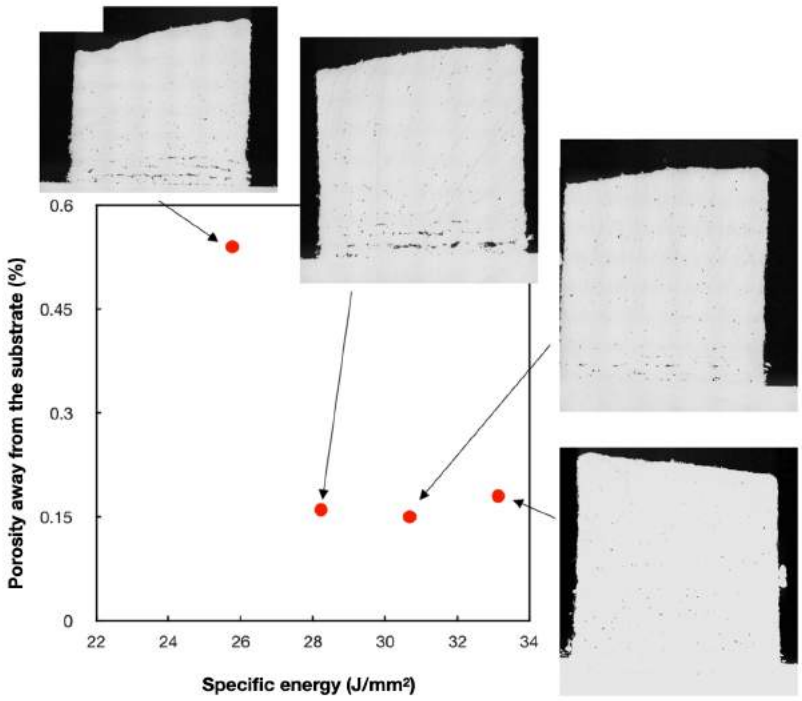

Figure 2.16. Effect of specific energy on porosity of Fe parts printed via directed energy deposition (DED). Higher specific energy used during DED reduces the amount of lack of fusion porosity.

Table 2.2. Directed energy deposition process parameters used in this study.

Sample ID	Material	Laser power (W)	Scan speed (mm/s)	Powder feed rate (g/s)	Specific energy (J/mm²)	VED* (J/mm³)	Powder mass density (g/mm²)
60-62	Fe	467	26.67	0.365	25	100	0.020
63-65	Fe	889	16.93	0.237	75	300	0.020
66-68	Fe	926	10.58	0.170	125	500	0.023
73-75	Fe-50Cu	889	16.93	0.271	75	300	0.023
101-103	Fe-50Cu	400	16.09	0.270	36	140	0.024
104-106	Fe-50Cu	380	6.35	0.245	85	340	0.055
107-109	Fe-50Cu	450	16.93	0.247	38	152	0.021

*VED – volumetric energy density

2.4.3 Elastic properties

The measured Poisson's ratio and Young's modulus for the two additively manufactured materials, Fe and Fe-50Cu, are presented in **Table 2.3**. Poisson's ratio was determined to be 0.28 and 0.33 for Fe and Fe-50Cu, respectively. Young's

modulus was calculated as ~201 GPa for Fe and ~144 GPa for Fe-50Cu. These values are consistent with the literature data (~208 GPa for Fe) and the rule of mixtures, through which the estimated modulus of Fe-50Cu is estimated to be ~168 GPa [151].

Table 2.3. Material elastic constants determined from the ultrasonic velocity measurements.

Material	Shear velocity (mm/μs)	Longitudinal velocity (mm/μs)	Density (g/cm^3)	Poisson's ratio	Young's modulus (GPa)	Shear Modulus (GPa)
Fe	3.193	5.788	7.69	0.28	201	78
Fe-50Cu	2.624	5.231	7.85	0.33	144	54

2.4.4 Microstructure of Fe DED deposits

Optical micrographs of the microstructure of a representative pure Fe LENS® build are shown in **Figure 2.17**. At the bottom of the build, the heat affected zone between the low-carbon steel substrate and the pure Fe build is present. The pure Fe part exhibits grains elongated along the build direction, as is typical for AM. White arrows indicate gas porosity, while no lack of fusion porosity was observed in the builds fabricated using the optimized parameters.

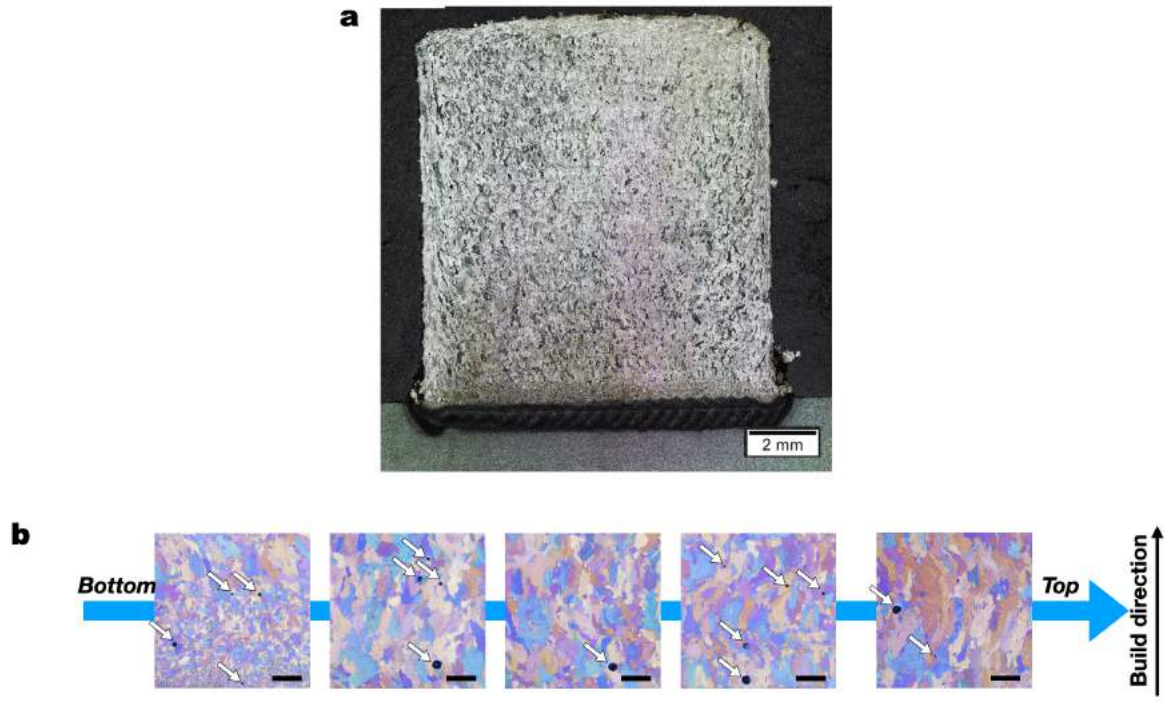

Figure 2.17. Optical micrographs showing the microstructure of a representative pure Fe LENS® build (scale bar 200 µm). a) An optical micrograph of an entire Fe LENS® build. b) Microstructural variations along the build direction. White arrows indicate gas porosity.

Figure 2.18 presents SEM micrographs of a representative Fe sample fabricated at a VED of 100 J/mm^3. Melt pool boundaries are visible from the low magnification micrographs (**Figure 2.18, a**), and no lack of fusion porosity is observed within the sample. In the higher magnification micrographs (**Figure 2.18, b**), a tendency of spherical gas pores of ~230 nm in diameter to migrate to the grain boundaries is evident. The pores then coalesced, promoting hot cracking at the grain boundaries [152]. This effect was not present in the Fe sample fabricated at a VED of 500 J/mm^3 (**Figure 2.19**), where the gas porosity was distributed randomly and did not segregate or coalesce.

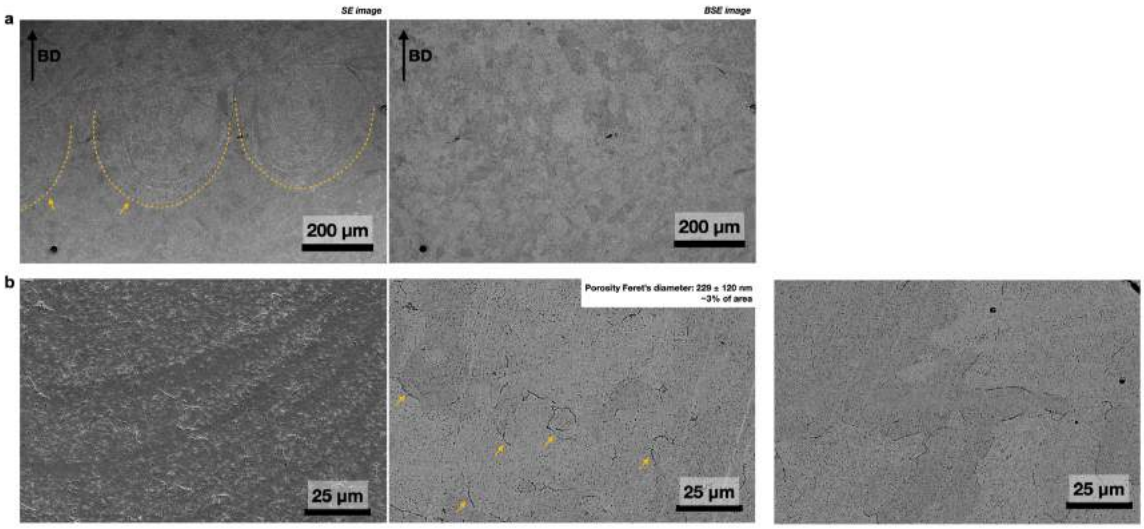

Figure 2.18. Scanning electron microscopy micrographs showing the microstructure of a representative Fe sample fabricated at a VED of 100 J/mm³. a) Melt pool and heat affected zone boundaries are evident in the sample. No lack of fusion pores are observed. b) Gas porosity segregation and hot cracking at the grain boundaries (cracks are indicated with yellow arrows). Gas pores occupy ~3% of the area, with average pore Feret's diameter of ~229 ± 120 nm.

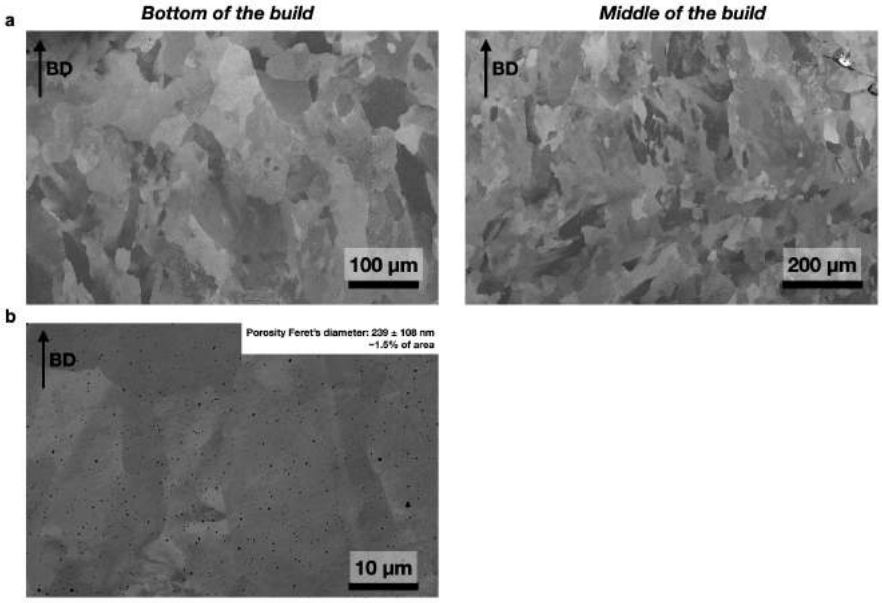

Figure 2.19. Scanning electron microscopy micrographs showing the microstructure of a representative Fe sample fabricated at a VED of 500 J/mm³. a) Large grains elongated along the build direction are evident. b) Gas porosity is randomly distributed within the grains, in contrast to the 100 J/mm³ sample. Gas pores occupy ~1.5% or the area, and have an average Feret's diameter of ~239 ± 108 nm, similar to the 100 J/mm³ sample.

2.4.5 Microstructure of Fe-50Cu DED deposits

SEM micrographs of a representative microstructure of a Fe-50Cu deposit are shown in **Figure 2.20**. In these secondary electron micrographs, the Fe-rich phase appears darker than the Cu-rich phase due to a lower atomic number of Fe as compared to Cu. The Fe-rich phase forms finely-distributed, nearly-spherical particles or elongated dendrites, depending on the position within the melt pool.

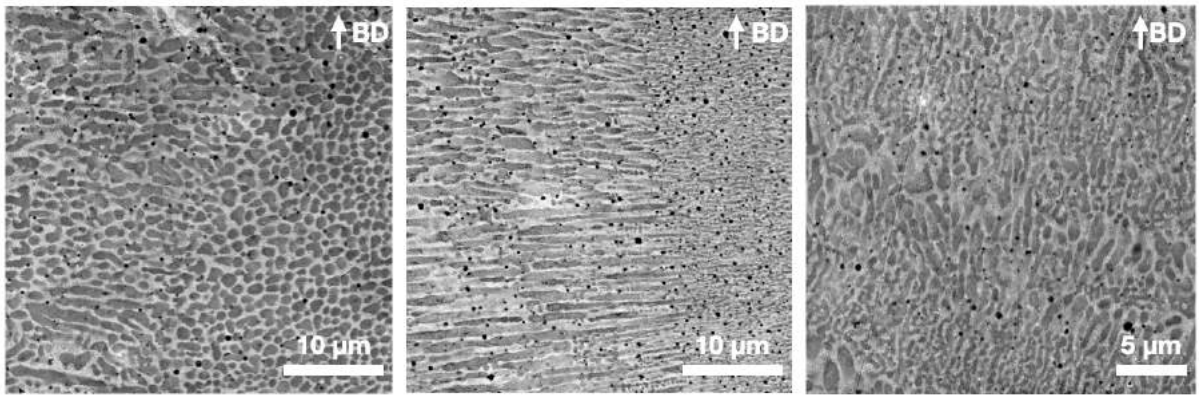

Figure 2.20. Scanning electron microscopy images showing some representative microstructures of a DED-fabricated Fe-50Cu sample. The Fe-rich phase appears darker than the Cu-rich phase. Gas porosity appears as black spherical particles.

EDS analysis revealed that dendrites and spherical particles are Fe-rich, while interdendritic regions are Cu-rich (**Figure 2.21**). After LENS® processing, composition of the Fe-50Cu alloy remained close to that of the pristine powder: 49.1-49.8 wt.% Fe and 50.2-50.9 wt.% Cu (**Table 2.4**). This result indicates that Cu loss during DED processing was minimal, despite its significantly lower melting point (1538 °C and 1085 °C for Fe and Cu, respectively [151]).

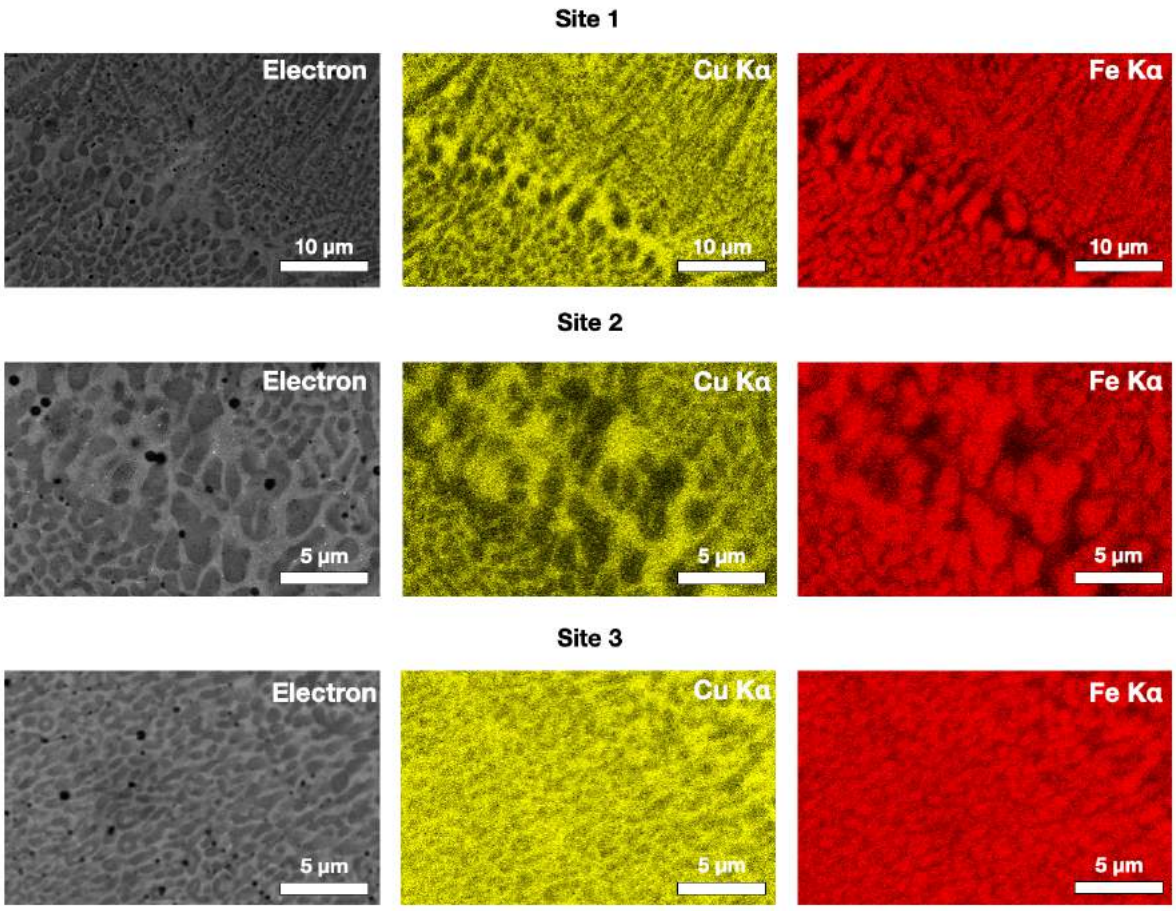

Figure 2.21. Energy dispersive spectroscopy mapping of a representative Fe-50Cu deposit showing the distribution of the Fe-rich and Cu-rich phases.

Table 2.4. Energy-dispersive spectroscopy chemical composition analysis results for three sites shown in Figure 2.21.

Site	Element	Wt. %	At.%
1	Fe	49.8	53.0
	Cu	50.2	47.0
2	Fe	49.3	52.5
	Cu	50.7	47.5
3	Fe	49.1	52.4
	Cu	50.9	47.6

2.4.6 Residual stresses in DED-printed samples

Results of residual stress measurements are presented in **Figure 2.22**. For samples fabricated from pure Fe feedstock powder, higher energy input during

printing yielded residual stresses lower in magnitude and of a more compressive character (**Figure 2.22, a**). For Fe-50Cu samples, surface compressive stresses of ~ -190 MPa were observed (**Figure 2.22, b**). High variability was observed between the replicate samples fabricated with the same process parameters.

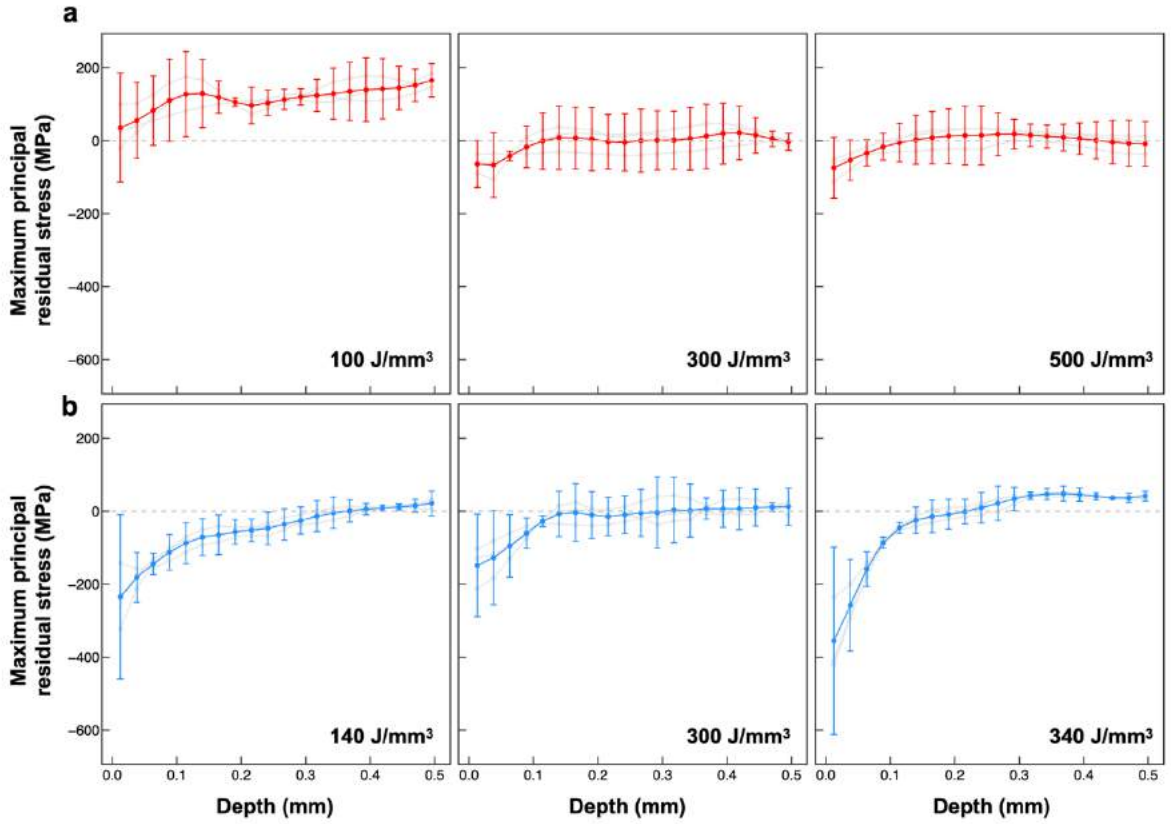

Figure 2.22. Residual stress measurement results. Data for individual samples are shown in grey traces. Red and blue traces show mean values of residual stresses calculated for three replicate samples. Error bars represent 95% confidence intervals on the mean. a) Maximum principal residual stress in Fe samples fabricated at three VEDs: 100 J/mm³ (left), 300 J/mm³ (center) and 500 J/mm³ (right). b) Maximum principal residual stress in Fe-50Cu samples fabricated at three VEDs: 140 J/mm³ (left), 300 J/mm³ (center), and 340 J/mm³ (right).

The mean values of maximum principal residual stress in the bulk and surface zones of the Fe and Fe-50Cu samples as a function of VED are plotted in **Figure 2.23**. For pure Fe samples, higher VED used during DED caused lower stress both in the bulk and on the surface of the samples. For Fe-50Cu, higher VED caused higher bulk

stresses and did not affect the surface stresses. This result suggests that the relationship between the residual stress and process parameters is material-specific, corroborating the findings of Denlinger et al. obtained for Ti-6Al-4V and Inconel 625 [124] and validating out initial hypothesis.

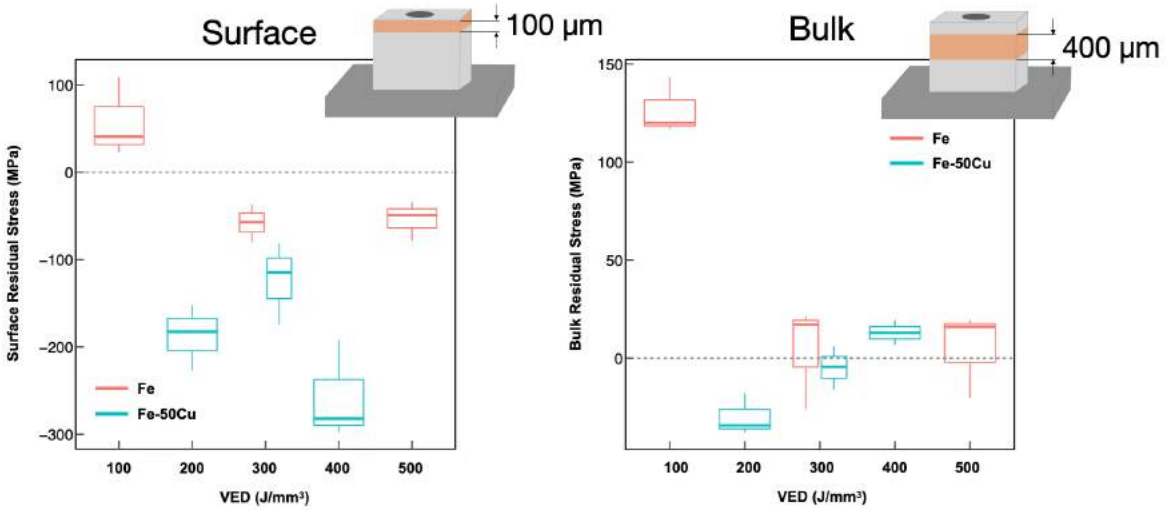

Figure 2.23. *Maximum principal residual stress in the bulk (right) and surface (left) zones of the Fe and Fe-50Cu samples as a function of volumetric energy density (VED).*

The ANOVA results are presented in **Table 2.5**. For the surface residual stresses, there was a statistically significant difference between the Fe and Fe-50Cu materials as determined by one-way ANOVA ($F(1,5) = 80.181$, $p = 1.16 \times 10^{-6}$). Moreover, the difference between the samples fabricated with different VEDs was also statistically significant ($F(1,5) = 7.977$, $p = 0.00223$). Based on the ANOVA results, ~64.6% of the variation in surface principal residual stresses was attributed to the alloy composition, ~25.7% to the VED, and ~9.7% of the variation was not explained by the statistical model and was attributed to random error. For the bulk residual stresses, both VED and material factors had a statistically significant effect on the bulk principal residual stresses ($p = 3.93 \times 10^{-6}$ and $p = 2.14 \times 10^{-5}$, respectively). Variation partitioning based on the ANOVA results suggested that ~25.7% of the variation in

bulk principal residual stress was attributed to the alloy composition, ~67.4% - to the VED, and ~6.9% - to the random error. The statistical analysis results confirmed our initial hypothesis that the residual stresses in additively manufactured metal parts can be manipulated by adjusting the alloy composition. Moreover, adjusting the process parameters also had a statistically significant effect on both bulk and surface residual stresses.

Table 2.5. Analysis of variance results for bulk and surface residual stresses.

Source	DF	SS	MS	F-value	p
Surface residual stress					
Material	1	132199	132199	80.181	$1.16 \times 10^{-6***}$
VED	5	52607	13152	7.977	0.00223^{**}
Residuals (error)	14	19785	1649		
Bulk residual stress					
Material	1	12470	12470	45.15	$2.14 \times 10^{-5***}$
VED	5	32673	8168	29.57	$3.93 \times 10^{-6***}$
Residuals (error)	14	3314	276		

2.4.7 Plastic deformation in DED-printed Fe-50Cu

Phase-specific plastic deformation within the Cu-rich and the Fe-rich phases of DED-fabricated Fe-50Cu alloy was examined directly with TEM. A TEM sample was extracted with a focused ion beam lift out procedure from within the top 500 μm of the LENS® deposit (**Figure 2.24, a**). Examination of the sample using STEM revealed a high density of dislocations within the Cu-rich phase (**Figure 2.24, b-c**), and dislocation-free Fe-rich dendrites and particles. This was further confirmed with

STEM-EDS, which demonstrated conclusively that a high dislocation density within the Cu-rich phase (**Figure 2.24, d**).

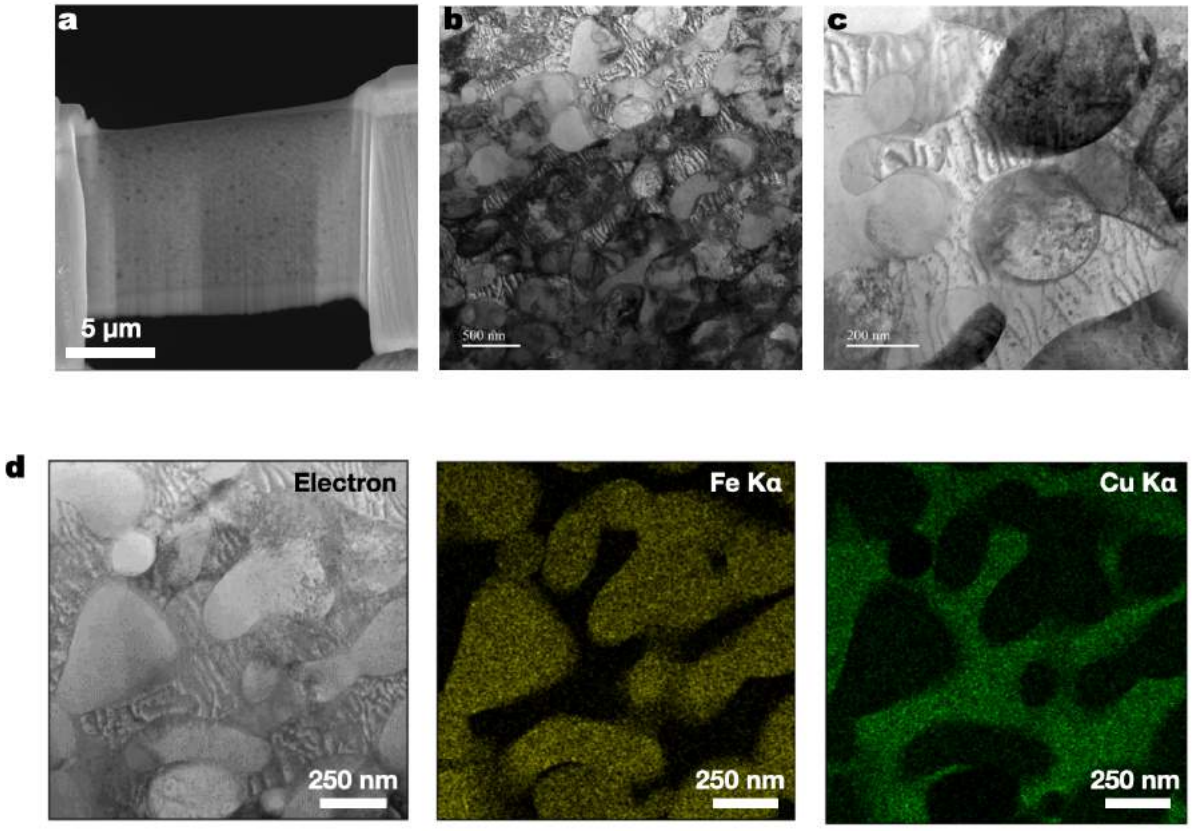

Figure 2.24. Scanning transmission electron microscopy (STEM) imaging of a DED-fabricated Fe-50Cu sample. a) An SEM micrograph of the TEM sample. b-c) Bright-field STEM micrographs showing high dislocation density within the Cu-rich phase. D) STEM-EDS mapping confirming that dislocations are confined to the Cu-rich phase.

To quantify the GND density within the two phases, we performed EBSD mapping of a Fe-50Cu sample (**Figure 2.25**). A phase map showing the distribution of the Fe-rich and Cu-rich phases is presented in **Figure 2.25, a**. Inverse pole figure (IPF) map of the Fe-rich phase (**Figure 2.25, b**) demonstrates that each of the Fe-rich particles and dendrites is a separate grain. In contrast, IPF map of the Cu-rich phase (**Figure 2.25, c**) suggests gradual orientation changes within the Cu-rich phase and formation of relatively large, micro-scale grains. Phase-specific analysis of the

GND density revealed that GND densities were lognormally distributed within both phases (**Figure 2.25, d**). The mean GND density was calculated to be 471 ± 95 μm^{-2} in the Fe-rich phase and 684 ± 80 μm^{-2} within the Cu-rich phase, and a t-test performed on the difference in means confirmed statistical significance of the difference in GND densities between the two phases (p = 0.0008).

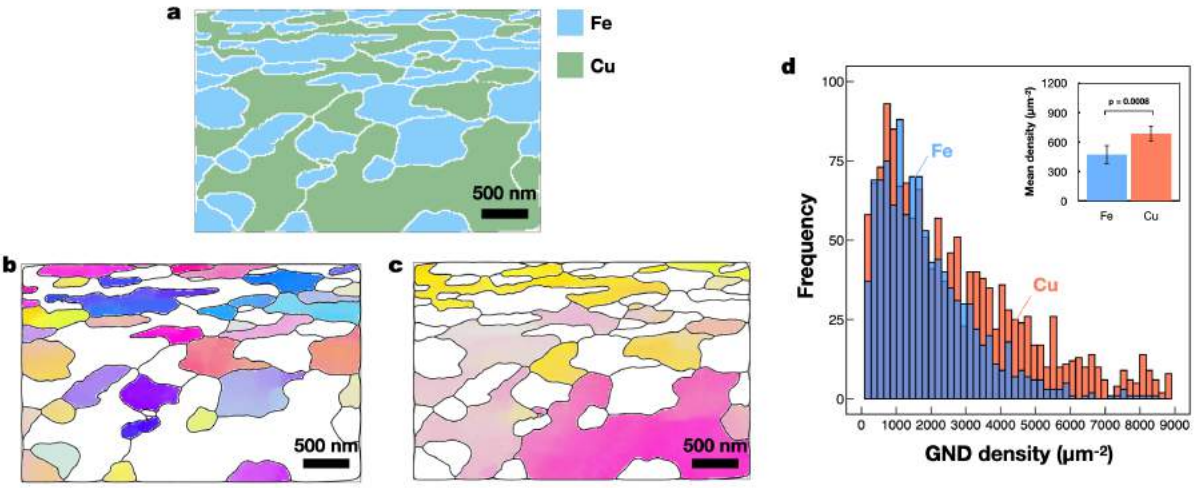

Figure 2.25. Electron backscatter diffraction (EBSD) mapping of a DED-fabricated Fe-50Cu sample. a) Phase map showing the distribution of the Fe-rich and Cu-rich phases. b) Inverse pole figure (IPF) map of the Fe-rich phase. c) IPF of the Cu-rich phase. d) Histogram of the geometrically necessary dislocation (GND) density for the two phase, with mean GND densities plotted in the inset. Error bars indicate 95% confidence intervals.

2.5 Discussion

DED-printed parts of pure Fe tended to exhibit large grains elongated along the build direction (**Figure 2.17, Figure 2.18, Figure 2.19**) , which is a microstructure typical for additively-manufactured parts. Fe-50Cu parts, in turn, showed a fine dispersion of the Fe-rich phase within the Cu-rich matrix and small, randomly-oriented grains (**Figure 2.21, Figure 2.25**). Interestingly, such finely-dispersed microstructures cannot be readily achieved in immiscible alloys in general and Fe-Cu binary alloys specifically using conventional manufacturing methods, such as casting [153].

Hole drilling residual stress measurements demonstrated that both the magnitude and the character (i.e., tensile/compressive) of the residual stress can be manipulated by engineering solid-state transformations in the alloy. By separating the stresses into surface and bulk components and applying ANOVA to the resulting data, we were able to demonstrate that surface residual stresses are controlled by the alloy composition. For surface residual stress, ~65% of the total variation was attributed to the alloy composition, ~25% – to DED process parameters summarized in VED, and ~10% to other factors and random error. In contrast, for bulk residual stress, the variation was dominated by DED process parameters: ~67% of the variation was attributed to VED, ~26% - to alloy composition, and 7% - to random error.

It is important to note that the present analysis of the residual stresses is limited by the hole-drilling technique, in which only in-plane stresses can be measured. No information about the build direction stresses can be acquired with a strain gage placed on the top surface of the sample. Future studies will involve additional strain gages placed on side surface of the sample or other residual stress measurement approaches that are capable of measuring stresses in x, y and z direction, such as neutron diffraction.

Overall, residual stresses were more compressive in the Fe-50Cu samples. We can speculate that this effect can be attributed to the phase transformations occurring during solidification of the Fe-50Cu binary alloy. According to the Fe-Cu binary phase diagram, the FCC γ-Fe phase solidifies first, followed by solidification of the ε-Cu phase and a solid-state phase transformation of FCC γ-Fe to BCC α-Fe (**Figure 2.10**). Upon further cooling, the system stabilizes as a two-phase solid with the Cu-rich phase as a matrix.

A schematic representation of the phase and microstructure evolution during solidification of Fe-50Cu binary alloy is shown in **Figure 2.26**. Solid-state phase transformation of FCC γ-Fe to BCC α-Fe is accompanied by a ~1% volume increase of the Fe-rich particles/dendrites due to BCC lattice accommodating fewer atoms in a unit cell than the FCC lattice.

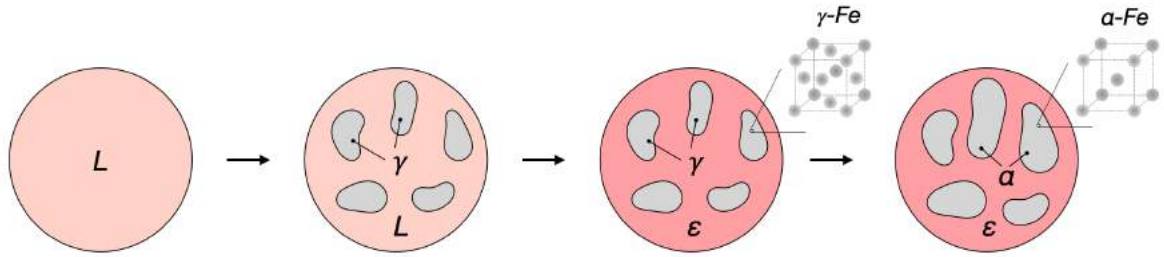

Figure 2.26. A schematic representation of phase evolution during solidification of the Fe-50Cu alloy.

We can now discuss the phase and microstructure evolution of Fe-50Cu in terms of the residual stresses within the system upon cooling **(Figure 2.27**). Let us first focus on pure Fe. . In the liquid state, residual stresses within this system are equal to zero. Upon cooling, the BCC δ-Fe phase solidifies first. Cooling of δ-Fe results in thermal contraction of the sample that is constrained by the substrate, which leads to development of hydrostatic tensile residual stresses. At ~1394 °C, the BCC δ-Fe undergoes a solid-state phase transformation to FCC γ-Fe accompanied by ~3% decrease in volume. The decrease in volume is associated with a rapid increase in tensile residual stress. After the phase transformation is complete, the system once again undergoes only thermal contraction, which continues to increase residual stresses until the system reaches ~910 °C. At this temperature, FCC γ-Fe is transformed to BCC α-Fe, causing a ~1% increase in volume, which slightly decreases the residual stress. Finally, upon further cooling, the residual stresses increase due to thermal contraction of α-Fe.

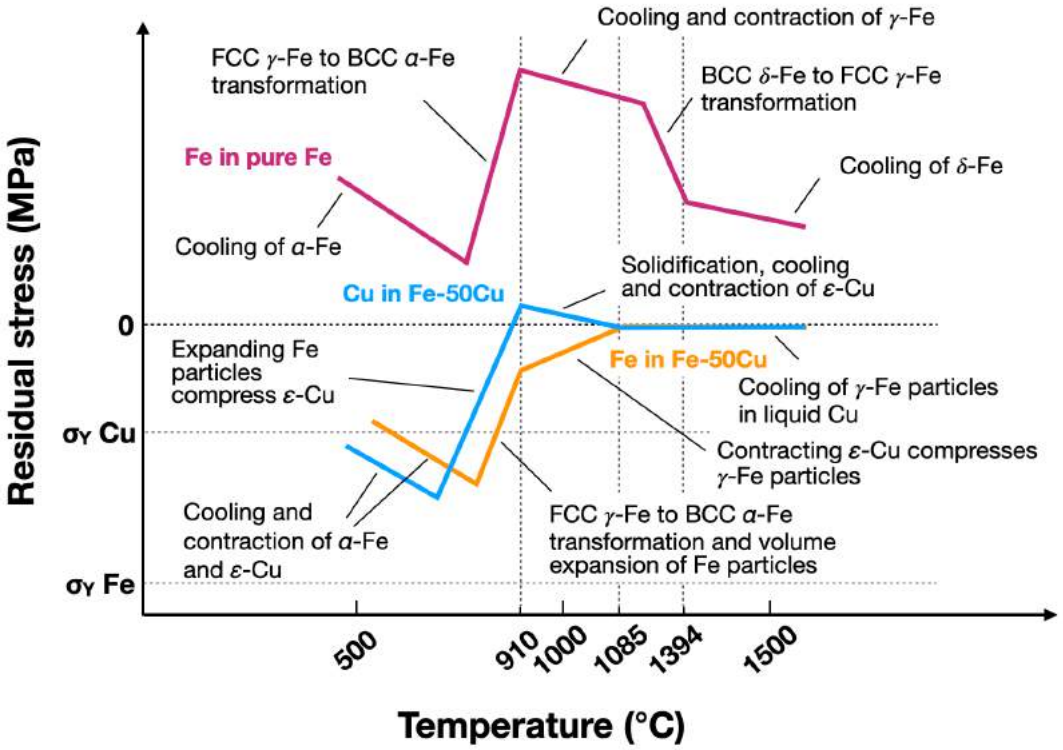

Figure 2.27. A schematic of the evolution of residual stress during solidification and cooling of pure Fe and the Fe-50Cu alloy.

The evolution of residual stresses in the Fe-50Cu alloy follows a different path. First, we can consider the Fe-rich phase. The γ-Fe particles and dendrites solidified within the liquid Cu-rich phase will be virtually stress-free. Upon solidification of ε-Cu that starts at ~1085 °C, thermal contraction of the Cu-rich matrix induces compressive residual stresses within the γ-Fe particles and dendrites. At ~910 °C, solid state phase transformation of γ-Fe to α-Fe (accompanied by volume expansion of the Fe particles) leads to an increase in compressive residual stresses. Further cooling of the system leads to thermal contraction of the particles and, consequently, to a decrease in compressive residual stresses. The Cu-rich phase follows a similar path. Liquid Cu-rich phase remains stress-free until ~1085 °C, at which point solidification, cooling and resulting thermal contraction of Cu results in hydrostatic tensile residual stresses within the matrix. At

~910 °C, expansion of the Fe-rich particles caused by the solid-state transformation of Fe introduces compressive residual stresses. Finally, cooling of the system results in contraction of both α-Fe and ε-Cu that causes a decrease in the magnitude of compressive stress within the Cu-rich phase.

If we contrast the residual stress evolution within the pure Fe to that of Fe-50Cu, we can clearly see that, upon cooling, residual stresses in pure Fe are likely to remain tensile. However, both Cu-rich and Fe-rich phases within Fe-50Cu are likely to exhibit compressive residual stresses. It is important to note that yield strength of Cu is significantly lower than that of Fe (69 MPa [154] versus 140 MPa [155], respectively), which explains our observations of high dislocation density within the Cu-rich phase (**Figure 2.24, Figure 2.25**).

While we can attribute the observed differences in residual stress state to the solid-state phase transformations within the Fe and Fe-50Cu samples, it is important to highlight that DED is a non-equilibrium, high cooling rate processing technique, in which phase transformations might deviate from those predicted by the equilibrium phase diagram. An *in situ* synchrotron diffraction study of Fe-50Cu DED could be used to acquire real-time information on the phases and strains present within the material.

2.6 Conclusions

In this work, we investigated the relationship between alloy composition and residual stresses formed during DED processing in a Fe-Cu binary alloy. To this end, we studied DED-fabricated components of i) pure Fe, and ii) Fe-50Cu (wt.%) binary alloy. We measured the residual stresses within as-printed samples using the hole drilling approach. Through statistical analysis, we demonstrated that surface residual stresses were especially susceptible to alloy composition. TEM and EBSD

characterization of the Fe-50Cu parts revealed a high density of dislocations within the Cu-rich phase, suggesting that Cu-rich phase yielded to accommodate the residual stresses introduced during DED. This work demonstrates that phase transformations can be successfully engineered to produce a desired residual stress state in the as-printed components.

CHAPTER 3 HIGH ENTROPY SILICIDES: CALPHAD-BASED PREDICTION AND THIN FILM FABRICATION

3.1 Introduction

The field of high entropy materials design represents a departure from conventional materials design by enabling a vast and mostly unexplored compositional space. The high entropy design concept was first introduced in high entropy alloys (HEAs), alternatively called multi-principal element alloys or complex concentrated alloys [156,157]. HEAs are generally comprised of five or more principal elements in near equiatomic compositions. Some HEA systems achieve a single solid solution phase with a random distribution of the constituents on a crystalline lattice, which leads to interesting properties [158]. Conventional engineering alloy design is traditionally based on a single principal element, which confines the available compositional space to the corners of the phase diagram. In contrast, in HEAs the central regions of the phase diagrams are investigated, unlocking an immense and previously unexplored compositional space (**Figure 3.1**).

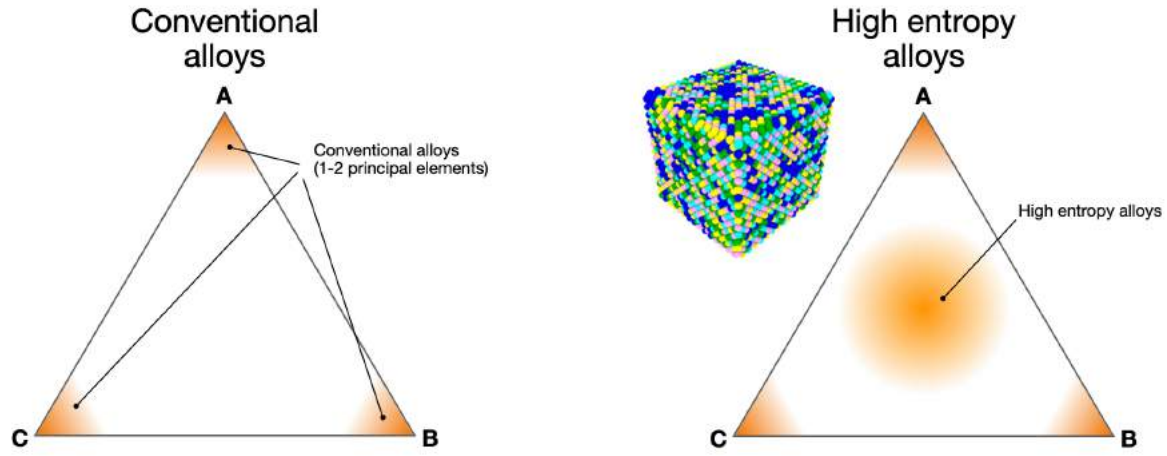

Figure 3.1. Schematic ternary phase diagrams illustrating the differences between conventional alloys and high entropy alloys (HEAs).

The high entropy materials design concept has also been applied to other materials systems, including high entropy oxides [159], high entropy borides [160], and high entropy carbides [161], where the high configurational entropy stabilizes structures and compositions with unusual properties unattainable by the constituent materials [162]. Recently, a new class of high entropy materials – high entropy silicides (HES) – has been demonstrated [163,164]. Development of HES materials is particularly exciting due to their potential applications in microelectronics, where use of silicides is common. For example, silicides are used as insulation in metal-oxide-semiconductor field-effect-transistors (MOSFETs) at the gate, source, and drain terminals [165]. In addition, silicides tend to possess a unique combination of metal-like thermal and electrical conductivity with a ceramic-like elastic modulus and melting temperature (**Figure 3.2, Table 3.1**).

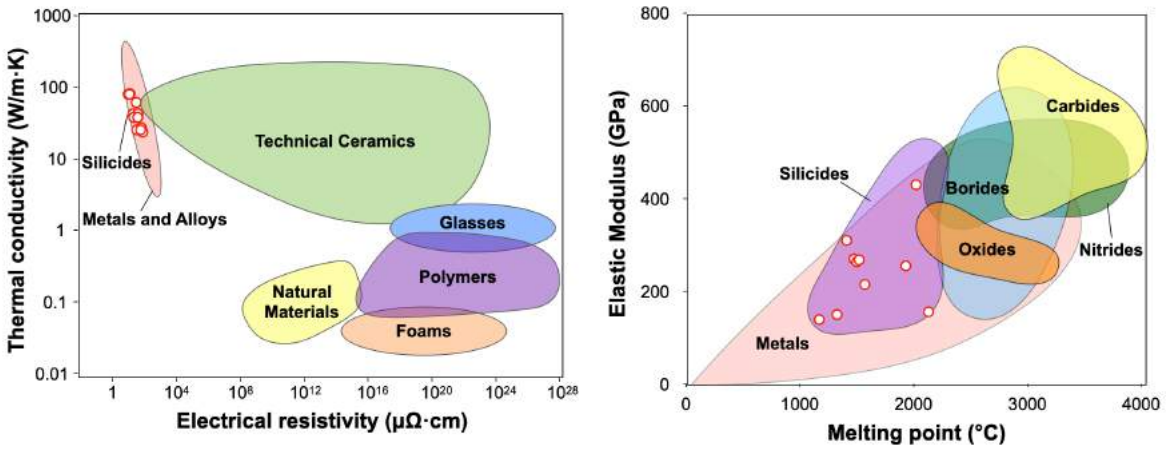

Figure 3.2. Properties of metal silicides (data from [166]*)*

To date, only two HES compositions – $(MoNbTaTiW)Si_2$ [164] and $(MoNbTaCrW)Si_2$ [163] – have been reported. Both materials were synthesized in bulk form via mechanical alloying followed by spark plasma sintering (SPS). It is important to note that neither $(MoNbTaTiW)Si_2$ nor $(MoNbTaCrW)Si_2$ were single phase, as oxides [164] or intermetallics [163] were also present, either due to processing or due

to secondary phases being thermodynamically stable. Thus, it is essential to develop a deeper understanding of phase formation and evolution in our efforts to pursue single-phase HES materials. Additionally, previous work on HES materials has only considered bulk samples, and an investigation into the viability of thin film HES materials is required to expand these materials into integrated circuit and device applications.

The primary challenge in probing the extensive compositional space allowed by high entropy stabilization is effective screening and validation of candidate compositions. Computational thermodynamics techniques, such as the CALculation of PHAse Diagrams (CALPHAD) approach, can be used to predict the phase stability of a given composition and reveal promising candidate compositions. Advancements in the underlying thermodynamic databases used with the CALPHAD approach have made prediction of the phase formation in multiple HEA materials more reliable [167–169], and have enabled us to extend the CALPHAD approach directly to the development of complex HES compositions with targeted phase stability.

In this study, we employ the CALPHAD approach to identify two single-phase HES materials: the ternary $(CrMoTa)Si_2$ and quinary $(CrMoTaVNb)Si_2$. We then experimentally synthesize these silicide compositions in thin film form by electron beam evaporation of the metal constituents onto a Si substrate, followed by a heat treatment to induce a solid-state reaction. Finally, we use grazing incidence X-ray diffraction (GIXRD) depth profiling and scanning electron microscopy (SEM) to evaluate the phase composition and microstructure of the ternary $(CrMoTa)Si_2$ and quinary $(CrMoTaVNb)Si_2$ HES thin films. Both $(CrMoTa)Si_2$ and $(CrMoTaVNb)Si_2$ exhibit a single-phase state with a C40 hexagonal crystal structure, which is consistent with our CALPHAD predictions.

Table 3.1. Binary metal silicides with hexagonal crystal structure.

Material	Crystal System	Space Group	Prototype	Lattice Constants (Å)	Melting Point (°C)	Electrical Classification	RT Resistivity (μΩ·cm)	RT Thermal Conductivity (W/m·K)	Applications
$CrSi_2$	Hexagonal	$P6_222$	$CrSi_2$	a = 4.42758(7) c = 6.36805(11)	1460-1490	Semiconductor (E_{BG} = 0.35 eV)	0.9 (bulk) 120-900 (thin film)	10.6	Thermoelectrics
$MoSi_2$	Tetragonal (α-$MoSi_2$)	I4/mmm	$MoSi_2$	a = 3.200 c = 7.850	2020±20	Semimetal	57-157 (thin film)	66.2	Electrical contacts, electrical heating elements, high temperature structural
	Hexagonal (β-$MoSi_2$, metastable)	$C6_22$	$CrSi_2$	a = 4.596 c = 6.550		Semiconductor (E_{BG} = 0.07 eV)	411 (thin film)		
$TaSi_2$	Hexagonal	$P6_222$	$CrSi_2$	a = 4.78351(7) c = 6.56980(16)	2040-2300	Metal (superconductor, T_c = 0.353 K)	20.2-40.1 (single crystal) 50-281 (thin film)	21.9	Schottky barriers, ohmic contacts, interconnects in ICs
VSi_2	Hexagonal	$P6_222$	$CrSi_2$	a = 4.57230(16) c = 6.3730(4)	1677-1750	Metal	34.13-59.64 (s.c.) 60-85 (thin film)	11.9	High temperature coatings, interconnects in ICs, gate contacts
$NbSi_2$	Hexagonal	$P6_422$	$CrSi_2$	a = 4.797 c = 6.592	1930-1940	Metal (superconductor, T_c = 0.130 K)	22.01-39.15 (s.c.) 50-200 (thin film)	19.1	High temperature structural

3.2 Materials and methods

The CALPHAD approach was employed to identify candidate silicide compositions that are predicted to form a single phase with a C40 hexagonal crystal structure. ThermoCalc Software equipped with the TCHEA3 HEA thermodynamic database was used for the CALPHAD calculations. The TCHEA3 database produced by ThermoCalc contains the necessary models for silicide structures and constituent elements to assess the phase stability in refractory metal silicide systems [170].

The HES thin films were fabricated via a two-step process (Figure 1). First, metal layers (Cr, Mo and Ta for (CrMoTa)Si_2; Ta, V, Nb, Cr, and Mo for (CrMoTaVNb)Si_2) were sequentially deposited onto a Si substrate **(Figure 3.3, a)**. The thicknesses of the individual metal layers (Table S1) were selected to obtain the desired silicide composition after full reaction with Si. The as-deposited multilayer thin films were then heat treated to facilitate the interdiffusion of the metals and Si and solid-state transformation to a single-phase silicide material **(Figure 3.3, b)**.

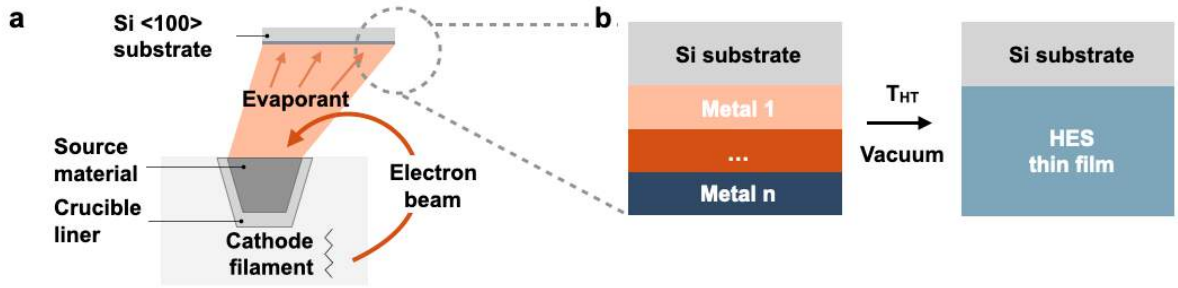

Figure 3.3. Fabrication of thin film high entropy silicides. a) A schematic of the electron beam evaporation process used to fabricate the multilayer thin films. b) Following the deposition, multilayer thin films were heat treated at temperature T_{HT} in a vacuum furnace to facilitate a solid-state transformation to a single-phase silicide material.

V, Nb, Cr, Ta and Mo pellets with >99.7% purity (Kurt J. Lesker Company, Jefferson Hills, PA, USA) were used for electron beam evaporation. Thin films were deposited in an electron beam evaporator (EvoVac Glovebox, Angstrom Engineering,

Kitchener, ON, Canada) with the pressure maintained at <$2.9 \cdot 10^{-7}$ Torr during the deposition. The evaporation parameters, including power and deposition rate for each layer, are summarized in **Table 3.2**. The deposition rates were measured with a quartz crystal monitor (QCM). Thin films were deposited onto undoped Si <100> wafers (University Wafer, South Boston, MA, USA). Heat treatment was performed using a vacuum furnace (M60, Centorr Vacuum Industries, Nashua, NH, USA) under a pressure of <$1x10^{-5}$ Torr. During heat treatment, samples were placed inside a graphite crucible and heated to 800-900 °C for 30-60 min with a heating rate of 10 °C/min. The furnace was turned off at the end of the heat treatment and allowed to cool naturally.

Table 3.2. Electron beam evaporation parameters.

Material	Layer No.	Target layer thickness (nm)	Crucible liner material	Ratio	QCM* deposition rate (Å/s)	Power (%)
$(CrMoTa)Si_2$						
Cr	1	4.00	Graphite	1.15	0.50	1.7
Mo	2	5.21	Graphite	1.23	0.26	23.0
Ta	3	6.00	Graphite	1.50	0.51	19.8
$(CrMoTaVNb)Si_2$						
Ta	1	7.19	Graphite	1.50	0.15	20.0
V	2	5.63	Tungsten	1.13	0.49	2.8
Nb	3	7.19	Fabmate	1.42	0.30	25.3
Cr	4	4.80	Graphite	1.15	0.50	2.2
Mo	5	6.24	Graphite	1.23	0.60	10.0

GIXRD diffraction patterns were collected with a diffractometer equipped with a 2.2 kW Cu-Kα X-ray source with λ = 1.54187 Å (Smartlab, Rigaku, Tokyo, Japan). The diffractometer was configured in parallel beam geometry and ω-2θ mode, with the incidence angle ω set to 0.2°, 0.4°, 0.55°, 0.6°, 0.8° and 1.2° to facilitate depth profiling. The patterns were collected in the 2θ range of 20-50° with 0.05° step and at a scan speed of 0.65 °/s. PDF cards No. 00-004-0809, 00-006-0694, 00-004-0788, 00-034-0370, 00-022-1058 were used to identify the (110) peak position for Mo, Cr, Ta, Nb and V, respectively. Lattice parameters for the (CrMoTa)Si_2 and (CrMoTaVNb)Si_2 thin film samples were determined by performing full-pattern Rietveld refinement using the GSAS-II software package [171]. Patterns collected at the incidence angle of 0.55° were used for the refinement.

Secondary electron micrographs were obtained with a scanning electron microscope (SEM, Magellan 400, FEI, Hillsboro, OR, USA) equipped with a through-the-lens (TLD) detector operated in immersion mode. Cross-sectional imaging was performed by fracturing the samples, and thin film thicknesses were measured from the fracture cross-section micrographs using ImageJ [39]. Average grain sizes were measured from the top-down SEM micrographs according to the Abrams three-circle procedure described in ASTM E112-13 [43]. Energy-dispersive X-ray spectroscopy (EDS) was performed with X-Max silicon drift detector (Oxford Instruments, Abingdon, UK) at an accelerating voltage of 5 kV and a beam current of 0.2 nA.

3.3 Results and Discussion

First, we pre-screened metals that form silicides with the target C40 ($CrSi_2$-type) hexagonal crystal structure. We found that Cr, Ta, V, Mo and Nb form MSi_2 silicides with C40 hexagonal crystal structure (**Table 3.1**) [166,172]. Then, we used the CALPHAD approach to identify candidate single-phase silicide compositions.

Equilibrium step diagrams, which show the relative amount of each stable phase calculated as a function of temperature, were used to assess a composition's propensity to form a single-phase state. By comparing the equilibrium step diagrams for a variety of silicide compositions containing three or more refractory metal elements in equiatomic ratios, i.e., (M_1, M_2, M_3, … , M_x)Si_2, we identified two candidate single-phase HES compositions: the ternary (CrMoTa)Si_2 and quinary (CrMoTaVNb)Si_2. Both the ternary (CrMoTa)Si_2 **(Figure 3.4, a)** and the quinary (CrMoTaVNb)Si_2 **(Figure 3.4, b)** were predicted to exhibit a single phase with a C40 hexagonal crystal structure. Stability of the high entropy C40 phase predicted by CALPHAD is in agreement with previous studies on phase stability in $MoSi_2$-based ternary silicides, where the presence of the C40 phase was shown to be ubiquitous [173].

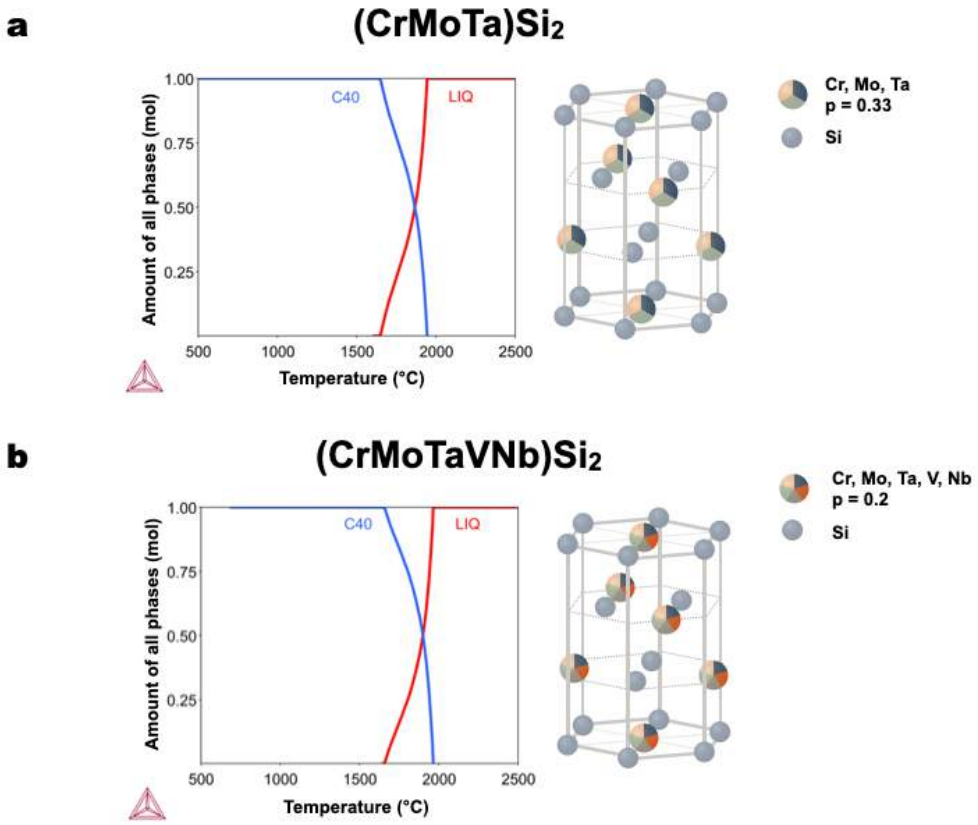

Figure 3.4. CALPHAD prediction of the two candidate high entropy silicides (HES). a) Calculated equilibrium step diagram of the ternary (CrMoTa)Si2 HES, showing the equilibrium phases over a range of temperatures (left). A schematic unit cell of ternary (CrMoTa)Si2 HES with a C40 hexagonal crystal structure, showing equal probability of site occupation by Cr, Mo and Ta atoms on the metal cation sublattice

as predicted by CALPHAD (right). b) Calculated equilibrium step diagram for the quinary (CrMoTaVNb)Si2 HES, showing the equilibrium phases over a range of temperatures (left). A schematic unit cell of the quinary (CrMoTaVNb)Si2 HES with a C40 hexagonal crystal structure, showing equal probability of site occupation by Cr, Mo, Ta, V and Nb atoms on the metal sublattice as predicted by CALPHAD (right).

Representative equilibrium phase diagrams for silicides that are predicted to form multiple phases are shown in **Figure 3.5**. In both (CrMoW)Si_2 and (TiMoTaVNb)Si_2, one element has been substituted in comparison with (CrMoTa)Si_2 and (CrMoTaVNb)Si_2, which resulted in predicted formation of $C11_b$ and C14 Laves phases, respectively.

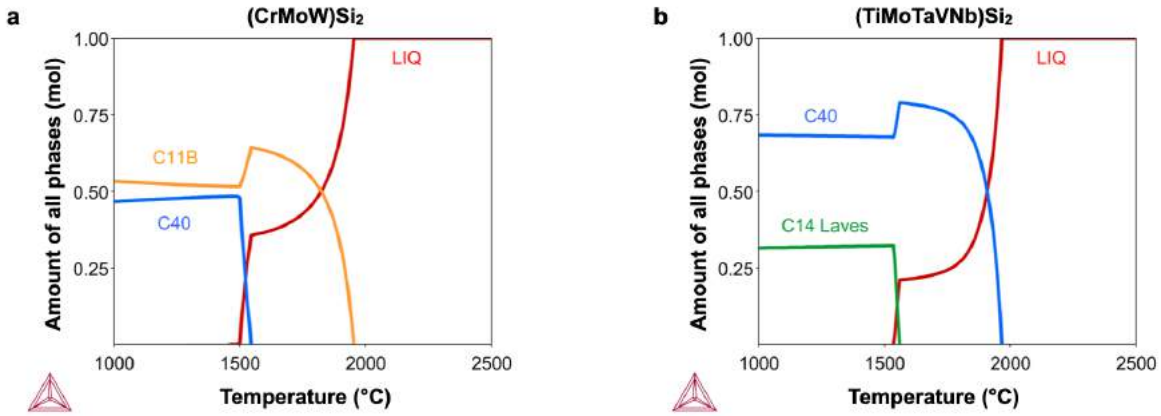

Figure 3.5. Calculated equilibrium step diagrams of (a) (CrMoW)Si_2 and (b) (TiMoTaVNb)Si_2 materials. Both materials exhibit secondary phase formation.

Moreover, we demonstrated the (CrMoTa)Si_2 and (CrMoTaVNb)Si_2 compositions are unique in their single C40 phase formation as compared to the previously reported HES materials. **Figure 3.6** presents the equilibrium step diagrams for (MoNbTaTiW)Si_2 [164], (MoNbTaWZr)Si_2 [164] and (MoNbTaCrW)Si_2 [163], which were predicted to exhibit multiple phases at equilibrium, confirming previously reported observations of secondary phases. In (MoNbTaWZr)Si_2, presence of Ta-, Nb- and Zr-rich intermetallics was demonstrated by XRD and EDS mapping

[164] and further confirmed by our CALPHAD predictions (**Figure 3.6, c-e**). Taken together, our CALPHAD predictions and previous studies suggest that Cr, Mo, Ta, V and Nb are unique in their ability to form a single phase with a C40 hexagonal crystal structure. However, additional single-phase high entropy silicides with other crystal structures (e.g., A15 cubic) might be possible.

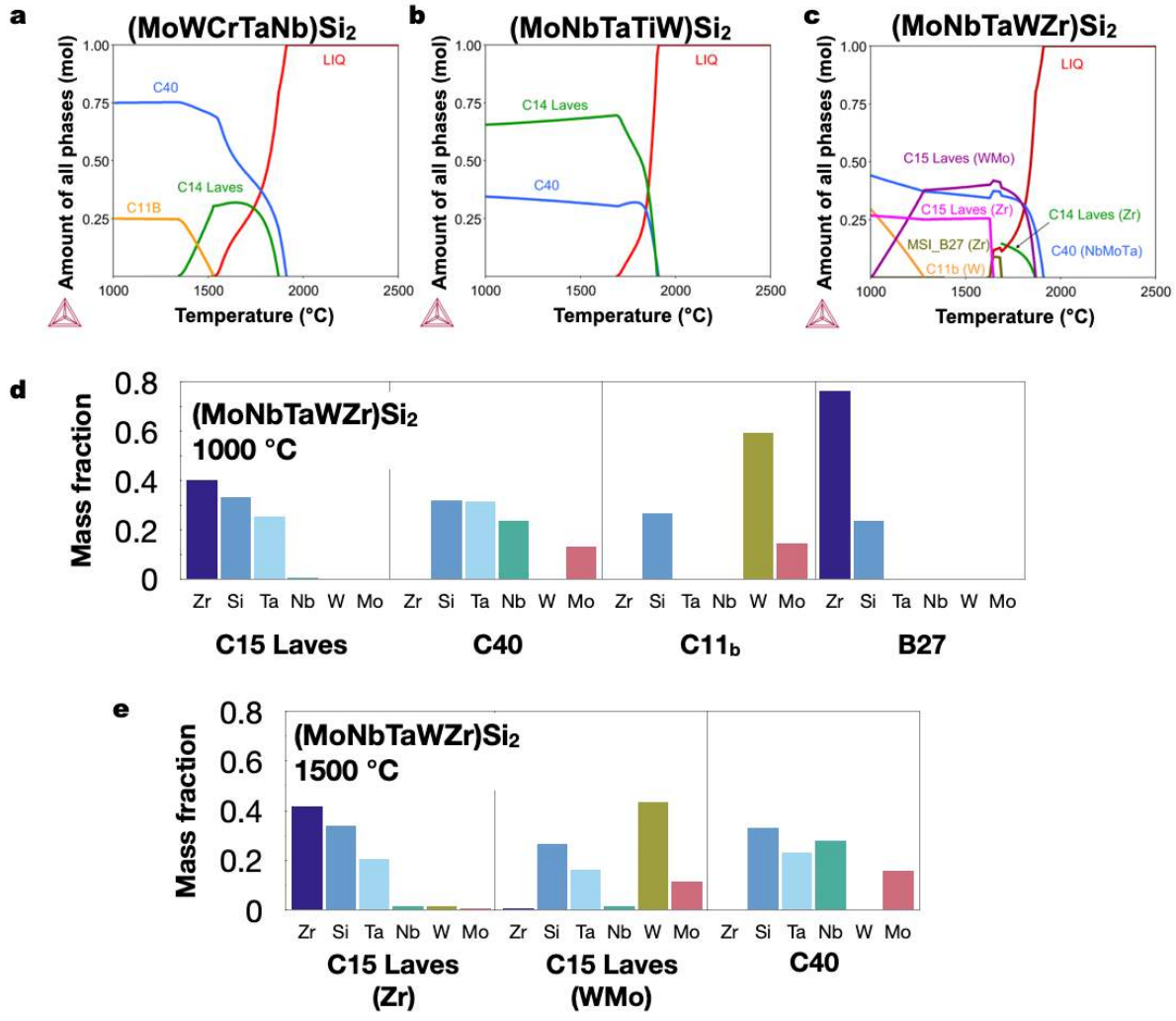

Figure 3.6. Calculated equilibrium step diagrams of recently reported high entropy silicide materials. Materials suggested by (a) Liu et al. [1], and (b-c) Gild et al. [2] exhibit secondary phase formation, as compared to the material suggested in this work. Composition of the phases present in (MoNbTaWZr)Si_2 at d) 1000 °C and e) 1500 °C.

To fabricate the ternary (CrMoTa)Si_2 HES, we sequentially deposited layers of Cr, Mo, and Ta onto a Si substrate with an equiatomic ratio of each constituent metal. The total thickness of the as-deposited ternary multilayer thin film was ~25 nm, as determined from a cross-sectional SEM micrograph **(Figure 3.7)**.

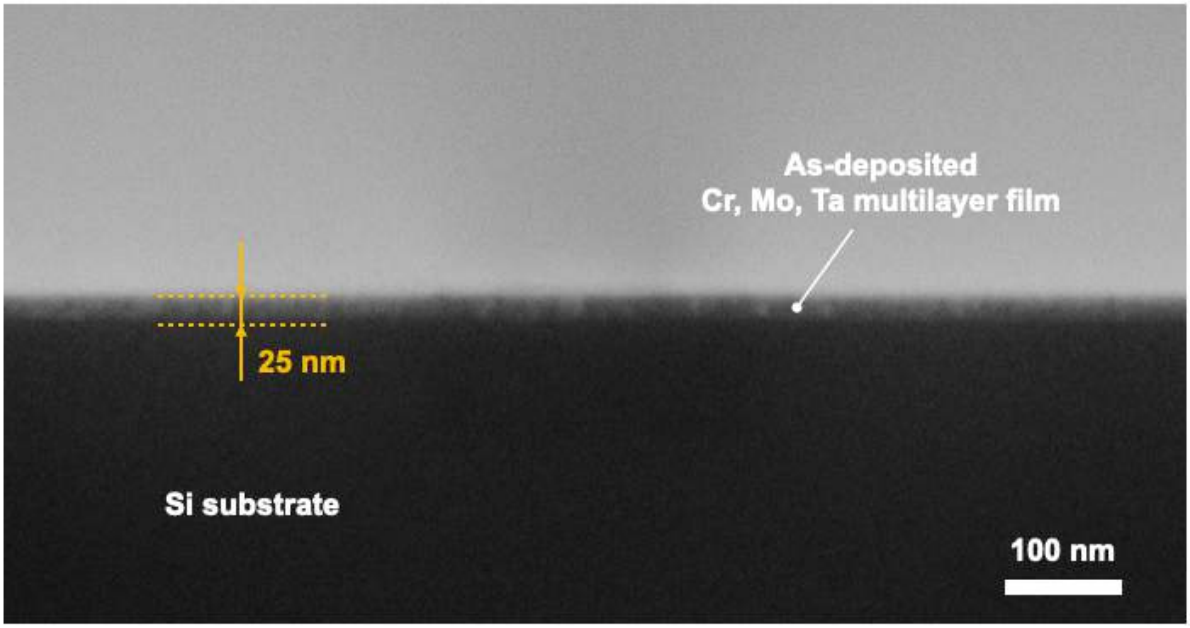

Figure 3.7. A cross-sectional SEM micrograph of the as-deposited Cr, Mo, Ta multilayer thin film.

To determine the appropriate heat treatment conditions for fully reacting the multilayer thin film, we evaluated several discrete temperature/time combinations between 800-900 °C and 30-60 min, and the corresponding GIXRD patterns collected from the heat-treated samples are shown in **Figure 3.8**. It was found that heat treating the multilayer structure at 900 °C for 30 min yielded a single-phase material with a C40 hexagonal crystal structure with no extraneous peaks, indicating a complete transformation of the multilayer structure to the single (CrMoTa)Si_2 phase.

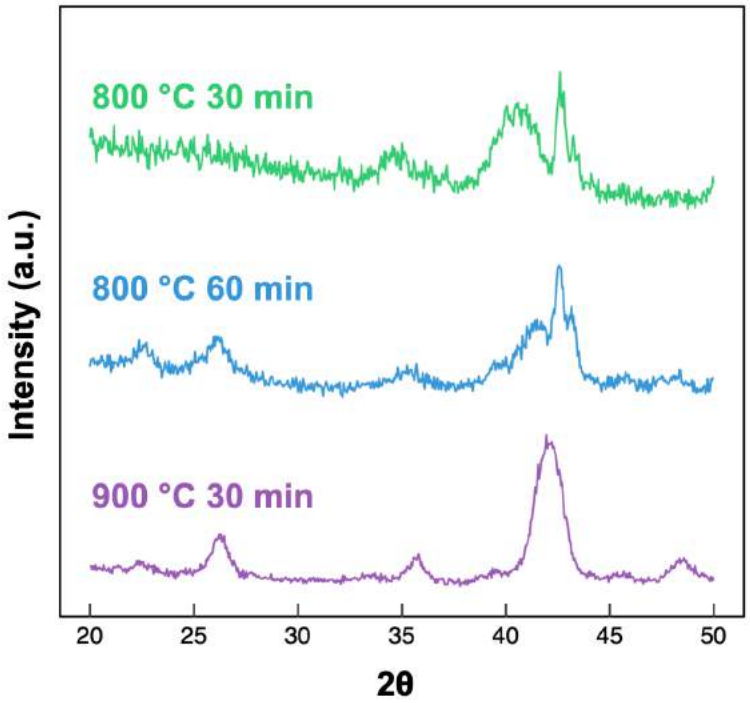

Figure 3.8. Heat treatment optimization on the ternary (CrMoTa)Si2 high entropy material. GIXRD patterns collected at ω = 0.5° indicate that heat treatment at 900 °C for 30 min yields a single-phase high entropy silicide with a C40 hexagonal crystal structure.

GIXRD patterns for the as-deposited ternary multilayer thin film exhibited a broad peak centered around ~37° **(Figure 3.9, a)**, which was indexed to the (110) set of lattice planes of the body-centered cubic (BCC) structures of Cr, Mo and Ta. Formation of a single phase with a C40 hexagonal crystal structure in (CrMoTa)Si_2 is not surprising given that the constituent silicides $CrSi_2$ and $MoSi_2$ both stabilize in the C40 hexagonal crystal structure [166], and the C40 β-$MoSi_2$ phase is metastable relative to the tetragonal α-$MoSi_2$ $C11_b$ phase [172]. Additionally, (MoTa)Si_2 stabilizes a single C40 phase at ~0.45-1.0 mole fractions of $TaSi_2$, and (CrMo)Si_2 stabilizes a single C40 phase at ~0.65-1.0 mole fractions of $CrSi_2$ [173]. The (CrMoTa)Si_2 ternary has also been shown to form a single C40 phase at near-equiatomic compositions [173].

GIXRD depth profiling was then used to confirm the phase uniformity of the reacted ternary (CrMoTa)Si_2 silicide thin film after heat treatment at 900 °C for 30 min **(Figure 3.9, b)**. All GIXRD patterns were indexed to the C40 hexagonal crystal structure, confirming that the solid-state reaction yielded a uniform single-phase state throughout the thickness of the thin film. A single extraneous peak observed in the ω = 0.2° pattern at ~33.6° can be potentially attributed to the surface oxidation of the Ta layer and formation of Ta_2O_5 [174], since the Ta layer was deposited last and, therefore, was exposed to air during sample manipulation. Observation of the single C40 phase in the (CrMoTa)Si_2 HES thin film confirmed our CALPHAD predictions **(Figure 3.4, a)**.

A SEM micrograph of the fracture cross-section of the reacted ternary (CrMoTa)Si_2 HES thin film is presented in **Figure 3.9, c**. Voids were observed to be distributed uniformly along the interface between the ternary (CrMoTa)Si_2 HES thin film and the Si substrate. The void formation is attributed to the Kirkendall effect, which occurs due to the majority atoms (Si) being more mobile than the minority atoms (Cr, Mo and Ta) [175]. The reacted ternary (CrMoTa)Si_2 HES thin film was ~42 nm in thickness, which constituted a ~70% increase in thickness compared to the as-deposited multilayer thin film. The growth of the thin film after heat treatment is indicative of Si incorporation into the metal film during the heat treatment. The thickness of the reacted thin film was in line with the ~37 nm thickness predicted from the theoretical density of 6.97 g/cm^3. Theoretical density was calculated based on the lattice parameters obtained from full-pattern refinement (**Table 3.3**) for the C40 hexagonal crystal structure with equal probability of site occupation by Cr, Mo and Ta atoms assuming ideal stoichiometry. The thin film exhibited a uniform microstructure (**Figure 3.9, d**), with an average grain size of 40 ± 3 nm. Additionally, no obvious cracks or pores were observed on the surface of the thin film. The Kirkendall voids

under the thin film appeared as dark regions in the top-down micrograph due to fewer emitted secondary electrons.

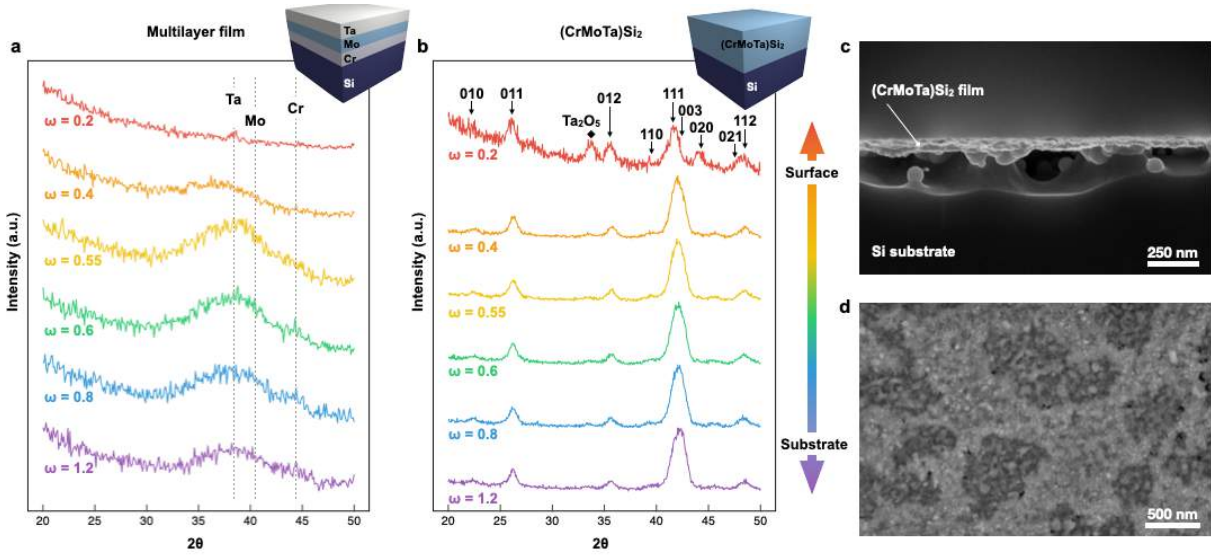

Figure 3.9. Characterization of the as-deposited Cr, Mo and Ta multilayer thin film and the reacted ternary (CrMoTa)Si2 high entropy silicide (HES) thin film. a) Grazing incidence X-ray diffraction (GIXRD) patterns collected from the as-deposited multilayer Cr, Mo and Ta thin film reveal a broad peak attributed to the (110) planes of the elemental BCC Cr, Mo and Ta (indicated with dashed lines). b) GIXRD patterns collected from the ternary (CrMoTa)Si2 HES thin film after heat treatment at 900 °C for 30 min reveal a single-phase material with a C40 hexagonal crystal structure with some surface oxidation. c) A SEM micrograph of a fracture cross-section of the ternary (CrMoTa)Si2 HES thin film on Si substrate. d) A top-down SEM micrograph showing the nanocrystalline ternary (CrMoTa)Si2 HES thin film.

We used the approach developed for the ternary $(CrMoTa)Si_2$ HES thin film to fabricate a quinary $(CrMoTaVNb)Si_2$ HES. To avoid the surface oxidation observed in the ternary $(CrMoTa)Si_2$ thin film (**Figure 3.9, b** at $\omega = 0.2°$), we revised the deposition order of the constituent metals. The five metals were deposited according to their room temperature Gibbs free energy of oxide formation (ΔG_f): the Ta layer was deposited first (ΔG_f = -1911 kJ/mol), followed by V (ΔG_f = -1803 kJ/mol), Nb (ΔG_f = -1766 kJ/mol), Cr (ΔG_f = -1053 kJ/mol), and, finally, Mo (ΔG_f = -668 kJ/mol) [176]. The metals were deposited in equiatomic ratios, and the thickness of the as-deposited

multilayer thin film, as determined from a SEM micrograph the of fracture cross-section, was ~42 nm **(Figure 3.10)**. GIXRD patterns obtained from the as-deposited multilayer thin film **(Figure 4, a)** exhibited a broad peak at ~38°, which was indexed to the (110) peaks of Ta, Nb and Mo. Another peak present at ~42° was attributed to the (110) lattice planes of elemental V.

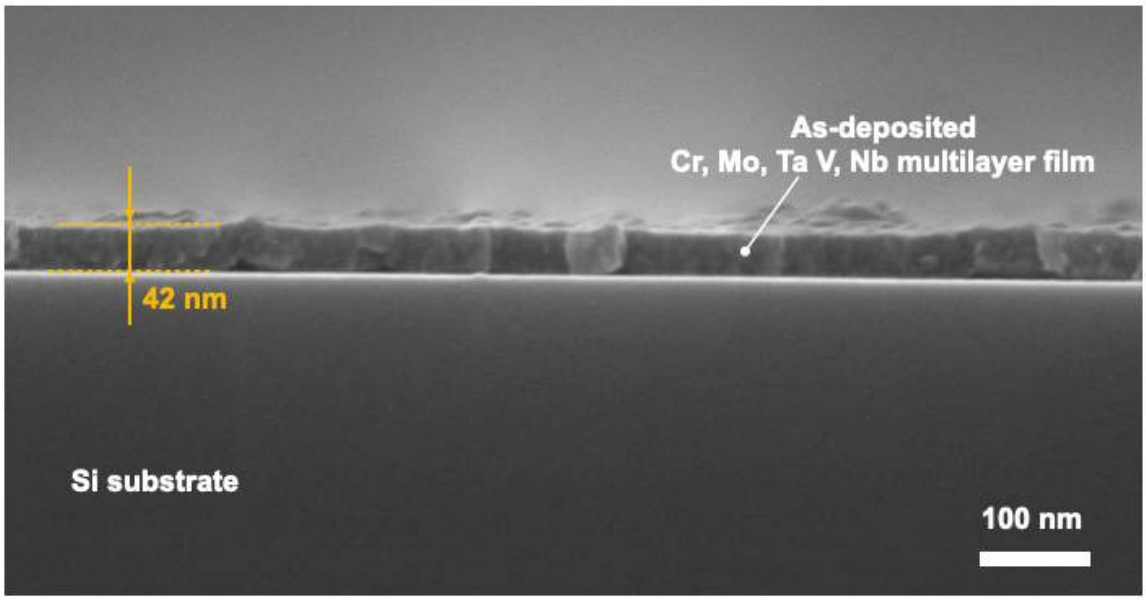

Figure 3.10. A cross-sectional SEM micrograph of the as-deposited Cr, Mo, Ta, V and Nb multilayer thin film.

Following the procedure previously established for the ternary (CrMoTa)Si_2 thin film, the as-deposited Cr, Mo, Ta, V, Nb multilayer thin film was then heat treated at 900 °C for 30 minutes, and its phase composition was evaluated through GIXRD **(Figure 3.11, b)**. The diffraction patterns exhibited peaks indexed to the C40 hexagonal crystal structure throughout the entire thickness of the thin film, confirming the CALPHAD predictions of phase formation in (CrMoTaVNb)Si_2. Similar to the ternary (CrMoTa)Si_2, formation of a single phase with a C40 hexagonal crystal structure is expected in (CrMoTaVNb)Si_2 due to the prevalence of the C40 crystal structure in the constituent silicides $CrSi_2$, $MoSi_2$, $TaSi_2$, VSi_2 and $NbSi_2$ [173].

Formation of a single phase with a C40 hexagonal crystal structure in the $(CrMoTa)Si_2$ ternary silicide discussed above also supports this finding. No secondary phases were evident from the diffraction patterns, indicating a complete reaction to the high entropy $(CrMoTaVNb)Si_2$ single phase. In contrast to the ternary $(CrMoTa)Si_2$ HES **(Figure 3.9, b)**, no surface oxidation was observed in the $(CrMoTaVNb)Si_2$ HES.

A cross-sectional SEM micrograph of the reacted quinary $(CrMoTaVNb)Si_2$ HES thin film **(Figure 3.11, c)** revealed that the thin film grew to ~101 nm in thickness after heat treatment. The ~143% increase in thickness is attributed to the incorporation of Si atoms from the substrate during the reaction process. The thickness of the reacted thin film is ~21% larger than the ~80 nm thickness predicted from the theoretical density of 6.25 g/cm^3. The deviation from the predicted thickness can be attributed to thin film porosity, as well as potential errors in thickness measurements of metal layers during electron beam evaporation. Kirkendall voids were observed at the interface between the thin film and the substrate, indicating a similar reaction process to the ternary $(CrMoTa)Si_2$ sample. However, these voids were not observed from a top-down view due to the larger thin film thickness (Figure 4d). The quinary $(CrMoTaVNb)Si_2$ HES thin film exhibited a nonuniform grain size distribution, with grains ranging from ~145 nm to ~280 nm and an average grain size of 198 ± 13 nm. The increase in grain size compared to the ternary thin film can be attributed to abnormal grain growth associated with the more complex solid-state reaction process required to form the quinary sample.

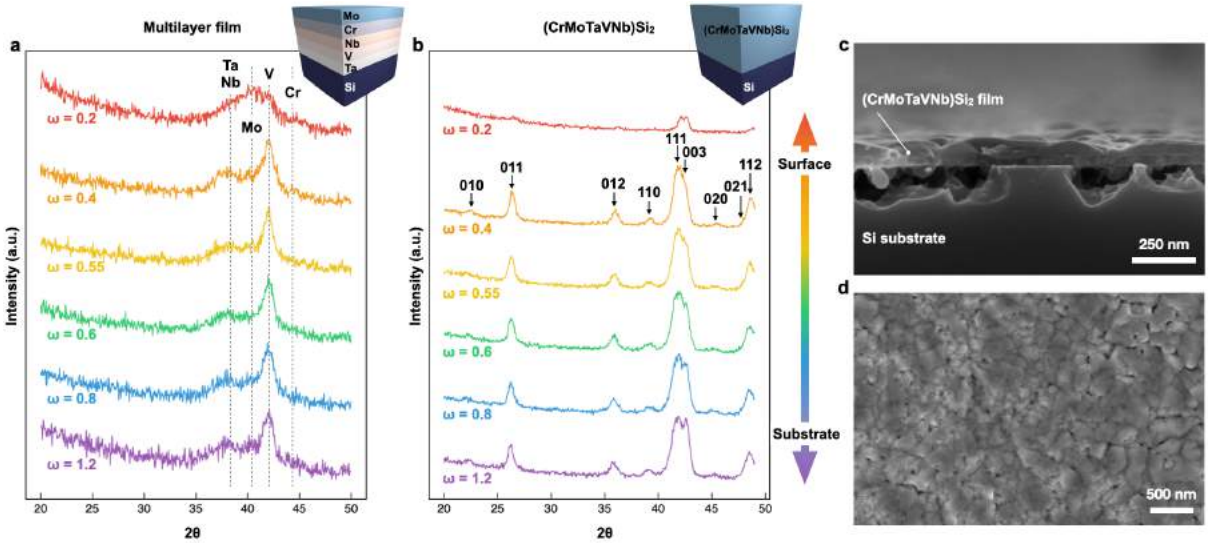

Figure 3.11. Characterization of the as-deposited Cr, Mo, Ta, V, Nb multilayer thin film and the reacted quinary (CrMoTaVNb)Si_2 high entropy silicide (HES) thin film. a) Grazing incidence X-ray diffraction (GIXRD) patterns collected from the as-deposited multilayer thin film reveal peaks attributed to the (110) planes of the elemental Cr, Mo, Ta, V, Nb (indicated with dashed lines). b) GIXRD patterns collected from the reacted quinary (CrMoTaVNb)Si_2 HES thin film after heat treatment at 900 °C for 30 min demonstrate a single-phase material with a C40 hexagonal crystal structure. c) A cross-sectional SEM micrograph showing the reacted quinary (CrMoTaVNb)Si_2 HES thin film on a Si substrate. e) A top-down SEM micrograph showing the reacted quinary (CrMoTaVNb)Si_2 HES thin film.

A homogenous elemental distribution was confirmed through EDS mapping **(Figure 3.12)** of the reacted quinary (CrMoTaVNb)Si_2 thin film, which revealed no large-scale segregation nor secondary phases. It is important to note that nanoscale segregation cannot be determined with SEM-based spectroscopy, and TEM-based experiments are required to confirm that no nanoscale precipitates are present within the sample.

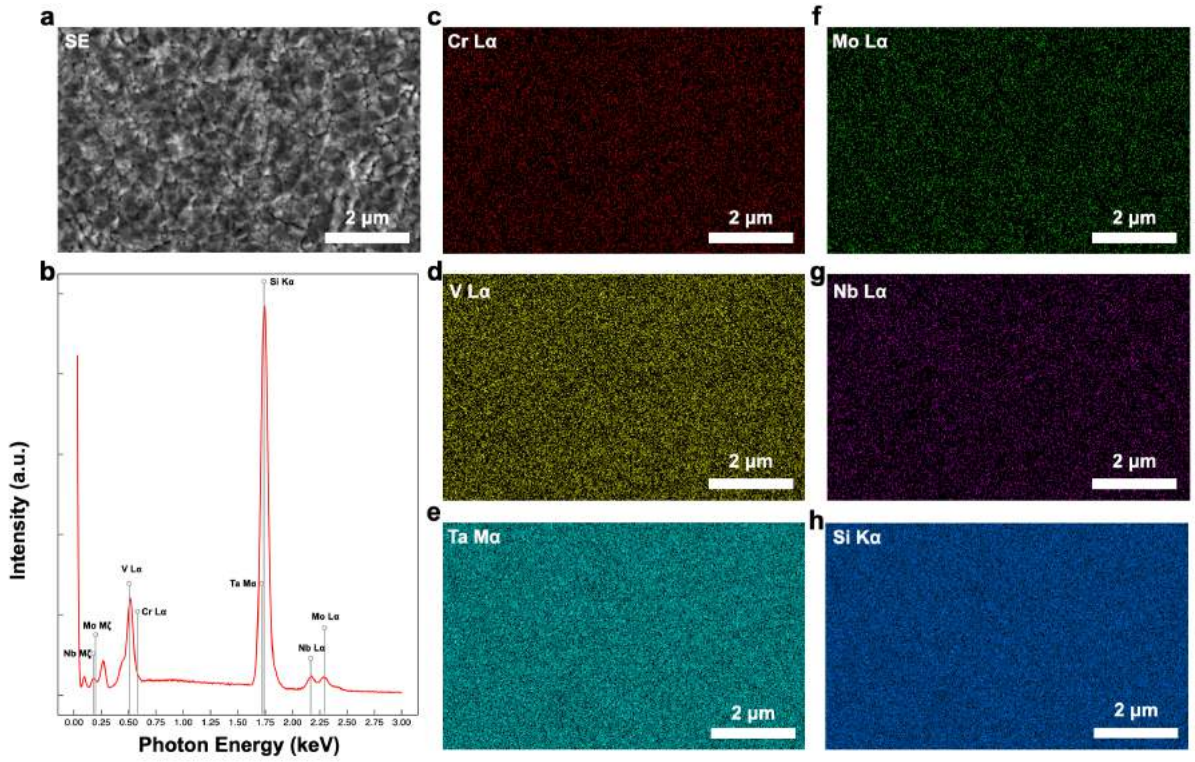

Figure 3.12. Energy-dispersive spectroscopy (EDS) mapping of the reacted quinary (CrMoTaVNb)Si_2 high entropy silicide. a) A secondary electron image, b) EDS spectrum, c-h) elemental maps.

Quantitative analysis using Rietveld refinement was performed on the diffraction patterns obtained from both HES materials at ω = 0.55°. A Rietveld plot for the (CrMoTaVNb)Si_2 quinary HES is presented in **Figure 3.13**. Observed differences in intensity between the observed and calculated data can be potentially attributed to crystallographic texture present in the thin film. Overall, low fit residuals suggest that the pattern was refined well.

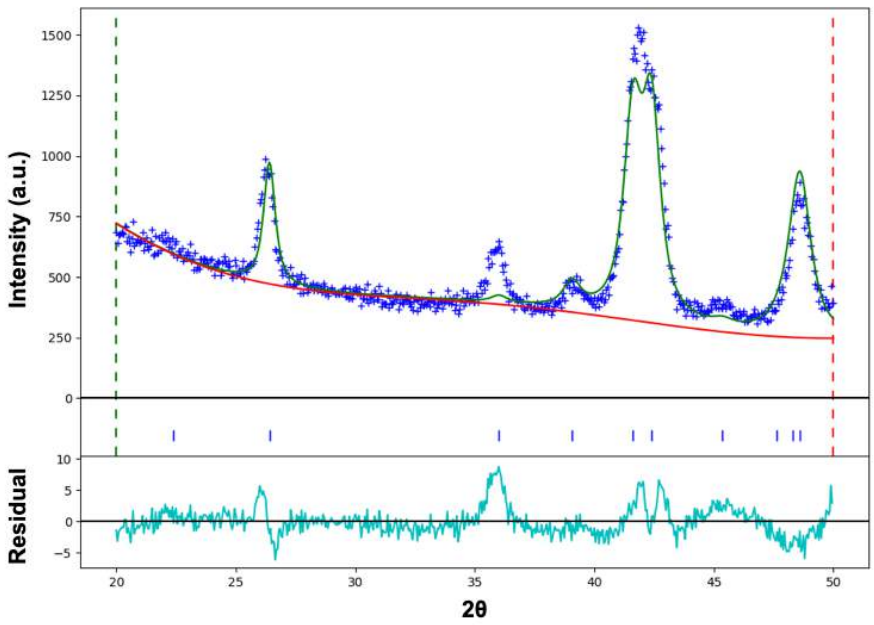

Figure 3.13. A Rietveld plot for the quinary (CrMoTaVNb)Si_2. The blue symbols indicate the observed data, while the green line represents the calculated diffraction pattern. Residuals are shown in cyan trace. Calculated Bragg reflection positions are indicated by blue dashes.

The measured lattice parameters *a* and *c* were compared to the lattice parameters calculated from Vegard's law [177] **(Table 3.3)**. The difference between the measured and the calculated lattice parameters is <0.35% for *a* and <1.5% for *c*. The close correspondence of the measured and calculated lattice parameters indicates that both the ternary and quinary HES materials fabricated in this work follow the ideal rule of mixing and have solid-solution structures. We interpret this agreement with Vegard's law as a confirmation that all of the constituent metal elements have been incorporated on the cation sublattice of the C40 hexagonal solid-solution crystal structure.

Table 3.3. Lattice parameters of $(CrMoTa)Si_2$ and $(CrMoTaVNb)Si_2$ HES with a C40 hexagonal crystal structure.

Material	a (nm)	c (nm)	Axial ratio c/a	Reference
$CrSi_2$ (experimental)	0.4428	0.6368	1.438	[166]
β-$MoSi_2$ (experimental)	0.4596	0.6550	1.425	[166]
$TaSi_2$ (experimental)	0.4784	0.6570	1.373	[166]
VSi_2 (experimental)	0.4572	0.6373	1.394	[166]
$NbSi_2$ (experimental)	0.4797	0.6592	1.374	[166]
$(CrMoTa)Si_2$ Rietveld (experimental)	0.4618	0.6423	1.391	This work
$(CrMoTa)Si_2$ Vegard's Law (calculated)	0.4602	0.6496	1.411	This work
$(CrMoTaVNb)Si_2$ Rietveld (experimental)	0.4644	0.6437	1.386	This work
$(CrMoTaVNb)Si_2$ Vegard's Law (calculated)	0.4635	0.6491	1.400	This work

3.4 Conclusions

In conclusion, we demonstrated the successful implementation of the CALPHAD approach to the design of compositionally complex high entropy silicide systems. We identified two single-phase HES materials: the ternary $(CrMoTa)Si_2$ and quinary $(CrMoTaVNb)Si_2$. The HES materials were fabricated via electron beam evaporation followed by a solid-state reaction facilitated by heat treatment in vacuum. As evidenced by GIXRD, both $(CrMoTa)Si_2$ and $(CrMoTaVNb)Si_2$ exhibited a single phase with a C40 hexagonal crystal structure, corroborating our CALPHAD predictions. Lattice parameters obtained from the experimental GIXRD patterns after full pattern refinement were in close alignment with lattice parameters calculated from

Vegard's law, indicating incorporation of all constituent elements onto the metal sublattice of the C40 hexagonal phase. Our fabrication process is compatible with industry-standard deposition processes used in microelectronics, which opens the door for HES consideration in IC and device applications. In addition, our thin film fabrication process is compatible with high-throughput materials synthesis and characterization techniques, potentially enabling fast and facile screening of novel scientifically interesting HES materials. This work is the first report of a rationally selected, experimentally synthesized thin film single-phase high entropy silicide.

3.5 Legacy experiments and future work

In our previous work on HES, we demonstrated successful fabrication of HES thin films via electron beam evaporation followed by heat treatment in vacuum. In this approach, elemental metals were deposited in a layer-by-layer fashion onto a Si substrate (**Figure 3.14, a**). This approach has two main drawbacks: 1) as-deposited films are multilayer stacks, which makes complete intermixing of metals and diffusion of Si through the entire thickness of the film challenging; 2) since Si is the main diffusing species, Kirkendall voids are formed under the film (**Figure 3.9 and Figure 3.11**), which might promote film delamination from the substrate and complicate characterization of electrical and mechanical properties.

To promote intermixing of the elements during fabrication of HES thin films, as well as to prevent formation of large-area Kirkendall voids, we investigated synthesizing HES materials using magnetron co-sputtering. In this approach, all five targets were operated concurrently, producing a pre-mixed thin film as shown in **Figure 3.14, b**. In addition, we investigated co-sputtering of Si together with Cr, Mo, Ta, V, and Nb as an approach to prevent void formation during the solid-state reaction.

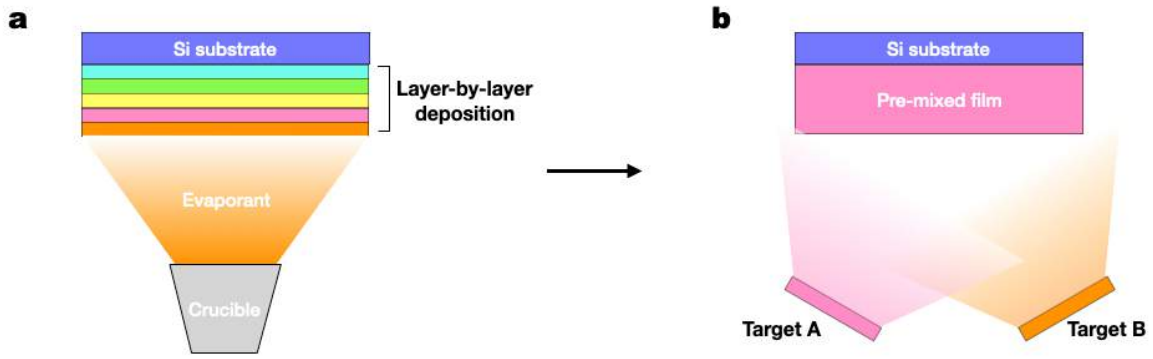

Figure 3.14. A schematic illustration of two high entropy silicide film deposition strategies: a) layer-by-layer electron beam evaporation, b) deposition of a premixed film via magnetron sputtering.

3.5.2 Materials and methods

HES thin films were deposited using a large-distance magnetron sputtering system (Createc Fischer & Co. GmbH, Erligheim, Germany) equipped with eight magnetrons arranged in an octagonal geometry (**Figure 3.15**). Prior to deposition, the chamber was evacuated to a base pressure of ~1.5 x 10^{-8} mbar. After the base pressure was reached, sputtering was performed using a flux of 40 sccm of Ar. Ta and Nb targets were connected to RF power supplies, while Cr, Mo, V and Si targets were connected to DC power supplies. Polished Si wafers of 2" in diameter and (100) orientation were used as substrates (SurfaceNet GmbH, Rheine, Germany). Sputtering rate calibration of individual elements was performed prior to deposition of HES films.

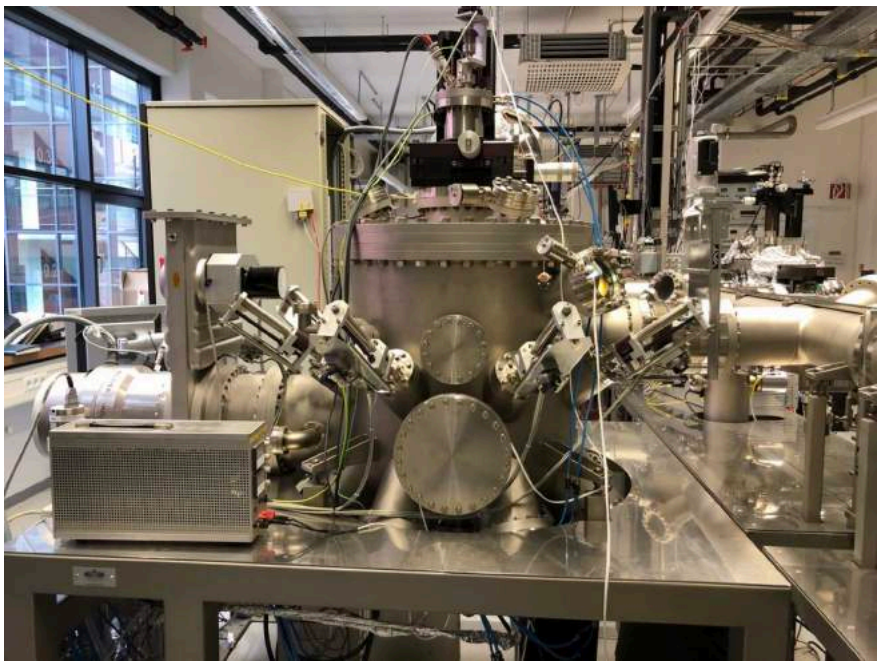

Figure 3.15. Createc Fischer magnetron sputtering system.

After deposition, the samples were heat treated in a vacuum tube furnace evacuated to a pressure of ~1.2 x 10^{-8} mbar at 900 °C for 3 hours. After heat treatment, the heating was turned off and the samples were cooled to room temperature naturally inside the furnace.

Phase state of the as-deposited and heat treated HES films was characterized using grazing incidence X-ray diffraction (GIXRD) with a D8 Discover diffractometer (Bruker, Billerica, MA, USA).

Morphology of the films was investigated using a Magellan 400 XHR scanning electron microscope (FEI, Hillsboro, Oregon, USA) outfitted with a through-the-lens detector and operated in immersion mode. Cross-sectional imaging was performed using fracture cross-sections. Atomic force microscopy (AFM) was performed in contact mode using a Tosca system (Anton Paar, Graz, Austria).

Sheet resistance R_s was measured using the RM3000 Test Unit (Jandel, Leighton Buzzard, United Kingdom) with a linear four-point probe (1 mm distance

between the electrodes) connected to a current source and a digital voltmeter. The resistivity and conductivity of the films was determined using the following relationships:

$$\rho = R_s \cdot t$$

$$\sigma = \frac{1}{\rho}$$

where ρ –electrical resistivity (Ω·m), t – film thickness (nm), σ – conductivity (S/m).

3.5.3 Results and Discussion

In this work, we evaluated two samples: 1) a sample with Cr, Mo, Ta, V and Nb metals co-deposited onto a Si substrate in an equiatomic ratio, and 2) a sample with Cr, Mo, Ta, V, Nb and Si co-deposited onto a Si substrate to produce the (CrMoTaVNb)Si_2 stoichiometry. The two samples will be further referred to as "(CrMoTaVNb)Si_2 sample with diffused Si" and "(CrMoTaVNb)Si_2 sample with deposited Si", respectively.

First, we evaluated the phase composition of both samples using GIXRD. For the (CrMoTaVNb)Si_2 sample with diffused Si in the as-deposited state, sharp diffraction peaks indexed to the body-centered cubic (BCC) crystal structure were observed (**Figure 3.16, left**). The GIXRD patterns indicate that the as-deposited sample formed a single phase with a BCC structure. We can speculate that the as-deposited sample formed a high entropy alloy (HEA) film. Upon heat treatment in vacuum at 900 °C for 3 hours, a solid-state phase transformation from the BCC to C40 hexagonal structure was observed (**Figure 3.16, right**), which indicates a successful diffusion of Si into the HEA layer. However, additional peaks corresponding to a secondary phase were also observed. The presence of the secondary phase can be

attributed to insufficient heat treatment time or temperature, as previously observed in the electron-beam-deposited films (**Figure 3.8**).

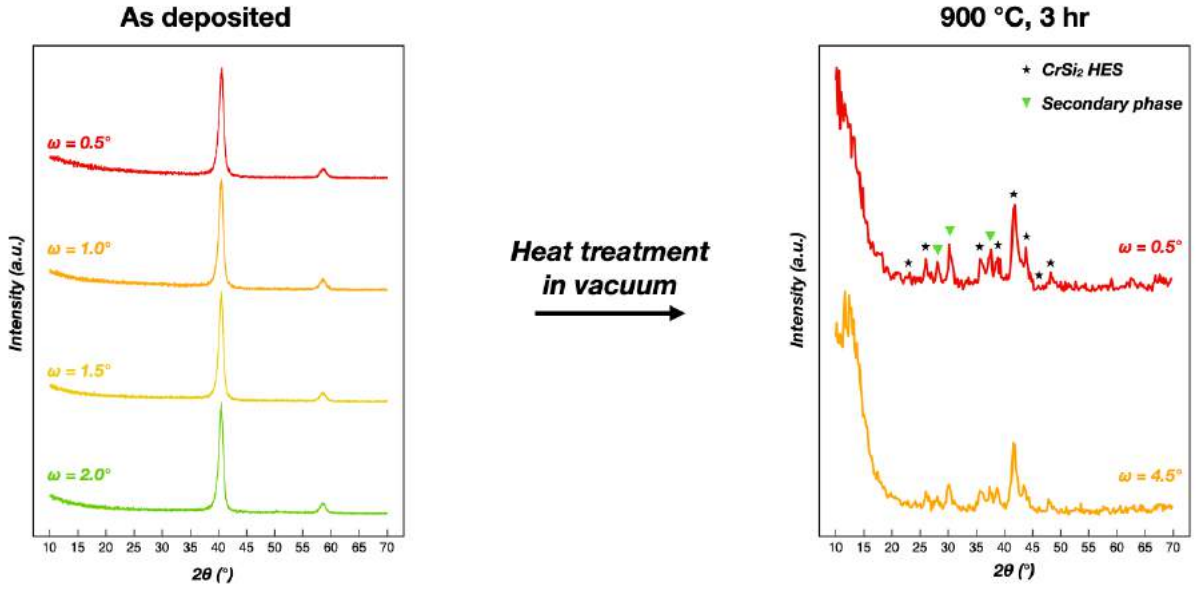

Figure 3.16. Grazing incidence X-ray diffraction patterns of the (CrMoTaVNb)Si_2 sample with diffused Si. As-deposited material (left) is crystalline and has a body-centered cubic structure. After heat treatment at 900 °C for 3h, material forms the target hexagonal C40 crystal structure along with a secondary phase, indicating an incomplete solid-state transformation (right).

We continued characterization by evaluating the (CrMoTaVNb)Si_2 sample with deposited Si. GIXRD patterns of the as-deposited sample feature a broad peak centered at the 2θ angle of ~40° (**Figure 3.17, left**). The broad peak suggests that the as-deposited material is amorphous. It is likely that high quenching speed of the sputtering process, combined with high crystallization temperature of Si (~ 720 °C) prevented crystallization of the film during deposition [178]. Heat treatment in vacuum at 900 °C induced the solid-state transformation of the material to the target C40 hexagonal crystal structure (**Figure 3.17, right**). No extraneous peaks are observed, suggesting either that no secondary phases are present or that secondary phases are present in the amount below the GIXRD detection limit.

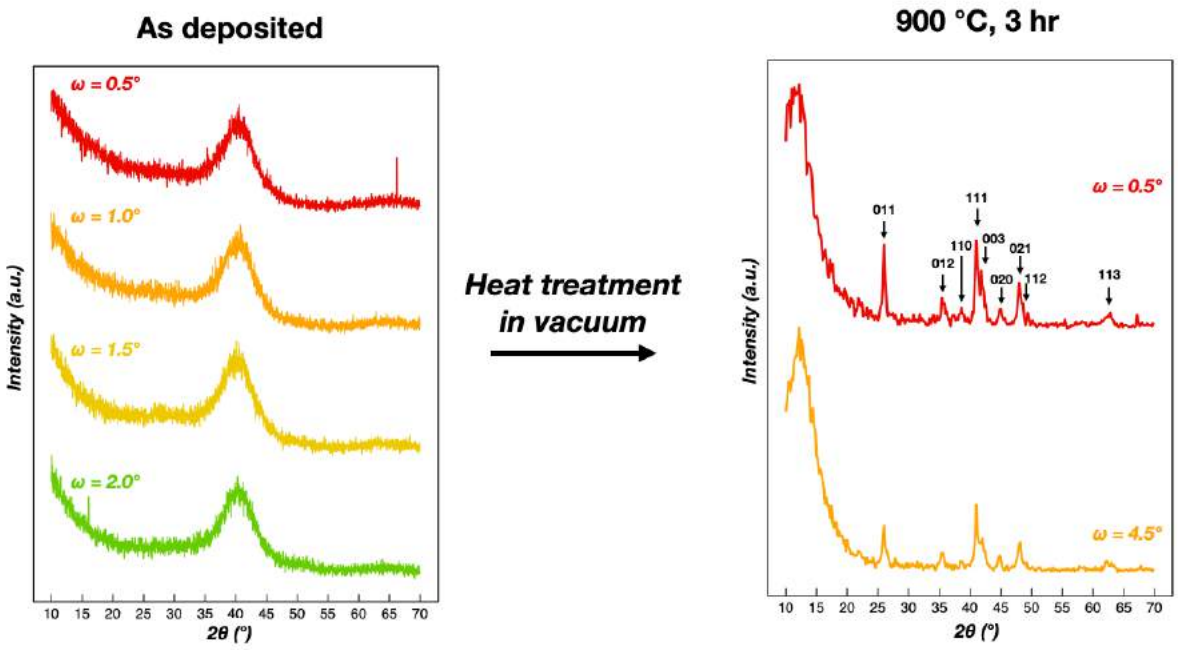

Figure 3.17. Grazing incidence diffraction (GIXRD) patterns of the (CrMoTaVNb)Si_2 sample with deposited Si. As-deposited material (left) exhibits broad peaks, potentially indicating its amorphous state. After heat treatment treatment at 900 °C for 3h, material forms the target C40 hexagonal crustal structure with no extraneous phases identified by GIXRD (right).

Morphology and thickness of the (CrMoTaVNb)Si_2 thin film with deposited Si was evaluated using top-down (**Figure 3.18, a**) and cross-sectional (**Figure 3.18, b**) SEM. No grain boundaries are apparent in the as-deposited film (**Figure 3.18, a, left**), confirming the XRD results and suggesting that the as-deposited film is amorphous. Upon heat treatment, nearly equiaxed grains of ~100 nm in size are formed (**Figure 3.18, a, right**). Cross-sectional SEM imaging revealed a three-fold growth of the film in thickness upon heat treatment, from ~53 nm to ~156 nm thick (**Figure 3.18, b**). The observed dramatic increase in film thickness potentially indicated incorporation of some Si atoms from the substrate, although no significant voiding at the interface between the film and the substrate was observed. AFM mapping of the heat-treated film (**Figure 3.18, a, right**) reveals a root mean square (RMS) roughness of ~7.4 nm or ~4.7% of the total film thickness.

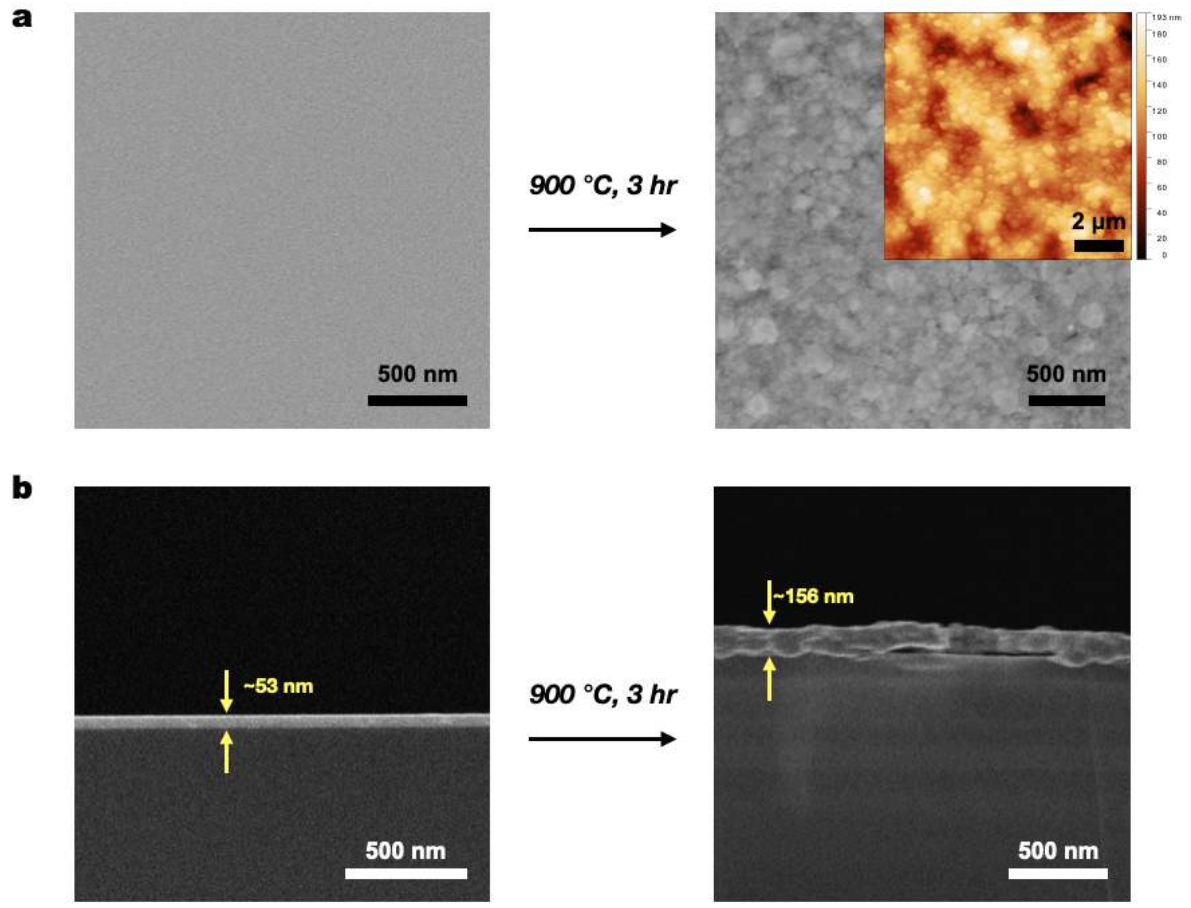

Figure 3.18. Scanning electron microscopy imaging of the high entropy silicide film with co-deposited Si. a) Top-down view of the as-deposited film reveals uniform microstructure with no apparent grain boundaries. Upon heat treatment at 900 °C for 3h, formation of a nearly equiaxed nanocrystalline structure is observed. Inset shows an atomic force microscopy micrograph of the heat treated sample. b) Cross-sectional imaging of the as-deposited and heat treated films demonstrates thickness growth from ~53 nm to ~156 nm following heat treatment.

Next, we measured sheet resistance of the (CrMoTaVNb)Si_2 thin film with deposited Si using the four-point-probe method [179]. In as-deposited state, sheet resistance was found to be ~52 Ω/□, and in the heat treated state - ~22 Ω/□ (**Table 3.4**). Electrical resistivity and conductivity were calculated based on sheet resistance and film thickness. In the as-deposited state, the film has a resistivity of ~276 μΩ·cm, while the resistivity of the heat treated film is ~27% higher at ~350 μΩ·cm.

Table 3.4. Electrical properties of the (CrMoTaVNb)Si_2 thin film with deposited Si.

Sample	Film thickness (nm)	Sheet resistance (Ω/□)	Resistivity (μΩ·cm)	Conductivity (S/m)
As deposited	53	52	276	3.6
Heat treated	156	22	350	2.9

If we compare the electrical resistivity of the (CrMoTaVNb)Si_2 thin film with resistivities of the constituent binary disilicides (**Figure 3.19**), we find that it falls within the range of resistivities reported in the literature [166,180–184]. The close correspondence of the electrical properties of the high entropy silicide to those of binary silicides suggests that random occupation of the metal sublattice sites does not significantly deteriorate electrical conductivity of the material.

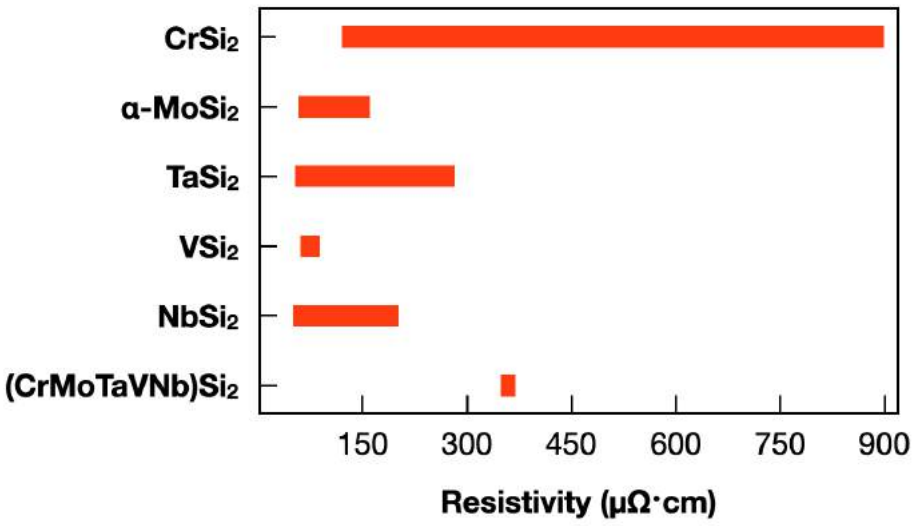

Figure 3.19. Resistivity of the (CrMoTaVNb)Si_2 high entropy silicide (HES) as compared to resistivities of constituent binary disilicides. Data for $CrSi_2$, $MoSi_2$, $TaSi_2$, VSi_2 and $NbSi_2$ obtained from references [166,180–184].

3.5.4 Scope of future work

Our preliminary results suggest that we were able to fabricate a single-phase HES film using magnetron co-sputtering followed by heat treatment in vacuum. Furthermore, the heat treated film demonstrated resistivity of ~350 μΩ·cm, which falls within the range of resistivity of the constituent binary silicides.

We will continue characterization of the quinary HES films deposited via magnetron co-sputtering by performing the following experiments:

1) Chemical composition mapping using SEM EDS and STEM EDS;
2) *In situ* TEM observation of amorphous-to-crystalline transformation of the as-deposited film during heat treatment;
3) Characterization of mechanical properties using nanoindentation.

CONCLUSIONS

In this dissertation, research questions in two major areas were addressed. In chapters 1 and 2, key aspects of metal additive manufacturing, i.e., microstructural inhomogeneities within as-built components and residual stress, were discussed. Chapter 3 introduced a novel single-phase high entropy silicide material that lends itself to thin film processing.

We started by investigating the influence of part geometry on the microstructure of additively manufactured stainless steel. We fabricated parts with varying feature sizes using laser powder bed fusion (LPBF). The microstructure of the parts and local plastic deformations within features of different thickness were characterized via electron backscatter diffraction. We found that feature thickness has a dramatic impact on the microstructure. However, the microstructure could be successfully manipulated by adjusting the LPBF process parameters. This study provides a foundation for future work on LPBF process optimization to improve the mechanical properties and corrosion resistance of the as-printed parts.

We continued our work on additive manufacturing by investigating the feasibility of alloy engineering for residual stress manipulation. Inspired by the use of low temperature transformation wires in welding, we studied two metals: pure Fe and Fe-50Cu (wt.%) binary alloy. We determined that solid-state transformations undergone by the material during cooling have a dramatic effect on surface residual stresses in additively manufactured parts. We were able to induce beneficial compressive stresses on the surface of Fe-50Cu parts. Overall, this study proved that residual stress resistance can serve as a criterion in alloy design for additive manufacturing.

Finally, in chapter 3, we introduced a novel high entropy silicide (HES) material. In this work, we used computational modeling to select a composition that forms a single phase. We then successfully fabricated our HES material in thin film form via electron beam evaporation followed by heat treatment in vacuum. The fabricated material exhibited a single phase with the hexagonal C40 crystal structure, confirming our computational predictions. Additionally, we demonstrated fabrication of the HES material using magnetron co-sputtering. Electrical characterization of the HES material revealed good conductivity in line with the constituent binary disilicides.

REFERENCES

[1] M. Acuto, COVID-19: Lessons for an Urban(izing) World, One Earth. 2 (2020) 317–319. doi:10.1016/j.oneear.2020.04.004.

[2] C. Connolly, R. Keil, S.H. Ali, Extended urbanisation and the spatialities of infectious disease: Demographic change, infrastructure and governance, Urban Stud. 58 (2021) 245–263. doi:10.1177/0042098020910873.

[3] J.F.B. Mitchell, J. Lowe, R.A. Wood, M. Vellinga, Extreme events due to human-induced climate change, Philos. Trans. R. Soc. A Math. Phys. Eng. Sci. 364 (2006) 2117–2133. doi:10.1098/rsta.2006.1816.

[4] H.E. Huppert, R.S.J. Sparks, Extreme natural hazards: Population growth, globalization and environmental change, Philos. Trans. R. Soc. A Math. Phys. Eng. Sci. 364 (2006) 1875–1888. doi:10.1098/rsta.2006.1803.

[5] A.D. Franklin, S.J. Han, G.S. Tulevski, M. Luisier, C.M. Breslin, L. Gignac, M.S. Lundstrom, W. Haensch, Sub-10 nm carbon nanotube transistor, Tech. Dig. - Int. Electron Devices Meet. IEDM. (2011) 9–13. doi:10.1109/IEDM.2011.6131600.

[6] X. Du, I. Skachko, A. Barker, E.Y. Andrei, Approaching ballistic transport in suspended graphene, Nat. Nanotechnol. 3 (2008) 491–495. doi:10.1038/nnano.2008.199.

[7] R. Rajagopalan, Y. Tang, X. Ji, C. Jia, H. Wang, Advancements and Challenges in Potassium Ion Batteries: A Comprehensive Review, Adv. Funct. Mater. 30 (2020) 1–35. doi:10.1002/adfm.201909486.

[8] K. Chayambuka, G. Mulder, D.L. Danilov, P.H.L. Notten, Sodium-Ion Battery Materials and Electrochemical Properties Reviewed, Adv. Energy Mater. 8 (2018) 1–49. doi:10.1002/aenm.201800079.

[9] J.Y. Kim, J.W. Lee, H.S. Jung, H. Shin, N.G. Park, High-Efficiency Perovskite Solar Cells, Chem. Rev. 120 (2020) 7867–7918. doi:10.1021/acs.chemrev.0c00107.

[10] A. Züttel, Materials for hydrogen storage, Mater. Today. 6 (2003) 24–33. doi:10.1016/S1369-7021(03)00922-2.

[11] J. Graetz, New approaches to hydrogen storage, Chem. Soc. Rev. 38 (2009) 73–82. doi:10.1039/b718842k.

[12] J. Song, J. She, D. Chen, F. Pan, Latest research advances on magnesium and magnesium alloys worldwide, J. Magnes. Alloy. 8 (2020) 1–41. doi:10.1016/j.jma.2020.02.003.

[13] T.A. Schaedler, A.J. Jacobsen, A. Torrents, A.E. Sorensen, J. Lian, J.R. Greer, L. Valdevit, W.B. Carter, Ultralight metallic microlattices, Science (80-.). 334 (2011) 962–965. doi:10.1126/science.1211649.

[14] A. Vyatskikh, S. Delalande, A. Kudo, X. Zhang, C.M. Portela, J.R. Greer, Additive manufacturing of 3D nano-architected metals, Nat. Commun. 9 (2018) 593. doi:10.1038/s41467-018-03071-9.

[15] E.P. George, W.A. Curtin, C.C. Tasan, High entropy alloys: A focused review of

mechanical properties and deformation mechanisms, Acta Mater. 188 (2020) 435–474. doi:10.1016/j.actamat.2019.12.015.

[16] M. Orme, I. Madera, M. Gschweitl, M. Ferrari, Topology Optimization for Additive Manufacturing as an Enabler for Light Weight Flight Hardware, Designs. 2 (2018) 51. doi:10.3390/designs2040051.

[17] GE Additive, Why GE Additive's 3D Prtinted Catalyst Turboprop Engine Is Turning Heads?, (2019). https://www.ge.com/additive/stories/ge-additive-3d-printed-catalyst-turboprop-engine-turning-heads (accessed December 4, 2020).

[18] A. Good, A. Johnson, G. Hautaluoma, NASA's Perseverance Rover Bringing 3D-Printed Metal Parts to Mars, (2020). https://www.nasa.gov/feature/jpl/nasas-perseverance-rover-bringing-3d-printed-metal-parts-to-mars (accessed December 4, 2020).

[19] J.M. Waller, B.H. Parker, K.L. Hodges, E.R. Burke, J.L. Walker, Nondestructive Evaluation of Additive Manufacturing State-of-the-Discipline Report, 2014.

[20] C. Dordlofva, A. Lindwall, P. Törlind, Opportunities and challenges for additive manufacturing in space applications, in: Proc. Nord., 2016.

[21] F. Romei, A.N. Grubišić, D. Gibbon, Manufacturing of a high-temperature resistojet heat exchanger by selective laser melting, Acta Astronaut. 138 (2017) 356–368. doi:10.1016/j.actaastro.2017.05.020.

[22] C. Zhang, S. Wang, J. Li, Y. Zhu, T. Peng, H. Yang, Additive manufacturing of products with functional fluid channels: A review, Addit. Manuf. 36 (2020) 101490. doi:10.1016/j.addma.2020.101490.

[23] A.M. Roach, B.C. White, A. Garland, B.H. Jared, J.D. Carroll, B.L. Boyce, Size-dependent stochastic tensile properties in additively manufactured 316L stainless steel, Addit. Manuf. 32 (2020) 101090. doi:10.1016/j.addma.2020.101090.

[24] B. Brown, W. Everhart, J. Dinardo, Characterization of bulk to thin wall mechanical response transition in powder bed AM, Rapid Prototyp. J. 22 (2016).

[25] S.M.J. Razavi, B. Van Hooreweder, F. Berto, Effect of build thickness and geometry on quasi-static and fatigue behavior of Ti-6Al-4V produced by Electron Beam Melting, Addit. Manuf. 36 (2020) 101426. doi:10.1016/j.addma.2020.101426.

[26] X. Tan, Y. Kok, Y.J. Tan, G. Vastola, Q.X. Pei, G. Zhang, Y.W. Zhang, S.B. Tor, K.F. Leong, C.K. Chua, An experimental and simulation study on build thickness dependent microstructure for electron beam melted Ti-6Al-4V, J. Alloys Compd. 646 (2015) 303–309. doi:10.1016/j.jallcom.2015.05.178.

[27] A. Majeed, A. Ahmed, B. Liu, S. Ren, J. Yang, Influence of wall thickness on the hardness of AlSi10Mg alloy parts manufactured by selective laser melting, Procedia CIRP. 81 (2019) 459–463. doi:10.1016/j.procir.2019.03.079.

[28] M.R. Stoudt, M.E. Williams, L.E. Levine, A. Creuziger, S.A. Young, J.C. Heigel, B.M. Lane, T.Q. Phan, Location-Specific Microstructure Characterization Within IN625 Additive Manufacturing Benchmark Test Artifacts, Integr. Mater. Manuf. Innov. 9 (2020) 54–69. doi:10.1007/s40192-020-00172-6.

[29] L. Levine, B. Lane, J. Heigel, K. Migler, M. Stoudt, T. Phan, R. Ricker, M.

Strantza, M. Hill, F. Zhang, J. Seppala, E. Garboczi, E. Bain, D. Cole, A. Allen, J. Fox, C. Campbell, Outcomes and Conclusions from the 2018 AM-Bench Measurements, Challenge Problems, Modeling Submissions, and Conference, Integr. Mater. Manuf. Innov. 9 (2020) 1–15. doi:10.1007/s40192-019-00164-1.

[30] T.Q. Phan, M. Strantza, M.R. Hill, T.H. Gnaupel-Herold, J. Heigel, C.R. D'Elia, A.T. DeWald, B. Clausen, D.C. Pagan, J.Y. Peter Ko, D.W. Brown, L.E. Levine, Elastic Residual Strain and Stress Measurements and Corresponding Part Deflections of 3D Additive Manufacturing Builds of IN625 AM-Bench Artifacts Using Neutron Diffraction, Synchrotron X-Ray Diffraction, and Contour Method, Integr. Mater. Manuf. Innov. 8 (2019) 318–334. doi:10.1007/s40192-019-00149-0.

[31] A. Saboori, G. Piscopo, M. Lai, A. Salmi, S. Biamino, An investigation on the effect of deposition pattern on the microstructure, mechanical properties and residual stress of 316L produced by Directed Energy Deposition, Mater. Sci. Eng. A. 780 (2020). doi:10.1016/j.msea.2020.139179.

[32] Z.E. Tan, J.H.L. Pang, J. Kaminski, H. Pepin, Characterisation of porosity, density, and microstructure of directed energy deposited stainless steel AISI 316L, Addit. Manuf. 25 (2019) 286–296. doi:10.1016/j.addma.2018.11.014.

[33] J.C. Haley, B. Zheng, U.S. Bertoli, A.D. Dupuy, J.M. Schoenung, E.J. Lavernia, Working distance passive stability in laser directed energy deposition additive manufacturing, Mater. Des. 161 (2019) 86–94. doi:10.1016/j.matdes.2018.11.021.

[34] Y.M. Wang, T. Voisin, J.T. McKeown, J. Ye, N.P. Calta, Z. Li, Z. Zeng, Y. Zhang, W. Chen, T.T. Roehling, R.T. Ott, M.K. Santala, P.J. Depond, M.J. Matthews, A. V. Hamza, T. Zhu, Additively manufactured hierarchical stainless steels with high strength and ductility, Nat. Mater. 17 (2018) 63–70. doi:10.1038/NMAT5021.

[35] Design Guidelines for the Selection and Use of Stainless Steels - A Designers' Handbook Series, Nickel Institute, 2020. https://app.knovel.com/hotlink/pdf/id:kt01284I6B/design-guidelines-selection/identification BT - Design Guidelines for the Selection and Use of Stainless Steels - A Designers' Handbook Series No 9014.

[36] P.S. Korinko, S.H. Malene, Considerations for the weldability of types 304L and 316L stainless steel, J. Fail. Anal. Prev. 1 (2001) 61–68. doi:10.1007/BF02715336.

[37] N. Haghdadi, M. Laleh, M. Moyle, S. Primig, Additive manufacturing of steels: a review of achievements and challenges, J. Mater. Sci. 56 (2021) 64–107. doi:10.1007/s10853-020-05109-0.

[38] T. DebRoy, H.L. Wei, J.S. Zuback, T. Mukherjee, J.W. Elmer, J.O. Milewski, A.M. Beese, A. Wilson-Heid, A. De, W. Zhang, Additive manufacturing of metallic components – Process, structure and properties, Prog. Mater. Sci. 92 (2018) 112–224. doi:10.1016/j.pmatsci.2017.10.001.

[39] C.A. Schneider, W.S. Rasband, K.W. Eliceiri, NIH Image to ImageJ: 25 years of image analysis, Nat. Methods. 9 (2012) 671–675. doi:10.1038/nmeth.2089.

[40] F. Bachmann, R. Hielscher, H. Schaeben, Texture analysis with MTEX- Free and open source software toolbox, Solid State Phenom. 160 (2010) 63–68. doi:10.4028/www.scientific.net/SSP.160.63.

[41] R. Hielscher, C.B. Silbermann, E. Schmidla, J. Ihlemannb, Denoising of crystal

orientation maps, J. Appl. Crystallogr. 52 (2019) 984–996. doi:10.1107/S1600576719009075.

[42] W. Pantleon, Resolving the geometrically necessary dislocation content by conventional electron backscattering diffraction, Scr. Mater. 58 (2008) 994–997. doi:10.1016/j.scriptamat.2008.01.050.

[43] ASTM Standard E112-13, 2013, Standard test methods for determining average grain size, ASTM Int. (2013). doi:10.1520/E0112-13.1.4.

[44] S. Katayama, A. Matsunawa, Solidification microstructure of laser welded stainless steels, in: ICALEO, 1984: pp. 60–67. doi:10.2351/1.5057623.

[45] A.L. Vyatskikh, T.B. Slagle, S. Jiang, S.A. El-azab, U.S. Bertoli, L. Valdevit, E.J. Lavernia, J.M. Schoenung, Thickness-Dependent Microstructure in Additively Manufactured Stainless Steel, J. Mater. Eng. Perform. (2021). doi:10.1007/s11665-021-05931-w.

[46] G. Krauss, Steels - Processing, Structure, and Performance, (n.d.). https://app.knovel.com/hotlink/toc/id:kpSPSP0001/steels-processing-structure/steels-processing-structure.

[47] H.U. Hong, B.S. Rho, S.W. Nam, Correlation of the M23C6 precipitation morphology with grain boundary characteristics in austenitic stainless steel, Mater. Sci. Eng. A. 318 (2001) 285–292. doi:10.1016/S0921-5093(01)01254-0.

[48] U. Scipioni Bertoli, B.E. MacDonald, J.M. Schoenung, Stability of cellular microstructure in laser powder bed fusion of 316L stainless steel, Mater. Sci. Eng. A. 739 (2019) 109–117. doi:10.1016/j.msea.2018.10.051.

[49] Y.M. Wang, T. Voisin, J.T. McKeown, J. Ye, N.P. Calta, Z. Li, Z. Zeng, Y. Zhang, W. Chen, T.T. Roehling, R.T. Ott, M.K. Santala, P.J. Depond, M.J. Matthews, A. V. Hamza, T. Zhu, Additively manufactured hierarchical stainless steels with high strength and ductility, Nat. Mater. 17 (2018) 63–70. doi:10.1038/NMAT5021.

[50] K. Saeidi, X. Gao, Y. Zhong, Z.J. Shen, Hardened austenite steel with columnar sub-grain structure formed by laser melting, Mater. Sci. Eng. A. 625 (2015) 221–229. doi:10.1016/j.msea.2014.12.018.

[51] V.D. Manvatkar, A.A. Gokhale, G. Jagan Reddy, A. Venkataramana, A. De, Estimation of melt pool dimensions, thermal cycle, and hardness distribution in the laser-engineered net shaping process of austenitic stainless steel, Metall. Mater. Trans. A Phys. Metall. Mater. Sci. 42 (2011) 4080–4087. doi:10.1007/s11661-011-0787-8.

[52] N. Suutala, T. Takalo, T. Moisio, Ferritic-austenitic solidification mode in austenitic stainless steel welds, Metall. Trans. A. 11 (1980) 717–725. doi:10.1007/BF02661201.

[53] J.A. Brooks, A.W. Thompson, Microstructural development and solidification cracking susceptibility of austenitic stainless steel welds, Int. Mater. Rev. 36 (1991) 16–44. doi:10.1179/imr.1991.36.1.16.

[54] Y. Strausser, 30. X-Ray Diffraction (XRD), in: Charact. Silicon Process., Elsevier, 1993. https://app.knovel.com/hotlink/pdf/id:kt002ZAP63/characterization-in-silicon/x-ray-diffraction-xrd BT - Characterization in Silicon Processing.

[55] A.L. Schaeffler, Constitution diagram for stainless steel weld metal, Met. Prog. 56 (1949) 680-680B.

[56] D. Séférian, Métallurgie de la soudure, Dunod, Paris, 1959.

[57] J.C. Lippold, D.J. Kotecki, Welding metallurgy and weldability of stainless steels, John Wiley & Sons, 2005. https://app.knovel.com/hotlink/khtml/id:kt0080VTT1/welding-metallurgy-weldability/alloying-e-references.

[58] S.A. David, J.M. Vitek, R.W. Reed, T.L. Hebble, Effect of rapid solidification on stainless steel weld metal microstructures and its implications on the Schaeffler diagram, United States, 1987. doi:10.2172/5957599.

[59] M. Letenneur, A. Kreitcberg, V. Brailovski, The average grain size and grain aspect ratio in metal laser powder bed fusion: Modeling and experiment, J. Manuf. Mater. Process. 4 (2020). doi:10.3390/jmmp4010025.

[60] N.J. Petch, The cleavage strength of crystals, J. Iron Steel Inst. 174 (1953) 25.

[61] E.O. Hall, The deformation and ageing of mild steel: III Discussion of results, Proc. Phys. Soc. Sect. B. 64 (1951) 747–753. doi:10.1088/0370-1301/64/9/303.

[62] M.S. Pham, B. Dovgyy, P.A. Hooper, C.M. Gourlay, A. Piglione, The role of side-branching in microstructure development in laser powder-bed fusion, Nat. Commun. 11 (2020) 1–12. doi:10.1038/s41467-020-14453-3.

[63] J.J. Marattukalam, D. Karlsson, V. Pacheco, P. Beran, U. Wiklund, U. Jansson, B. Hjörvarsson, M. Sahlberg, The effect of laser scanning strategies on texture, mechanical properties, and site-specific grain orientation in selective laser melted 316L SS, Mater. Des. 193 (2020). doi:10.1016/j.matdes.2020.108852.

[64] Y. Kok, X.P. Tan, P. Wang, M.L.S. Nai, N.H. Loh, E. Liu, S.B. Tor, Anisotropy and heterogeneity of microstructure and mechanical properties in metal additive manufacturing: A critical review, Mater. Des. 139 (2018) 565–586. doi:10.1016/j.matdes.2017.11.021.

[65] A. Yadollahi, N. Shamsaei, Additive manufacturing of fatigue resistant materials: Challenges and opportunities, Int. J. Fatigue. 98 (2017) 14–31. doi:10.1016/j.ijfatigue.2017.01.001.

[66] A. Riemer, S. Leuders, M. Thöne, H.A. Richard, T. Tröster, T. Niendorf, On the fatigue crack growth behavior in 316L stainless steel manufactured by selective laser melting, Eng. Fract. Mech. 120 (2014) 15–25. doi:10.1016/j.engfracmech.2014.03.008.

[67] T.S. Huang, G.S. Frankel, Influence of grain structure on anisotropic localised corrosion kinetics of AA7XXX-T6 alloys, Corros. Eng. Sci. Technol. 41 (2006) 192–199. doi:10.1179/174327806X120739.

[68] K.A. Small, Z. Clayburn, R. DeMott, S. Primig, D. Fullwood, M.L. Taheri, Interplay of dislocation substructure and elastic strain evolution in additively manufactured Inconel 625, Mater. Sci. Eng. A. 785 (2020) 139380. doi:10.1016/j.msea.2020.139380.

[69] T. Skippon, L. Balogh, M.R. Daymond, Comparison of electron backscatter and

x-ray diffraction techniques for measuring dislocation density in zircaloy-2, J. Appl. Crystallogr. 52 (2019) 415–427. doi:10.1107/S1600576719003054.

[70] C. Yan, L. Hao, A. Hussein, P. Young, Ti-6Al-4V triply periodic minimal surface structures for bone implants fabricated via selective laser melting, J. Mech. Behav. Biomed. Mater. 51 (2015) 61–73. doi:10.1016/j.jmbbm.2015.06.024.

[71] X. Wang, S. Xu, S. Zhou, W. Xu, M. Leary, P. Choong, M. Qian, M. Brandt, Y.M. Xie, Topological design and additive manufacturing of porous metals for bone scaffolds and orthopaedic implants: A review, Biomaterials. 83 (2016) 127–141. doi:10.1016/j.biomaterials.2016.01.012.

[72] S.M. Yusuf, S. Cutler, N. Gao, The impact of metal additive manufacturing on the aerospace industry, Metals (Basel). 9 (2019).

[73] L.J. Kumar, C.G.K. Nair, Current Trends of Additive Manufacturing in the Aerospace Industry, in: Adv. 3D Print. Addit. Manuf. Technol., Springer, 2016: pp. 39–54. doi:10.1007/978-981-10-0812-2.

[74] A.R. Thryft, SpaceX Reveals 3D-Printed Rocket Engine Parts, Des. News. (2014). https://www.designnews.com/design-hardware-software/spacex-reveals-3d-printed-rocket-engine-parts (accessed November 5, 2021).

[75] S. Yang, Y.F. Zhao, Additive Manufacturing-Enabled Part Count Reduction: A Lifecycle Perspective, J. Mech. Des. Trans. ASME. 140 (2018). doi:10.1115/1.4038922.

[76] S. Yang, W. Min, J. Ghibaudo, Y.F. Zhao, Understanding the sustainability potential of part consolidation design supported by additive manufacturing, J. Clean. Prod. 232 (2019) 722–738. doi:10.1016/j.jclepro.2019.05.380.

[77] Z. Nie, S. Jung, L.B. Kara, K.S. Whitefoot, Optimization of part consolidation for minimum production costs and time using additive manufacturing, J. Mech. Des. Trans. ASME. 142 (2020). doi:10.1115/1.4045106.

[78] Optomec, Quick Guide to Metal AM, (n.d.). https://optomec.com/wp-content/uploads/2019/06/Metal-AM-Selection-Guide.pdf (accessed November 5, 2021).

[79] J.W. Pegues, M.A. Melia, R. Puckett, S.R. Whetten, N. Argibay, A.B. Kustas, Exploring additive manufacturing as a high-throughput screening tool for multiphase high entropy alloys, Addit. Manuf. 37 (2021) 101598. doi:10.1016/j.addma.2020.101598.

[80] B. Heer, A. Bandyopadhyay, Compositionally graded magnetic-nonmagnetic bimetallic structure using laser engineered net shaping, Mater. Lett. 216 (2018) 16–19. doi:10.1016/j.matlet.2017.12.129.

[81] F.F. Noecker, J.N. Dupont, Functionally graded copper – steel using laser engineered net shaping, ICALEO. 185430 (2002). doi:10.2351/1.5066217.

[82] J. Xie, Z. Huang, H. Lu, B. Zheng, X. Xu, J. Lei, Additive manufacturing of tantalum-zirconium alloy coating for corrosion and wear application by laser directed energy deposition on Ti6Al4V, Surf. Coatings Technol. 411 (2021). doi:10.1016/j.surfcoat.2021.127006.

[83] A.K. Rai, B. Srinivasulu, C.P. Paul, R. Singh, S.K. Rai, G.K. Mishra, S. Bontha,

K.S. Bindra, Development of thick SiC coating on thin wall tube of zircaloy-4 using laser based directed energy deposition technique, Surf. Coatings Technol. 398 (2020) 126088. doi:10.1016/j.surfcoat.2020.126088.

[84] J.M. Wilson, C. Piya, Y.C. Shin, F. Zhao, K. Ramani, Remanufacturing of turbine blades by laser direct deposition with its energy and environmental impact analysis, J. Clean. Prod. 80 (2014) 170–178. doi:10.1016/j.jclepro.2014.05.084.

[85] A. Saboori, A. Aversa, G. Marchese, S. Biamino, M. Lombardi, P. Fino, Application of directed energy deposition-based additive manufacturing in repair, Appl. Sci. 9 (2019). doi:10.3390/app9163316.

[86] ASTM International, Standard Guide for Directed Energy Deposition of Metals, (2016) 1–22. doi:10.1520/F3187.

[87] M. Seifi, A. Salem, J. Beuth, O. Harrysson, J.J. Lewandowski, Overview of Materials Qualification Needs for Metal Additive Manufacturing, Jom. 68 (2016) 747–764. doi:10.1007/s11837-015-1810-0.

[88] J.J. Lewandowski, M. Seifi, Metal Additive Manufacturing: A Review of Mechanical Properties, Annu. Rev. Mater. Res. 46 (2016) 151–186. doi:10.1146/annurev-matsci-070115-032024.

[89] A. Dass, A. Moridi, State of the art in directed energy deposition: From additive manufacturing to materials design, Coatings. 9 (2019) 1–26. doi:10.3390/COATINGS9070418.

[90] C. Baykasoğlu, O. Akyildiz, M. Tunay, A.C. To, A process-microstructure finite element simulation framework for predicting phase transformations and microhardness for directed energy deposition of Ti6Al4V, Addit. Manuf. 35 (2020) 101252. doi:10.1016/j.addma.2020.101252.

[91] Z. Wang, E. Denlinger, P. Michaleris, A.D. Stoica, D. Ma, A.M. Beese, Residual stress mapping in Inconel 625 fabricated through additive manufacturing: Method for neutron diffraction measurements to validate thermomechanical model predictions, Mater. Des. 113 (2017) 169–177. doi:10.1016/j.matdes.2016.10.003.

[92] J. Lu, Prestress Engineering of Stuctural Material: A Global Design Approach to the Residual Stress Problem, in: G. Totten, M. Howes, T. Inoue (Eds.), Handb. Residual Stress Deform. Steel, ASM International, 2002: pp. 11–26. doi:10.1361/hrsd2002p011.

[93] T. Inoue, Z. Wang, Coupling between stress, temperature, and metallic structures during processes involving phase transformations, Mater. Sci. Technol. (United Kingdom). 1 (1985) 845–850. doi:10.1179/mst.1985.1.10.845.

[94] M.C. Payares-Asprino, H. Katsumoto, S. Liu, Effect of martensite start and finish temperature on residual stress development in structural steel welds, Weld. J. (Miami, Fla). 87 (2008) 279–289.

[95] V. Manvatkar, A. De, T. Debroy, Heat transfer and material flow during laser assisted multi-layer additive manufacturing, J. Appl. Phys. 116 (2014). doi:10.1063/1.4896751.

[96] F. Lia, J.Z. Park, J.S. Keist, S. Joshi, R.P. Martukanitz, Thermal and microstructural analysis of laser-based directed energy deposition for Ti-6Al-4V and

Inconel 625 deposits, Mater. Sci. Eng. A. 717 (2018) 1–10. doi:10.1016/j.msea.2018.01.060.

[97] C. Kenel, D. Grolimund, X. Li, E. Panepucci, V.A. Samson, D.F. Sanchez, F. Marone, C. Leinenbach, In situ investigation of phase transformations in Ti-6Al-4V under additive manufacturing conditions combining laser melting and high-speed micro-X-ray diffraction, Sci. Rep. 7 (2017) 1–10. doi:10.1038/s41598-017-16760-0.

[98] B. Zheng, Y. Zhou, J.E. Smugeresky, J.M. Schoenung, E.J. Lavernia, Thermal behavior and microstructural evolution during laser deposition with laser-engineered net shaping: Part I. Numerical calculations, Metall. Mater. Trans. A Phys. Metall. Mater. Sci. 39 (2008) 2228–2236. doi:10.1007/s11661-008-9557-7.

[99] K. Zhang, S. Wang, W. Liu, X. Shang, Characterization of stainless steel parts by Laser Metal Deposition Shaping, Mater. Des. 55 (2014) 104–119. doi:10.1016/j.matdes.2013.09.006.

[100] M.L. Griffith, M.E. Schlieriger, L.D. Harwell, M.S. Oliver, M.D. Baldwin, M.T. Ensz, M. Essien, J. Brooks, C. V. Robino, J.E. Smugeresky, W.H. Hofmeister, M.J. Wert, D. V. Nelson, Understanding thermal behavior in the LENS process, Mater. Des. 20 (1999) 107–113.

[101] D.A. Kriczky, J. Irwin, E.W. Reutzel, P. Michaleris, A.R. Nassar, J. Craig, 3D spatial reconstruction of thermal characteristics in directed energy deposition through optical thermal imaging, J. Mater. Process. Technol. 221 (2015) 172–186. doi:10.1016/j.jmatprotec.2015.02.021.

[102] X. Lu, X. Lin, M. Chiumenti, M. Cervera, Y. Hu, X. Ji, Residual stress and distortion of rectangular and S-shaped Ti-6Al-4V parts by Directed Energy Deposition : Modelling and experimental calibration, Addit. Manuf. 26 (2019) 166–179. doi:10.1016/j.addma.2019.02.001.

[103] J.C. Heigel, P. Michaleris, E.W. Reutzel, Thermo-mechanical model development and validation of directed energy deposition additive manufacturing of Ti-6Al-4V, Addit. Manuf. 5 (2015) 9–19. doi:10.1016/j.addma.2014.10.003.

[104] K.L. Terrassa, T.R. Smith, S. Jiang, J.D. Sugar, J.M. Schoenung, Improving build quality in Directed Energy Deposition by cross-hatching, Mater. Sci. Eng. A. (2019) 138269. doi:https://doi.org/10.1016/j.msea.2019.138269.

[105] W.E. Frazier, Metal additive manufacturing: A review, J. Mater. Eng. Perform. 23 (2014) 1917–1928. doi:10.1007/s11665-014-0958-z.

[106] B.A. Szost, S. Terzi, F. Martina, D. Boisselier, A. Prytuliak, T. Pirling, M. Hofmann, D.J. Jarvis, A comparative study of additive manufacturing techniques: Residual stress and microstructural analysis of CLAD and WAAM printed Ti-6Al-4V components, Mater. Des. 89 (2016) 559–567. doi:10.1016/j.matdes.2015.09.115.

[107] M. Strantza, B. Vrancken, M.B. Prime, C.E. Truman, M. Rombouts, D.W. Brown, P. Guillaume, D. Van Hemelrijck, Directional and oscillating residual stress on the mesoscale in additively manufactured Ti-6Al-4V, Acta Mater. 168 (2019) 299–308. doi:10.1016/j.actamat.2019.01.050.

[108] M. Alimardani, E. Toyserkani, J.P. Huissoon, C.P. Paul, On the delamination and crack formation in a thin wall fabricated using laser solid freeform fabrication process: An experimental–numerical investigation, Opt. Lasers Eng. 47 (2009) 1160–

1168. doi:https://doi.org/10.1016/j.optlaseng.2009.06.010.

[109] D. Gu, B. He, Finite element simulation and experimental investigation of residual stresses in selective laser melted Ti-Ni shape memory alloy, Comput. Mater. Sci. 117 (2016) 221–232. doi:10.1016/j.commatsci.2016.01.044.

[110] R. Chattopadhyay, Life-Cycle Assessment, in: Green Tribol. Green Surf. Eng. Glob. Warm., ASM International, 2014: pp. 193–237.

[111] J. Zhang, X. Wang, S. Paddea, X. Zhang, Fatigue crack propagation behaviour in wire+arc additive manufactured Ti-6Al-4V: Effects of microstructure and residual stress, Mater. Des. 90 (2016) 551–561. doi:10.1016/j.matdes.2015.10.141.

[112] C. Li, Z.Y. Liu, X.Y. Fang, Y.B. Guo, Residual Stress in Metal Additive Manufacturing, Procedia CIRP. 71 (2018) 348–353. doi:10.1016/j.procir.2018.05.039.

[113] N.S. Rossini, M. Dassisti, K.Y. Benyounis, A.G. Olabi, Methods of measuring residual stresses in components, Mater. Des. 35 (2012) 572–588. doi:10.1016/j.matdes.2011.08.022.

[114] P.J. Withers, H.K.D.H. Bhadeshia, Residual stress. Part 1 – Measurement techniques, Mater. Sci. Technol. 17 (2001) 355–365. doi:10.1179/026708301101509980.

[115] P.S. Prevey, X-Ray Diffaction Residual Stress Techniques, in: ASM Handbook, Vol. 10 Mater. Charact., 1986: pp. 380–392. doi:10.1361/asmhba000.

[116] C.O. Ruud, A review of selected non-destructive methods for residual stress measurement, NDT Int. 15 (1982) 15–23. doi:10.1016/0308-9126(82)90083-9.

[117] C. Ruud, Measurement of residual stresses, in: G. Totten, M. Howes, T. Inoue (Eds.), Handb. Residual Stress Deform. Steel, ASM International, 2002: pp. 99–117. doi:10.1361/hrsd2002p011.

[118] M.T. Hutchings, P.J. Withers, T.M. Holden, T. Lorentzen, Introduction to the Characterization of Residual Stress by Neutron Diffraction, Taylor & Francis, 2005.

[119] W. Wu, A.D. Stoica, K.D. Berry, M.J. Frost, H.D. Skorpenske, K. An, PIND: High spatial resolution by pinhole neutron diffraction, Appl. Phys. Lett. 112 (2018). doi:10.1063/1.5026066.

[120] R. Pokharel, A. Patra, D.W. Brown, B. Clausen, S.C. Vogel, G.T. Gray, An analysis of phase stresses in additively manufactured 304L stainless steel using neutron diffraction measurements and crystal plasticity finite element simulations, Int. J. Plast. (2019) 1–17. doi:10.1016/j.ijplas.2019.06.005.

[121] J. Gauthier, T.W. Krause, D.L. Atherton, Measurement of residual stress in steel using the magnetic Barkhausen noise technique, NDT E Int. 31 (1998) 23–31. doi:10.1016/S0963-8695(97)00023-6.

[122] D.J. Corbin, A.R. Nassar, E.W. Reutzel, A.M. Beese, P. Michaleris, Effect of substrate thickness and preheating on the distortion of laser deposited ti-6al-4v, J. Manuf. Sci. Eng. Trans. ASME. 140 (2018) 1–9. doi:10.1115/1.4038890.

[123] A. Vasinonta, J.L. Beuth, M. Griffith, Process maps for predicting residual stress and melt pool size in the laser-based fabrication of thin-walled structures, J. Manuf. Sci. Eng. Trans. ASME. 129 (2007) 101–109. doi:10.1115/1.2335852.

[124] E.R. Denlinger, J.C. Heigel, P. Michaleris, T.A. Palmer, Effect of inter-layer dwell time on distortion and residual stress in additive manufacturing of titanium and nickel alloys, J. Mater. Process. Technol. 215 (2015) 123–131. doi:10.1016/j.jmatprotec.2014.07.030.

[125] W. Woo, D.K. Kim, E.J. Kingston, V. Luzin, F. Salvemini, M.R. Hill, Effect of interlayers and scanning strategies on through-thickness residual stress distributions in additive manufactured ferritic-austenitic steel structure, Mater. Sci. Eng. A. 744 (2019) 618–629. doi:10.1016/j.msea.2018.12.078.

[126] J. Yu, X. Lin, L. Ma, J. Wang, X. Fu, J. Chen, W. Huang, Influence of laser deposition patterns on part distortion, interior quality and mechanical properties by laser solid forming (LSF), Mater. Sci. Eng. A. 528 (2011) 1094–1104. doi:10.1016/j.msea.2010.09.078.

[127] L. Ma, H. Bin, Temperature and stress analysis and simulation in fractal scanning-based laser sintering, Int. J. Adv. Manuf. Technol. 34 (2007) 898–903. doi:10.1007/s00170-006-0665-5.

[128] M. Strantza, R.K. Ganeriwala, B. Clausen, T.Q. Phan, L.E. Levine, D.C. Pagan, J. Ruff, W.E. King, N.S. Johnson, R.M. Martinez, V. Anghel, G. Rafailov, D.W. Brown, Effect of the scanning strategy on the formation of residual stresses in additively manufactured Ti-6Al- 4V, Addit. Manuf. (2021) 158069. doi:10.1016/j.addma.2021.102003.

[129] Z. Wang, A.D. Stoica, D. Ma, A.M. Beese, Stress relaxation in a nickel-base superalloy at elevated temperatures with in situ neutron diffraction characterization: Application to additive manufacturing, Mater. Sci. Eng. A. 714 (2018) 75–83. doi:10.1016/j.msea.2017.12.058.

[130] F. Zhang, L.E. Levine, A.J. Allen, M.R. Stoudt, G. Lindwall, E.A. Lass, M.E. Williams, Y. Idell, C.E. Campbell, Effect of heat treatment on the microstructural evolution of a nickel-based superalloy additive-manufactured by laser powder bed fusion, Acta Mater. 152 (2018) 200–214. doi:10.1016/j.actamat.2018.03.017.

[131] H. Yamaguchi, O. Fergani, P.Y. Wu, Modification using magnetic field-assisted finishing of the surface roughness and residual stress of additively manufactured components, CIRP Ann. - Manuf. Technol. 66 (2017) 305–308. doi:10.1016/j.cirp.2017.04.084.

[132] W. Guo, R. Sun, B. Song, Y. Zhu, F. Li, Z. Che, B. Li, C. Guo, L. Liu, P. Peng, Laser shock peening of laser additive manufactured Ti6Al4V titanium alloy, Surf. Coatings Technol. 349 (2018) 503–510. doi:10.1016/j.surfcoat.2018.06.020.

[133] R. Sun, L. Li, Y. Zhu, W. Guo, P. Peng, B. Cong, J. Sun, Z. Che, B. Li, C. Guo, L. Liu, Microstructure, residual stress and tensile properties control of wire-arc additive manufactured 2319 aluminum alloy with laser shock peening, J. Alloys Compd. 747 (2018) 255–265. doi:10.1016/j.jallcom.2018.02.353.

[134] A. Ohta, N. Suzuki, Y. Maeda, K. Hiraoka, T. Nakamura, Superior fatigue crack growth properties in newly developed weld metal, Int. J. Fatigue. 21 (1999) 113–118. doi:10.1016/s0142-1123(99)00062-6.

[135] T. Ramjaun, H.J. Stone, L. Karlsson, J. Kelleher, R.J. Moat, J.R. Kornmeier, K. Dalaei, H.K.D.H. Bhadeshia, Effect of interpass temperature on residual stresses in

multipass welds produced using low transformation temperature filler alloy, Sci. Technol. Weld. Join. 19 (2014) 44–51. doi:10.1179/1362171813Y.0000000162.

[136] J. Dixneit, F. Vollert, A. Kromm, J. Gibmeier, A. Hannemann, T. Fischer, T. Kannengiesser, In situ analysis of the strain evolution during welding using low transformation temperature filler materials, Sci. Technol. Weld. Join. 24 (2019) 243–255. doi:10.1080/13621718.2018.1525150.

[137] X. Chen, K. Hu, S. Lin, The Properties and Residual Stress of Argon arc Cladding Metal by Low Temperature Martensitic Transformation Powder, J. Surf. Investig. 11 (2017) 1329–1337. doi:10.1134/S1027451017060222.

[138] D. Le Maux, M. Courtois, T. Pierre, B. Lamien, P. Le Masson, Density measurement of liquid 22MnB5 by aerodynamic levitation, Rev. Sci. Instrum. 90 (2019). doi:10.1063/1.5089620.

[139] M. Forde, ICE Manual of Construction Materials, Volume 1 - Fundamentals and Theory; Concrete; Asphalts in Road Construction; Masonry., ICE Publishing, 2009. https://app.knovel.com/hotlink/toc/id:kpICEMCMV3/ice-manual-construction/ice-manual-construction.

[140] O. Kubaschewski, Iron - binary phase diagrams, Springer Science & Business Media, 1982. doi:https://doi.org/10.1007/978-3-662-08024-5.

[141] X. Zhang, T. Pan, Y. Chen, L. Li, Y. Zhang, F. Liou, Additive manufacturing of copper-stainless steel hybrid components using laser-aided directed energy deposition, J. Mater. Sci. Technol. 80 (2021) 100–116. doi:10.1016/j.jmst.2020.11.048.

[142] A. Zafari, K. Xia, Nano/ultrafine grained immiscible Fe-Cu alloy with ultrahigh strength produced by selective laser melting, Mater. Res. Lett. 9 (2021) 247–254. doi:10.1080/21663831.2021.1884620.

[143] C.S. Smith, E.W. Palmer, Alloys of copper and iron, JOM. 2 (1950) 1486–1499. doi:10.1007/bf03399177.

[144] S.F. Abbas, K.T. Park, T.S. Kim, Effect of composition and powder size on magnetic properties of rapidly solidified copper-iron alloys, J. Alloys Compd. 741 (2018) 1188–1195. doi:10.1016/j.jallcom.2018.01.245.

[145] J. He, J.Z. Zhao, L. Ratke, Solidification microstructure and dynamics of metastable phase transformation in undercooled liquid Cu-Fe alloys, Acta Mater. 54 (2006) 1749–1757. doi:10.1016/j.actamat.2005.12.023.

[146] M.M. Pereira de Azevedo, M.S. Rogalski, J.B. Sousa, Magnetoresistance and phase analysis in splat-cooled Fe-Cu granular alloys, Solid State Commun. 100 (1996) 639–644.

[147] Y.Z. Chen, F. Liu, G.C. Yang, X.Q. Xu, Y.H. Zhou, Rapid solidification of bulk undercooled hypoperitectic Fe-Cu alloy, J. Alloys Compd. 427 (2007) 3–7. doi:10.1016/j.jallcom.2006.03.012.

[148] A. Munitz, Liquid separation effects in Fe-Cu alloys solidified under different cooling rates, Metall. Trans. B. 18 (1987) 565–575. doi:10.1007/BF02654269.

[149] K.I. Makarenko, I. V. Shishkovsky, Direct Energy Deposition of Cu-Fe System

Functionally Graded Structures, IOP Conf. Ser. Mater. Sci. Eng. 969 (2020). doi:10.1088/1757-899X/969/1/012104.

[150] K.S. Osipovich, E.G. Astafurova, A. V. Chumaevskii, K.N. Kalashnikov, S. V. Astafurov, G.G. Maier, E. V. Melnikov, V.A. Moskvina, M.Y. Panchenko, S.Y. Tarasov, V.E. Rubtsov, E.A. Kolubaev, Gradient transition zone structure in "steel–copper" sample produced by double wire-feed electron beam additive manufacturing, J. Mater. Sci. 55 (2020) 9258–9272. doi:10.1007/s10853-020-04549-y.

[151] J.R. Davis, Concise Metals Engineering Data Book, ASM International, 1997. https://app.knovel.com/hotlink/toc/id:kpCMEDB005/concise-metals-engineering/concise-metals-engineering.

[152] K. Farrell, J.T. Houston, J.W. Chumley, Hot Cracking in Fusion Welds in Tungsten, Weld. Res. Suppl. 49 (1970).

[153] C.P. Wang, X.J. Liu, I. Ohnuma, R. Kainuma, K. Ishida, Formation of immiscible alloy powders with egg-type microstructure, Science (80-.). 297 (2002) 990–993. doi:10.1126/science.1073050.

[154] D.L. Bourell, W. Frazier, H. Kuhn, M. Seifi, ASM Handbook®, Volume 24 - Additive Manufacturing Processes, ASM International, 2020. https://app.knovel.com/hotlink/toc/id:kpASMHVA23/asm-handbook-volume-24/asm-handbook-volume-24.

[155] M. Niinomi, Metals for Biomedical Devices, 2nd ed., Elsevier, 2019. https://app.knovel.com/hotlink/toc/id:kpMBDE0004/metals-biomedical-devices/metals-biomedical-devices.

[156] B. Cantor, I.T.H. Chang, P. Knight, A.J.B. Vincent, Microstructural development in equiatomic multicomponent alloys, Mater. Sci. Eng. A. 375–377 (2004) 213–218. doi:10.1016/j.msea.2003.10.257.

[157] J.W. Yeh, S.K. Chen, S.J. Lin, J.Y. Gan, T.S. Chin, T.T. Shun, C.H. Tsau, S.Y. Chang, Nanostructured high-entropy alloys with multiple principal elements: Novel alloy design concepts and outcomes, Adv. Eng. Mater. 6 (2004) 299–303. doi:10.1002/adem.200300567.

[158] D.B. Miracle, O.N. Senkov, A critical review of high entropy alloys and related concepts, Acta Mater. 122 (2017) 448–511. doi:10.1016/j.actamat.2016.08.081.

[159] C.M. Rost, E. Sachet, T. Borman, A. Moballegh, E.C. Dickey, D. Hou, J.L. Jones, S. Curtarolo, J.P. Maria, Entropy-stabilized oxides, Nat. Commun. 6 (2015) 1–8. doi:10.1038/ncomms9485.

[160] J. Gild, Y. Zhang, T. Harrington, S. Jiang, T. Hu, M.C. Quinn, W.M. Mellor, N. Zhou, K. Vecchio, J. Luo, High-Entropy Metal Diborides: A New Class of High-Entropy Materials and a New Type of Ultrahigh Temperature Ceramics, Sci. Rep. 6 (2016) 2–11. doi:10.1038/srep37946.

[161] P. Sarker, T. Harrington, C. Toher, C. Oses, M. Samiee, J.P. Maria, D.W. Brenner, K.S. Vecchio, S. Curtarolo, High-entropy high-hardness metal carbides discovered by entropy descriptors, Nat. Commun. 9 (2018) 1–10. doi:10.1038/s41467-018-07160-7.

[162] C. Oses, C. Toher, S. Curtarolo, High-entropy ceramics, Nat. Rev. Mater. 5

(2020) 295–309. doi:10.1038/s41578-019-0170-8.

[163] D. Liu, Y. Huang, L. Liu, L. Zhang, A novel of MSi2 high-entropy silicide: Be expected to improve mechanical properties of MoSi2, Mater. Lett. 268 (2020). doi:10.1016/j.matlet.2020.127629.

[164] J. Gild, J. Braun, K. Kaufmann, E. Marin, T. Harrington, P. Hopkins, K. Vecchio, J. Luo, A high-entropy silicide: (Mo 0.2 Nb 0.2 Ta 0.2 Ti 0.2 W 0.2)Si 2, J. Mater. 5 (2019) 337–343. doi:10.1016/j.jmat.2019.03.002.

[165] R.W. Mann, L.A. Clevenger, P.D. Agnello, F.R. White, Silicides and local interconnections for high-performance VLSI applications, IBM J. Res. Dev. 39 (1995) 403–417.

[166] K. Maex, M. Van Rossum, Properties of Metal Silicides, (1995).

[167] O.N. Senkov, C. Zhang, A.L. Pilchak, E.J. Payton, C. Woodward, F. Zhang, CALPHAD-aided development of quaternary multi-principal element refractory alloys based on NbTiZr, J. Alloys Compd. 783 (2019) 729–742. doi:10.1016/j.jallcom.2018.12.325.

[168] D.J.M. King, S.C. Middleburgh, A.G. McGregor, M.B. Cortie, Predicting the formation and stability of single phase high-entropy alloys, Acta Mater. 104 (2016) 172–179. doi:10.1016/j.actamat.2015.11.040.

[169] F. Zhang, C. Zhang, S.L. Chen, J. Zhu, W.S. Cao, U.R. Kattner, An understanding of high entropy alloys from phase diagram calculations, Calphad Comput. Coupling Phase Diagrams Thermochem. 45 (2014) 1–10. doi:10.1016/j.calphad.2013.10.006.

[170] H. Mao, H.L. Chen, Q. Chen, TCHEA1: A Thermodynamic Database Not Limited for “High Entropy” Alloys, J. Phase Equilibria Diffus. 38 (2017) 353–368. doi:10.1007/s11669-017-0570-7.

[171] B.H. Toby, R.B. Von Dreele, GSAS-II: The genesis of a modern open-source all purpose crystallography software package, J. Appl. Crystallogr. 46 (2013) 544–549. doi:10.1107/S0021889813003531.

[172] P.S. Frankwicz, J.H. Perepezko, Phase stability of MoSi2 in the C11b and C40 structures at high temperatures, Mater. Sci. Eng. A. 246 (1998) 199–206. doi:10.1016/s0921-5093(97)00747-8.

[173] W.J. Boettinger, J.H. Perepezko, P.S. Frankwicz, Application of ternary phase diagrams to the development of MoSi 2 -based materials, Mater. Sci. Eng. A. 155 (1992) 33–44. doi:10.1016/0921-5093(92)90310-W.

[174] R. Hollerweger, D. Holec, J. Paulitsch, M. Bartosik, R. Daniel, R. Rachbauer, P. Polcik, J. Keckes, C. Krywka, H. Euchner, P.H. Mayrhofer, Complementary ab initio and X-ray nanodiffraction studies of Ta2O5, Acta Mater. 83 (2015) 276–284. doi:10.1016/S1474-4422(10)70250-7.

[175] P. Aloke, S. Divinski, Handbook of Solid State Diffusion, Volume 2 - Diffusion Analysis in Material Applications, Elsevier, 2017. https://app.knovel.com/hotlink/toc/id:kpHSSDVDA1/handbook-solid-state/handbook-solid-state.

[176] C.L. Yaws, Yaws' Handbook of Thermodynamic Properties for Hydrocarbons and Chemicals, Knovel, 2009. https://app.knovel.com/hotlink/toc/id:kpYHTPHC09/yaws-handbook-thermodynamic/yaws-handbook-thermodynamic.

[177] A.R. Denton, N.W. Ashcroft, Vegard's law, Phys. Rev. A. 43 (1991) 3161–3164. doi:10.1002/pssb.19660180251.

[178] K. Wasa, M. Kitabatake, H. Adachi, Thin Film Materials Technology - Sputtering of Compound Materials, (2004). https://app.knovel.com/hotlink/toc/id:kpTFMTSCM6/thin-film-materials-technology/thin-film-materials-technology.

[179] F.M. Smits, Measurement of Sheet Resistivities with the Four-Point Probe, Bell Syst. Tech. J. 37 (1958) 711–718. doi:10.1002/j.1538-7305.1958.tb03883.x.

[180] N.M. Ravindra, L. Jin, D. Ivanov, V.R. Mehta, L.M. Dieng, G. Popov, O.H. Gokce, J. Grow, A.T. Fiory, Electrical and compositional properties of TaSi2 films, J. Electron. Mater. 31 (2002) 1074–1079. doi:10.1007/s11664-002-0045-3.

[181] M. Abd El Qader, R. Venkat, R. Kumar, T. Hartmann, P. Ginobbi, N. Newman, R. Singh, Structural, electrical, and thermoelectric properties of CrSi2 thin films, Thin Solid Films. 545 (2013) 100–105. doi:10.1016/j.tsf.2013.07.040.

[182] F. Nava, O. Bisi, P. Psaras, H. Takai, K.N. Tu, Electrical characterization of alloy thin films of VSi2 and V3Si, Thin Solid Films. 140 (1986) 167–172.

[183] A.H. Van Ommen, A.H. Reader, J.W.C. De Vries, Influence of microstructure on the resistivity of MoSi2 thin films, J. Appl. Phys. 64 (1988) 3574–3580. doi:10.1063/1.341418.

[184] C.D. Rude, T.P. Chow, A.J. Steckl, Characterization of NbSi2 thin films, J. Appl. Phys. 53 (1982) 5703–5709.